SURFACES AND INTERFACES IN THE GROWTH OF $SrTiO_3$ ON Si BY PULSED LASER DEPOSITION

Tjaša Parkelj Potočnik

Doctoral Dissertation
Jožef Stefan International Postgraduate School
Ljubljana, Slovenia

Supervisor: Asst. Prof. Matjaž Spreitzer, Jožef Stefan Institute and Jožef Stefan International Postgraduate School, Ljubljana, Slovenia

Evaluation Board:
Asst. Prof. Erik Zupanič, Chair, Jožef Stefan Institute and Jožef Stefan International Postgraduate School, Ljubljana, Slovenia
Prof. Dr. Dean Cvetko, Member, Faculty of Mathematics and Physics, University of Ljubljana, Ljubljana, Slovenia
Prof. Dr. Ulrike Diebold, Member, Vienna University of Technology (TU Wien), Vienna, Austria

MEDNARODNA PODIPLOMSKA ŠOLA JOŽEFA STEFANA
JOŽEF STEFAN INTERNATIONAL POSTGRADUATE SCHOOL

Tjaša Parkelj Potočnik

SURFACES AND INTERFACES IN THE GROWTH OF $SrTiO_3$ ON Si BY PULSED LASER DEPOSITION

Doctoral Dissertation

POVRŠINE IN MEJNE PLASTI PRI RASTI $SrTiO_3$ NA Si S TEHNIKO PULZNEGA LASERSKEGA NANAŠANJA

Doktorska disertacija

Supervisor: Asst. Prof. Matjaž Spreitzer

Ljubljana, Slovenia, May 2021

Acknowledgments

I am very lucky to have had Asst. Prof. Matjaž Spreitzer as my supervisor during my doctoral studies. I am very grateful for his guidance, patience, and understanding, and for providing me the opportunities for excellent research collaborations. I would especially like to thank Prof. Danilo Suvorov for giving me the opportunity to begin my research work at the K9 department.

I would like to thank the members of the Evaluation Board, Asst. Prof. Erik Zupanič, Prof. Dean Cvetko and Prof. Ulrike Diebold for their time and effort invested in the review and evaluation of the dissertation. Additionally, I am grateful to Asst. Prof. Erik Zupanič for all the discussions, support throughout my Ph.D. and help with the vacuum suitcase integrations and STM measurements and to Prof. Ulrike Diebold together with Dr. Michele Riva and Dr. Giada Franceschi for hosting me at their labs and giving me the opportunity to perform experiments at their MBE-PLD-XPS-STM ultra-high vacuum cluster.

I would like to thank the PLD group members, Dr. Urška Trstenjak, Dr. Daniel Diaz Fernandez, Dr. Zoran Jovanović, Dr. Dejan Klement and Dr. Jamal Belhadi for the wonderful teamwork and all their help and support. I would also like to thank Asst. Prof. Janez Kovač for XPS analysis, Prof. Philippe Ghosez, Dr. Eric Bousquet, and Dr. Wen-Yi Tong for DFT calculations and simulations of STM images, Prof. Gertjan Koster for debates related to the PLD technique and hosting me at their PLD labs at the beginning of my doctoral studies, Dr. Juan Rubio Zuazo for his help with XRD and XRR data analysis and measurements acquired at the ESRF synchrotron, Prof. Hana Uršič Nemevšek for PFM analysis, Marion Van Midden for her help with STM measurements and all our lunch discussions, K9 co-workers for all the pleasant coffee breaks (virtual and in person), and especially Uroš Hribar and Damjan Vengust for helping me carry the vacuum suitcase.

Last, but not least, I am very grateful for all the support and encouragement received from my family and friends throughout the period of my Ph.D. Aljaž, you gave me the courage to begin this journey and helped me every step of the way.

I would also like to acknowledge that this research was supported by the Slovenian Research Agency [grants number PR-06807, J2-6759, J2-9237, and P2-0091] and international projects: ENPIEZO [M-ERA.NET 3330-14-500197] and SIOX [M-ERA.NET 3330-17-500100].

Abstract

$SrTiO_3$ (STO) thin films are used as buffer layers that enable epitaxial integration of various functional oxides with silicon. When pulsed laser deposition (PLD) is used to grow STO on Si, a thin amorphous layer is formed at the STO-Si interface that limits the use of such heterostructures in certain applications. This thesis deals with the structural and chemical properties of surfaces, interfaces, and films formed during a multi-stage procedure used for the growth of ultra-thin STO films on Si(001) surfaces using the PLD technique, in order to understand the mechanisms that lead to epitaxial integration with an atomically abrupt interface. In this procedure, the deoxidation of Si substrates is followed by a deposition of ½ monolayer (ML) of Sr, which is used to passivate the Si surface, and the STO film growth, where the deposition, oxidation, and crystallization steps are carried out cyclically until a thickness of ~ 10 ML is achieved.

In the first part, the quality of deoxidized Si(001)(2×1) surfaces was inspected and it was confirmed that the contamination of the surface due to exposure to $\sim 1\times10^{-8}$ mbar of residual atmosphere for 5 min (which is difficult to avoid in PLD systems) is low enough to preserve a crystalline surface until it is passivated with Sr.

In the second part, PLD was used to prepare Sr/Si(001)(1×2) surfaces, followed by structural and chemical analysis performed without breaking vacuum. Scanning tunneling microscopy (STM) images showed an atomically ordered surface with terraces composed of corrugated one-dimensional chains running perpendicularly on neighboring terraces forming a double domain (2×1)+(1×2) surface reconstruction revealing a surface unit cell with 0.78 nm × 0.39 nm dimensions along with different types of surface defects. The interpretation of experimental STM images is supported by simulated images based on density functional theory.

In the final part, PLD was used to grow epitaxial ultra-thin (3–4 nm) STO films on Sr-Si surfaces. The optimization of STO deposition, oxidation, and crystallization parameters led to a significant improvement of the crystalline quality of the STO films and reduction of the interlayer thickness. It has been found that the minimization of the thermal budget during crystallization increases the interface sharpness, however, it can limit the densification of the STO film. The STO films prepared by the optimised procedure are single-phase and exhibit STO(001)||Si(001) out-of-plane and STO[110]||Si[100] in-plane orientation. Most of the STO film has a cubic unit cell 2-5% larger compared to bulk STO which is related to a slight non-stoichiometry of the film. A large part of the STO film is relaxed due to an amorphous silicate layer present at the STO-Si interface which starts forming during the deposition of the first 2 ML of STO and expands by every STO deposition-oxidation-crystallization cycle reaching a thickness of 1.2–1.9 nm after deposition of ~10 ML of STO.

Although the amorphization of the STO-Si interface cannot be avoided completely, ultra-thin STO films on Si produced by PLD can still be used as an excellent template for the growth of thicker STO films and the epitaxial integration of various functional oxides with Si.

Povzetek

Tanke plasti $SrTiO_3$ (STO) se uporabljajo kot puferske plasti, ki omogočajo epitaksialno integracijo različnih funkcionalnih oksidov s silicijem. Kadar se za rast STO na Si uporablja pulzno lasersko nanašanje (PLD), se na spoju STO-Si tvori tanka amorfna plast, ki omejuje uporabo tovrstnih heterostruktur v določenih aplikacijah. V doktorskem delu so obravnavane strukturne in kemijske lastnosti površin, medpovršin in plasti, ki nastajajo med večstopenjskim postopkom, ki se uporablja za rast ultratankih plasti STO na površinah Si(001) s pomočjo tehnike PLD, da bi dobili vpogled v mehanizme, ki vodijo do epitaksialne integracije z atomsko ostro mejo. Pri tem postopku deoksidaciji Si substratov sledi nanos elementarnega Sr, ki se uporablja za pasivacijo Si površine, in rast STO plasti, kjer se koraki nanašanja, oksidacije in kristalizacije izvajajo ciklično do debeline plasti ~10 enoatomskih plasti (ML).

V prvem delu je bila preverjena kakovost deoksidiranih površin Si(001)(2×1), izpostavljenim tlaku rezidualne atmosfere $\sim 1\times10^{-8}$ mbar za čas 5 min (čemur se je v sistemih za PLD težko izogniti). Izkazalo se je, da pri tako nizki izpostavljenosti ne prihaja do amorfizacije Si površine, ki jo je mogoče ohraniti dokaj čisto do njene pasivacije s Sr.

V drugem delu je bilo s pomočjo PLD tehnike na Si(001) površino nanešeno ½ ML Sr, čemur je sledila strukturna in kemijska analiza površine, izvedena pod pogoji ultravisokega vakuuma. Slike vrstične tunelske mikroskopije (STM) so pokazale atomsko urejeno površino s terasami, sestavljenimi iz valovitih enodimenzionalnih verig, ki potekajo pravokotno na sosednjih terasah in tvorijo površinsko rekonstrukcijo (2×1)+(1×2) z osnovno celico dimenzij 0,78 nm × 0,39 nm ter različnimi vrstami površinskih defektov. Interpretacija eksperimentalnih slik STM je podprta s simuliranimi slikami, ki temeljijo na izračunih teorije gostotnih funkcionalov.

V zadnjem delu je bila PLD tehnika uporabljena za pripravo epitaksialnih ultratankih (3–4 nm) STO plasti na površinah Sr-Si. Optimizacija parametrov nanašanja, oksidacije in kristalizacije je privedla do očitnega izboljšanja kristalne kakovosti STO plasti in zmanjšanja debeline amorfne vmesne plasti. Ugotovljeno je bilo, da zmanjšanje toplotne obremenitve vzorcev med kristalizacijo poveča ostrino spoja tanke plasti s substratom, a lahko hkrati negativno vpliva na zgoščevanje STO plasti. STO plasti, pripravljene po optimiziranem postopku, so enofazne in izkazujejo STO(001)||Si(001) izven ravninske in STO[110]||Si[100] znotraj ravninske orientacije. Večji del STO plasti ima kubično celico, ki je za 2–5 % večja v primerjavi z volumskim STO, kar je povezano z rahlo nestehiometrijo plasti. Velik del STO plasti je relaksiran zaradi prisotnosti amorfne silikatne plasti na spoju STO-Si, ki se začne tvoriti med nanašanjem prvih 2 ML STO in se širi z vsakim ciklom nanosa, oksidacije in kristalizacije STO in doseže debelino 1,2–1,9 nm po nanosu ~ 10 ML STO.

Kljub temu, da se amorfizaciji spoja STO-Si ni mogoče popolnoma izogniti, se lahko ultratanke plasti STO na Si, pripravljene s tehniko PLD, uporabljajo kot odlična osnova za rast debelejših STO plasti ter epitaksialno integracijo različnih funkcionalnih oksidov s Si tehnologijo.

Contents

List of Figures xv

List of Tables xix

Abbreviations xxi

1 Introduction 1

1.1 Epitaxial Integration of Functional Oxides with Silicon 1
1.2 Buffer Layers 2
1.3 $SrTiO_3$ Thin Films on Silicon 2
1.4 Main Techniques for the Growth of STO on Si 4
1.5 Thesis Outline 5

2 Aim and Hypotheses 7

2.1 Aim 7
2.2 Hypotheses 8

3 Synthesis and Characterization Methods 9

3.1 Pulsed Laser Deposition 9
3.1.1 Materials and the PLD set-up 11
3.1.1.1 Substrates 11
3.1.1.2 Sample holders 11
3.1.1.3 Targets 12
3.1.1.4 PLD setup 12
3.2 Imaging Techniques 14
3.2.1 Scanning tunneling microscopy 14
3.2.1.1 Tunneling current 14
3.2.1.2 Bardeen formalism and the Tersoff-Hamann model 15
3.2.1.3 Imaging semiconducting surfaces 16
3.2.1.4 Calculated STM images 17
3.2.1.5 Equipment and parameters in STM analysis and image calculations 17
3.2.2 Atomic force microscopy 17
3.2.3 Piezoresponse force microscopy 18
3.3 Structure Determination by Diffraction 18
3.3.1 Grazing incidence X-ray diffraction 18
3.3.2 Electron diffraction 19
3.4 X-Ray Reflectivity 20
3.5 X-Ray Photoelectron Spectroscopy 20

4 The Si(001) Surface 23

4.1 Introduction 23

4.1.1 The ideal Si(001) surface ... 24
4.1.2 Surface defects: steps and terraces ... 25
4.2 Surface Morphology of LD and HD Si Substrates ... 26
4.2.1 Methods ... 26
4.2.2 Results and discussion ... 27
4.3 Atomic Structure of Si(001) ... 29
4.3.1 Methods ... 30
4.3.2 Results and discussion ... 30
4.3.2.1 Ni contamination ... 32
4.4 Conclusions ... 34

5 The Sr-Passivated Si(001) Surface 35
5.1 Introduction ... 35
5.1.1 Ordered structures of Sr on the Si(001) surface ... 36
5.2 Properties of the Sr/Si(001)(1×2) Surface ... 37
5.2.1 Methods ... 37
5.2.2 Results and discussion ... 38
5.2.2.1 Controlling the Sr coverage by monitoring Si surface reconstructions ... 38
5.2.2.2 Surface morphology ... 38
5.2.2.3 Atomic structure ... 40
5.2.2.4 Surface defects ... 41
5.2.2.4.1 Type-A defects: Sr vacancies ... 42
5.2.2.4.2 Type-B defects: Sr adatoms ... 42
5.2.2.4.3 Possible adsorbates at the D-site ... 42
5.2.2.4.4 Comparison of surface defects in PLD and MBE grown surfaces ... 43
5.2.2.5 Problems with surface contamination and STM analysis ... 44
5.2.2.6 Chemical composition ... 45
5.3 Deposition of Sr in an Inert Background Gas ... 46
5.3.1 Methods ... 47
5.3.2 Results and discussion ... 47
5.4 Sr Deposition on Heavily Doped Si Substrates ... 48
5.4.1 Methods ... 48
5.4.2 Results and discussion ... 48
5.5 Conclusions ... 50

6 $SrTiO_3$ Thin Films on Si(001) 51
6.1 Introduction ... 51
6.2 Optimization of STO Growth on Si by PLD ... 52
6.2.1 Methods ... 52
6.2.2 Results and discussion ... 53
6.2.2.1 Interface ... 53
6.2.2.2 $SrTiO_3$ (seed) layer ... 55
6.2.2.3 Crystallization temperature ... 59
6.2.2.4 Optimized parameters for PLD of the STO seed layer ... 61
6.3 Properties of STO Ultra-Thin Films ... 62
6.3.1 Methods ... 62
6.3.2 Results and discussion ... 63
6.3.2.1 The STO-Si interface ... 65
6.3.2.2 The STO thin film ... 65

6.3.2.3 Test of functional properties....69
6.3.2.4 Demonstration of the integration of functional oxides....70
6.4 Conclusions....71

7 Summary and Conclusions 73

Appendix A Sample Transfer Using a Vacuum Suitcase 75
A.1 Introduction....75
A.1.1 The vacuum suitcase....76
A.1.2 Modifications of host UHV systems....76
A.1.3 The sample transfer procedure....78
A.2 Test of Sample Transfer....78
A.2.1 Methods 79
A.2.2 Results and discussion....80
A.3 Conclusions....81

Appendix B STM of 2 ML STO on Si 83

References 85

Bibliography 95

Biography 99

List of Figures

Figure 1: Schematic structure of the STO-protected silicon photocathode shows that light is absorbed by the p-silicon substrate and the photogenerated electrons tunnel to the surface metallic dots, at which H_2 is produced. The inset plot represents the interface between STO and Si(001), with a good lattice match [40]. 3
Figure 2: Insight into the deposition chamber taken during deposition of Sr onto a Si substrate heated by an infra-red laser. 10
Figure 3: (a) Design of the sample plate. (b) The sample plate with a mounted Si substrate inserted in a PLD adapter. (c) Design of the XPS adapter with the sample plate. (d) An example of an oxidised Mo sample plate after performing STO homoepitaxy and cooling in high oxygen pressure (~0.02 mbar)..12
Figure 4: A schematic of the PLD system at the Advanced Materials Department (JSI, Ljubljana, Slovenia). 13
Figure 5: Schematics of the STM operation. 14
Figure 6: Tersoff-Hamman model of STM tip with an s-type orbital at the apex. 16
Figure 7: (a) Representation of different primary Si surfaces. Figure from [94]. 24
Figure 8: Schematic diagrams of the Si(001) surface (1×1) unreconstructed (a) and (2×1) reconstructed (b). The darker circles represent the top layer in which the atoms are paired to form dimers. The dashed line shows the projection of the bulk unit cell onto the surface. (c) Schematic diagram of a vicinal Si(001) surface tilted about [110]. The three terraces shown are separated by two monoatomic steps, one type A and the other type B, running from the upper left to the lower right. Note that the dimers, represented by dashed lines, alternate their directions between terraces. The bulk lattice constant is a_0. Figure from [99]. 25
Figure 9: (a) RHEED pattern of an amorphous SiO_2 layer on a Si(001) surface, before deoxidation. (b) RHEED pattern of the Si(001) surface of a LD Si substrate, after deoxidation. (c) RHEED pattern of the Si(001) surface of a HD Si substrate, after deoxidation. The inset shows a part of the image with enhanced brightness. All RHEED patterns were taken in the [100] azimuth. (d) Schematics showing the reciprocal lattice of a double domain (2×1) (green) and (1×2) (orange) structure. The diffraction spots of the zeroth and 1/2 Laue zones in the RHEED patterns shown in (b) and (c) are marked. (e) and (f) LEED patterns of deoxidized LD Si and HD Si surfaces, respectively. 27
Figure 10: (a) and (b) Large area STM images of LD and HD Si(001) surface, respectively. (c) and (d) Comparison of step spacing of LD and HD Si substrates, respectively. (e) and (f) High resolution STM images of LD and HD Si, respectively. 28
Figure 11: (a) Mo sample plate with Si substrate mounted by spot-welding Mo strips. The red U marks the area of the plate that has a limited height in order to fit into the STM. (b) Image taken during a flash at 1200 °C. Not only the sample but also the plate is heated because the spot size of the IR laser on the plate is 1 cm in diameter, which is larger than in the case of IR laser heating in the PLD system at JSI..30

Figure 12: (a) LEED pattern of a (2×1)+(1×2) surface reconstruction. (b) Large-area STM image. (c) STM image of steps and terraces. Contamination from the tip approach is marked. 31
Figure 13: (a) High-resolution empty states STM image. (b) Close up where the main features of the Si(001) surface are marked. 31
Figure 14: (a) XPS survey of the deoxidised Si substrate. (b) High-resolution XPS spectrum in the Si 2p region. 32
Figure 15: (a) A clear (1×2)+(2×1) surface reconstruction after 3 flashes. (b) The surface reconstruction is preserved even after 5 additional flashes (8 flashes total). (c) LEED pattern after a total of 11 flashes exhibiting the (2×n) + (n×2) surface reconstruction. 32
Figure 16: XPS spectra of the deoxidized Si(001) surface after performing 3 (orange) and 11 (green) flashes. 33
Figure 17: Procedure for the preparation of the Sr-passivated Si surface by PLD. RHEED patterns were taken in the [100] azimuth. 36
Figure 18: Si surface reconstruction transitions induced by Sr deposition at high temperatures. 37
Fig. 19. RHEED patterns of the Si(001) surface reconstructions for different Sr coverages (θ_{Sr}) recoded along the [100] high-symmetry direction: (a) (2×1)+(1×2) reconstruction of the deoxidised Si(001). (b) (2×3)+(3×2) reconstruction at θ_{Sr} =1/6 ML. (c) (1×2)+(2×1) reconstruction at θ_{Sr} = 1/2 ML. The Laue zones seen in the RHEED patterns are marked with L_x. 38
Figure 20. (a) Large-scale STM image recorded after the deoxidation of the Si(001) surface and the deposition of ½ ML of Sr. The resulting Sr/Si(001)(1×2) surface exhibits rough-edged terraces, separated by monoatomic steps. (b) Large-scale STM image of a deoxidised Si surface exhibiting straighter A terraces and jagged B terraces. LEED patterns of the Si and Sr-Si surfaces recorded at E=58 eV exhibiting the (2×1)+(1×2) and the equivalent (1×2)+(2×1) surface reconstruction, respectively, are shown in the insets. The STM images were taken at T=60 K, U=2 V and I=50 pA. 39
Figure 21. (a) Filled-state STM image of a Sr/Si(001)(1×2) surface composed of 1D chains running in the [0-11] and [011] directions on neighbouring terraces. Different types of surface defects are marked. (b) A high-resolution filled-state STM image exhibiting corrugation along the 1D chains. The STM images were taken at T=60 K, U=-2V and I=120 pA. 40
Figure 22. Simulated STM images of the Sr/Si(001)(1×2) surface: (a) the ideal structure, (b) with two Sr vacancies, and (c) with two Sr adatoms. (d) Schematics of the atomic model with marked A and D sites. (e) and (f) Magnification of the area I and II of Fig. 21(b) exhibiting an array of Sr vacancies and Sr adatoms, respectively. 41
Figure 23: Simulated filled-state STM images (U=-2 V) of the Sr/Si(001)(1×2) surface with different adatoms adsorbed on the D-site. 43
Figure 24: STM images of ½ ML Sr on Si(001) surface. (a) Large-area image showing steps and terraces. The insets show a RHEED and a LEED pattern of the Sr-Si surface. (b) STM image showing 6 terraces. Elongated features oriented in two principle directions can be observed. (c) A high-resolution STM image showing two neighbouring terraces. The elongated features run in two perpendicular principal directions. 44
Figure 25: XPS spectra of the O 1s, C 1s, and Sr 3d regions for the Sr-passivated Si sample, taken at a take-off angle of 70° (more signal from the surface). 45
Figure 26: (a) XPS spectra of the Si 2p region for a Si substrate before and after the deoxidation and Sr-passivation steps. Take-off angle: 70° (b) Angle-resolved XPS spectra of the Si 2p region for Si substrate after deoxidation and passivation taken at different take-off angles. 46

Figure 27: Fitting of the XPS spectrum of the Sr-Si surface, taken at a 70° take-off angle. 46
Figure 28: (a) RHEED patterns taken in the [100] azimuth of (i) a bare Si surface in UHV, (ii) a bare Si surface in Ar, the Si surface after deposition of (iii) 40, (iv) 60, (v) and 90 pulses in Ar, (vi) and a RHEED pattern of the final Sr-Si surface taken in UHV. (b) STM image of a slightly oxidised the Sr-Si surface. (c) Measurement of Ar and O_2 partial pressures as a function of time. Two events when the total pressure was increased by an operator are marked. 47
Figure 29: (a)–(c) STM images of the Sr/Si(001) surface prepared by Sr deposition on an HD Si substrate. The inset in (a) shows RHEED (left) and LEED (right) patterns of the (1×2)+(2×1) reconstruction at θ=1/2 ML Sr coverage. 49
Figure 30: Comparison of RHEED, LEED and STM analysis results of a 1/2 ML Sr/Si(001) surface formed on a heavily and lightly doped Si substrate....50
Figure 31: (a) XPS spectra of the Si 2p region for all the samples studied. Take-off angle of all the spectra: 20°. (b) XPS Si 2p region spectra fittings for samples $S_{PR,1}$ and $S_{PR,2}$. (c)-(e) Normalized (with respect to the bulk substrate signal) intensity of the Si^{2+} and Si^{3+} contributions for all samples....53
Figure 32: (a) XRR spectra for all the samples studied in this section. 54
Figure 33: RHEED patterns for (a) S_{REC} an (b) S_{OX}, after the final crystallization. The respective coverages can be found in Table 6. 55
Figure 34: FWHM of the (00) streak in RHEED patterns and temperature of the sample at the time of appearance of streaks for (a) S_{REC} and (b) S_{OX} samples. 56
Figure 35: AFM images for samples $S_{REC,1}$ and $S_{OX,3}$. (b) RMS values for S_{REC} and S_{OX} samples. 57
Figure 36: XPS spectra of the O 1s, Sr 3d and Ti 2p regions of all the samples, taken at a take-off angle of 20°. 58
Figure 37: (a) Examples of fittings for the O 1s, Ti 2p and Sr 3d spectra of sample $S_{REC,1}$ (b) O, Sr, Ti atomic fractions for all the samples studied. 58
Figure 38: (a) RHEED patterns after the final crystallization of the S_{TR} samples, taken in the [100] azimuth. (b) FWHM of the (00) streak after the final crystallization. 59
Figure 39: (a) XRR data of the S_{TR} samples with fittings. (b) Density of the S_{TR} samples, as obtained from the fittings of the XRR data. The nominal STO density (5.11 g cm^{-1}) is marked with a horizontal dashed line. 60
Figure 40: XRR data and fitting. 62
Figure 41: RHEED patterns of the surfaces of samples S_{CY} taken: (a) before STO deposition, (b) after the deposition of 2 ML STO film, and (c) after the final crystallization for all four samples. The negatives of the original RHEED pattern images are presented to allow for a higher resolution of the figure in the printed version of this work....64
Figure 42: XPS results for samples S_{CY}....64
Figure 43: (a) XPS Si 2p region for samples S_{CY}. (b) Silicate/Si substrate peak area ratio as a function of number of D-O-R cycles....65
Figure 44: (a) K-L RSM of sample $S_{CY,4}$. (b) Magnification of the area marked in (a) with the (101) STO peak. The K, L values corresponding to the STO bulk lattice parameters are marked by a black dot. The black line represents pairs of K, L values corresponding to a constant unit cell volume equal to STO bulk unit cell volume, assuming H=K. The coloured lines marked with numbers represent 3 line profiles for 3 representative parts of the STO reflection. (c) A RSM taken at L=1.37. (d) L-Scan at H=K=0.987. Data points are marked with blue circles, while the red line represents the Gaussian curve fit. The analysis was performed using synchrotron radiation with a photon energy of 20 keV. 66
Figure 45: XPS spectra of the O 1s, Ti 2p, C 1s and Sr 3d regions of sample $S_{CY,4}$. 67
Figure 46: Fittings for O 1s, Ti 2p and Sr 3d spectra for sample $S_{CY,4}$. 68

Figure 47: XRR data and fitting for sample $S_{CY,4}$. The analysis was performed using synchrotron radiation with a photon energy of 20 keV.. 68
Figure 48: Results of PFM analysis of sample $S_{CY,4}$: (a) Topography-height image. (b) Topography-deflection image. (c) PFM mode – vertical amplitude. (d) PFM mode – lateral amplitude. 70
Figure 49: (a) Schematics of the vacuum suitcase. (b) The 3 sample plates (from total 6) can be inserted by rotating the transfer rod by 180°. 76
Figure 50: (a) Design of a docking station for the vacuum suitcase at the PLD system. (b) Protective stand. (c) Preparations for the bake-out of the buffer volume....................... 77
Figure 51: Schematics of different UHV system-vacuum suitcase connections with marked sample paths. The host UHV systems shown in the schematics are: (a) the PLD system, (b) the XPS system, and (c) the STM system. The vacuum suitcase is coloured blue and orange marks the vacuum equipment that was added to the existing UHV systems....... 77
Figure 52: A chart showing the Cu(111) surface exposure at every step performed during the 2nd transfer test from the STM system to the PLD system and back using the vacuum suitcase. 80
Figure 53: Results of STM analysis. (a) and (b) STM images of Cu(111) surface after cleaning. (c) STM image of the Cu(111) surface after the 1st transfer test. (d) and (e) STM images of the Cu(111) surface after the 2nd transfer test. The two insets in (e) show a transition from a double to a single apex STM tip after applying a bias pulse. 81
Figure 54: (a) RHEED of the Sr-passivated Si surface exhibiting the (1×2) + (2×1) surface reconstruction. (b) RHEED pattern after the deposition of a 2 ML of STO. (c) Large scale STM image of the STO film surface. (d) A magnification of a part of the STO film surface. 83

List of Tables

Table 1: Comparison of main features of typical PLD and MBE systems [3]....................10
Table 2: Properties of the two types of Si substrates with different dopant concentrations. 11
Table 3: Step densities of Si(001) surfaces with monoatomic steps for different miscut angles. 29
Table 4: Comparison of base pressures in the TU Wien and JSI PLD systems at different stages of the thermal deoxidation procedure. 29
Table 5: Fixed parameters used for the Sr deposition and growth of STO. 52
Table 6: Variable deposition parameters for all samples in this study. 52
Table 7: XRR fitting results for the silicate layer..54
Table 8: XRR fitting results for the STO layer. 57
Table 9: XRR results for samples S_{TR}...60
Table 10: Sr, O and Ti atomic percentages of samples $S_{TR,}$ as extracted from XPS fitting calculations. 60
Table 11: Growth parameters for samples S_{CY}...63
Table 12: Values for 3 different regions. 67
Table 13: Results of XRR analysis for sample $S_{CY,4}$..69

Abbreviations

AFM	...	atomic force microscopy
ALD	...	atomic layer deposition
DFT	...	density functional theory
D-O-C	...	deposition-oxidation-crystallization
ESRF	...	European Synchrotron Radiation Facility
fcc	...	face centre cubic
FE	...	ferroelectric
FWHM	...	full width at half maximum
GIXRD	...	grazing incidence X-ray diffraction
HD	...	highly doped
IR	...	infrared
JSI	...	Jožef Stefan Institute
LD	...	lightly doped
LEED	...	low-energy electron diffraction
LL	...	load-lock
LT	...	low temperature
MBE	...	molecular beam epitaxy
PFM	...	piezoresponse force microscopy
PLD	...	pulsed laser deposition
PVD	...	physical vapour deposition
RHEED	...	reflection high-energy electron diffraction
RMS	...	root-mean-square
RSM	...	reciprocal space mapping
RT	...	room temperature
SL	...	superlattices
STM	...	scanning tunneling microscopy
STO	...	$SrTiO_3$
TSST	...	Twente Solid State Technology
TU Wien	...	Vienna University of Technology
UHV	...	ultra-high vacuum
UV	...	ultraviolet
XPS	...	X-ray photoelectron spectroscopy
XRD	...	X-ray diffraction
XRR	...	X-ray reflectivity

Chapter 1

Introduction

The need to develop electronic devices with new and improved capabilities is the driving force behind a large part of today's research. Devices are becoming smaller, more powerful, and combine various functionalities in a single unit. Most of the present electronic devices are based on silicon. Silicon circuits are capable of advanced logic operations and data storage but do not exhibit special functional properties on their own. One of the great challenges of science in the 21st century is to find new strategies, concepts, and materials that would enhance silicon-based semiconductor technologies and thus contribute to technological progress [1].

1.1 Epitaxial Integration of Functional Oxides with Silicon

A group of materials that offers a wide range of functional properties including high-temperature superconductivity, piezoelectricity, ferroelectricity, magnetism, multiferroicity, and colossal magnetoresistance are complex metal oxides. Many of these oxides exhibit a perovskite structure, represented by the general formula ABO_3. By altering the composition of the A- and B-site cations, materials with a wide variety of physical properties can be realized [2].

With the advance of vacuum deposition techniques, layers of oxide material can be deposited on solid surfaces with atomic precision [3]. By using crystalline substrates, epitaxial growth, i.e. the oriented growth of one crystal upon another crystal, can be achieved [4]. Epitaxial thin films often exhibit superior properties compared to ceramic material. Even more, different symmetry constraints at the interface between oxide materials can be used to design structures exhibiting phenomena not found in the bulk constituents [5].

Epitaxial perovskite oxide films are generally grown on single crystalline perovskite substrates due to their matching structure [6]. However, as cost-effective approaches to produce large-scale single crystal oxide substrates are presently not available, silicon is considered as the foremost ideal physical platform by which oxides can be introduced to device technologies [7]. The studies of the growth of oxides on silicon, therefore, represent an important subject for the research community [7]–[9].

When depositing oxide thin films on silicon, epitaxial growth of crystalline material should be achieved. Only so can the functional physical features originating from the structural and chemical properties of oxide material be fully exploited. However, epitaxial integration of oxides with silicon is not trivial. First, there is a noteworthy symmetry difference between the diamond lattice of silicon and the simple cubic lattice of a perovskite. Secondly, the thermal mismatch should be considered, because the difference in the thermal expansion coefficients of perovskite oxides and silicon can be quite large [8], which can

result in huge stress induced in oxide films upon cooling following their deposition at high temperatures. The lattice mismatch between the oxides and silicon is a less critical problem. Although silicon is a rigid material due to its highly-oriented covalent bonds, oxides are generally more tolerant of strain. The ionic bonds in perovskite oxides are somewhat less sensitive to bond angle variations as long as the interatomic distances are maintained [8]. Additionally, there are extra degrees of freedom in complex oxides, e.g. the lattice parameters of an oxide can change by incorporating oxygen vacancies into the crystal structure [10].

1.2 Buffer Layers

Most of these issues can be avoided by using buffer layers. Buffer layers are used to impart the strain induced by lattice and thermal mismatch. The two most often used buffer layers are $SrTiO_3$ (STO) and yttria-stabilized zirconia (YSZ) [11]. These buffer layers have enabled epitaxial integration of many relevant oxides including ferroelectric $Bi_{3.25}La_{0.75}Ti_3O_{12}$ [12] and $BaTiO_3$ [13]–[15], piezoelectric $Pb(Mg_{1/3}Nb_{2/3})O_3$-$PbTiO_3$ [16], ferromagnetic manganites [17], and spinels [18] and the $LaAlO_3$/STO superstructures on Si(001) exhibiting two-dimensional (2D) electron gas at the $LaAlO_3$-STO interfaces [19].

The key problem unique to heteroepitaxy of perovskite oxides with silicon is the thermodynamic instability of oxide films in contact with silicon. A bare silicon substrate will form half a monolayer (ML) of amorphous SiO_2 when exposed for ~10 s to an oxygen pressure of $\sim 2.5\times10^{-6}$ mbar at room temperature [20]. Uncontrolled reactions at the oxide-silicon interface occurring during the film growth can degrade the quality of the growing film or even completely prevent epitaxy. Therefore, a pure silicon surface needs to be passivated prior to the deposition of oxide films. Deposition of divalent metals like Sr, Ba and Eu with submonolayer coverage is mostly used to fill the dangling bonds of the Si(001) surface that are the source of its high reactivity [21].

Epitaxial growth has been achieved for many different oxide thin films on silicon, however, a thin amorphous SiO_x layer is often formed at the buffer-silicon interface, which is undesirable for certain applications. For example in the case of EuO thin films on Si, where EuO is considered as a prospective spin injector for the new generation of spintronic devices, the coherent injection of spin-polarized carriers can only be achieved by obtaining an atomically abrupt oxide-silicon interface [22]. Achieving an atomically abrupt interface that enables charge transfer across the oxide-silicon junction represents an additional challenge in the oxide-silicon integration and only a small number of oxide materials have been grown directly on silicon without the formation of an amorphous interlayer, such as γ-Al_2O_3 on Si(001) [23], YSZ on Si(111) [11], $(La_xY_{1-x})_2O_3$ on Si(111) [24], Sc_2O_3 on Si(111) [25], EuO on Si(111) [26], and STO on Si(001) [27].

1.3 $SrTiO_3$ Thin Films on Silicon

The most extensively studied buffer layer is STO. A procedure to grow STO directly on silicon was first introduced by McKee and co-workers [28], and studied in detail by many groups [29]–[33]. The large interest in the epitaxial growth of STO on silicon started already in the 90s when researchers were looking for an alternative high-k dielectric that would replace SiO_2 as a gate in metal-oxide-semiconductor field-effect transistors (MOSFETs) [34]. At that time, the semiconductor industry was facing the challenge to continue the scaling of MOSFETs in order to maintain the trend predicted by Moore's law [35]. However, different materials like amorphous HfO_2 films [36] showed better properties and

were easier to implement by industry, which shifted the studies of the STO-silicon system elsewhere.

Nowadays, STO on silicon is being generally used as a pseudo-substrate for the epitaxial growth of multifunctional oxides because its unit cell closely matches a large number of other perovskite materials. Extensive reviews of many different materials that have been integrated with silicon are given in references [9] and [7].

In addition to the possibility of using STO thin films as dielectrics and buffer layers for functional oxide overgrowth, ferroelectric functionality was also shown for ultra-thin films of STO on silicon. Although bulk STO is not ferroelectric at any temperature, the ferroelectricity of the thin films can be induced by epitaxial strain, which is formed as a result of ~1.7% lattice mismatch between STO and silicon. Theoretical studies have predicted STO to exhibit ferroelectricity at room temperature under compressive strain [37], which was confirmed by an experimental study by Waruswithsana et al. [38]. They found that ultra-thin STO films of thicknesses ranging from 5-10 ML exhibit switchable contrast in the amplitude response of the piezoresponse force microscopy (PFM) signal, consistent with ferroelectricity [27] (Fig. 1). However, it was also found that the ferroelectricity can be easily diminished if an amorphous SiO_x layer is formed at the STO-silicon interface which relaxes the compressive strain initially induced by the STO-silicon lattice mismatch [33].

Furthermore, STO thin films are also considered as a corrosion-resistant protective layer for silicon substrates that can provide a stable surface for hydrogen evolution from water. Silicon offers a relatively small bandgap that is ideal for the generation of electron-hole pairs from sunlight [7]. Unfortunately, this semiconductor material tends to photo-corrode under photocatalytic conditions [39]. Ji et al. were the first to demonstrate this possibility in a stacked heterostructure comprised of a p-type silicon base, and an epitaxial STO layer covered by a nanostructured Pt/Ti bilayer [40] (Fig. 2). Given the near proximity between the conduction bands of silicon and STO, photo-generated electrons from the silicon base were transported through the STO layer for reaction at the surface achieving a large photocurrent density.

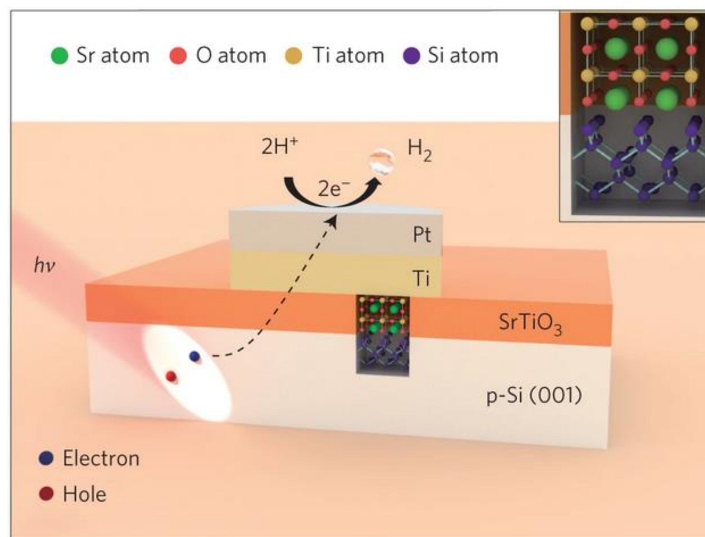

Figure 1: Schematic structure of the STO-protected silicon photocathode shows that light is absorbed by the p-silicon substrate and the photogenerated electrons tunnel to the surface metallic dots, at which H_2 is produced. The inset plot represents the interface between STO and Si(001), with a good lattice match [40].

However, the STO-silicon interface needs to be near perfect to allow electron transport while the absence of an amorphous SiO_x interlayer is crucial for preserving ferroelectric properties. Furthermore, in order to use the STO thin films deposited on silicon as pseudo-substrates, the structural properties of the films should resemble the properties of STO single-crystals, while their surfaces should be smooth and well-defined to enable epitaxial overgrowth. Therefore, not only growth control but also surface and interface engineering at the atomic level is important.

1.4 Main Techniques for the Growth of STO on Si

The main techniques used for the growth of STO on silicon are molecular beam epitaxy (MBE), atomic layer deposition (ALD) and pulsed laser deposition (PLD). MBE is especially suitable for epitaxial growth due to its slow rate in a controlled environment provided by ultra-high vacuum (UHV) conditions. For the growth of STO thin films on Si, MBE has been the prevailing technique. So far, atomically abrupt STO-silicon interfaces have been realized only using MBE, while the epitaxial integration of STO with silicon has been demonstrated on 200 nm silicon wafers using an industry-scale MBE system [41]. However, the limiting oxygen process pressures become problematic when MBE is used for the overgrowth of STO-silicon pseudo-substrates with functional oxides.

Recently, great progress has been made by depositing STO on silicon using ALD [42]. The main advantages of this technique are the low process temperatures and high scalability. The development of an all-ALD process would allow scalable integration of functional oxides with silicon, however, this would first require a successful integration of ALD-compatible buffer layers with silicon [7]. Zhang et al. have demonstrated the passivation of the Si(001) surface by 1/2 ML of Sr using HyperSr [$Sr(C_5Pr_3H_2)_2$] and H_2O as precursors, followed by a high temperature (800–850 °C) anneal [43]. However, the consequent growth of high quality films on the ALD-grown Sr-silicon templates remains challenging due to the formation of an interfacial SiO_2 layer [42]. To avoid this limitation, McDaniel et al. used ALD to grow epitaxial STO films on Si(001) substrates with a thin STO buffer layer grown by MBE [42].

Another technique that shows great potential for its use at the industrial scale is PLD [44], [45]. This vacuum deposition technique is currently the most common tool for oxide epitaxy on oxide substrates, owing to its relative ease of operation and wide span of possible materials [46], [47]. Despite showing less potential for industrial use compared to ALD, its widespread application in research makes it very attractive for oxide epitaxy on Si. Compared to the MBE technique, PLD offers precise stoichiometry control of the metals composing complex oxide films and higher oxygen environment compared to the classical MBE approach. Many functional oxides have been successfully integrated on silicon using PLD in combination with MBE-grown STO-silicon pseudo-substrates [48]–[50], however there have been only few attempts of growing STO directly on silicon by PLD [51]–[53].

Mimicking the successful MBE integration of STO on silicon [28], recently Klement and co-workers introduced a procedure for the growth of STO thin films on the Si(001) surface using the PLD technique showing promising results [35], [54]. The complex procedure can be divided into three main steps: the thermal removal of the amorphous SiO_2 layer from the silicon substrate (deoxidation), deposition of elemental Sr on a clean and reconstructed Si(001) surface (formation of the Sr-buffer layer) and the STO overgrowth using the so-called "kinetically controlled sequential deposition (KCSD)" method. The authors performed a detailed study of the initial deposition parameters in terms of the background gas, pressures, deposition temperature, fluence and the oxidation peculiarities. However,

the films exhibited a slight non-stoichiometry, low density and unideal crystal properties together with a 2.3 nm thick silicate layer at the STO-silicon interface.

High crystallinity, together with exact stoichiometry, high density, presence of a single phase and high surface smoothness are desired properties for the use of STO thin films on silicon as pseudo-substrates, while the presence of an atomically sharp STO-silicon interface represents an additional demand for the emergence of certain functional properties in the STO ultra-thin films. Therefore, the work presented in this thesis focuses on the mechanisms of the PLD growth of the first few STO layers on Si, the reactions occurring at the STO-silicon interface, and the optimization of the key growth parameters in order to further improve the film crystallinity and to enhance the structure of the STO-silicon interface prepared by PLD.

1.5 Thesis Outline

The thesis is divided as follows. The introductory Chapter 1 deals with the purpose of the dissertation followed by the goals and hypothesis presented in Chapter 2. The details of the materials and the methods used for the preparation and characterization are given in Chapter 3. In Chapter 4, the results of the analysis of surface properties of two types of silicon substrates used throughout the presented work are given. In Chapter 5, the details of the preparation of the Sr-passivated Si(001) surface using the PLD technique are explained together with its morphology, atomic structure, surface defects and chemical composition. In Chapter 6, the results of the optimization of some key parameters for the growth of ultra-thin STO films on Sr-silicon surfaces using PLD are presented followed by a study of the evolution of the STO-silicon interface structures. Final conclusions are given in Chapter 7. Additionally, the method and equipment used for transferring samples under UHV conditions are presented in Appendix A.

Chapter 2

Aim and Hypotheses

2.1 Aim

The aim of this thesis is to study the structural and chemical properties of the surfaces, interfaces and thin films formed in the process of growing STO on a Sr-passivated Si(001) surface in an all-PLD procedure. The gained knowledge can be used in the optimization of the growth procedure for the preparation of thicker high-quality STO thin films on silicon (Si) using the PLD technique. Such heterostructures can be used to bring diverse properties of functional oxides to the well-developed semiconductor technology. This combination of Si and oxide materials is heralded as the next step in the development of novel electronic devices.

For that purpose, combining various state-of-the-art techniques, I would answer the following questions:

- Is the native SiO_2 layer completely removed from the Si surface after the deoxidation step?
- Is the clean Si surface stable enough to avoid reactions with the oxygen from the residual atmosphere before its passivation with Sr?
- What is the morphology and the atomic structure of the Sr-passivated Si surface prepared using PLD? Are there any surface defects present? If so, what are their types, their origin and what is their overall density?
- How and why is the Sr/Si(001) surface prepared with PLD different from the surfaces prepared by the MBE technique?
- How do the individual deposition parameters in the PLD growth of STO on Si affect the crystallinity, density and stoichiometry of STO thin films? What are the optimal growth parameters for PLD of STO on Si?
- What is the structure of the STO-Si interface and at which steps of the growth is the interface disrupted the most?
- Is it possible to prepare STO thin films on Si with an atomically abrupt interface using the PLD technique? Do such films exhibit ferroelectric properties?

2.2 Hypotheses

Hypothesis 1: By upgrading the vacuum equipment of the PLD, XPS and STM systems at the Jožef Stefan Institute (JSI) and establishing a suitable procedure for sample transfer under UHV conditions, detailed analysis of surfaces prepared by PLD can be achieved.

Hypothesis 2: By careful optimization of PLD parameters based on results of surface analysis, it is possible to prepare Sr-passivated Si surfaces exhibiting a high level of crystallinity, smoothness and low defect density that enable epitaxial growth of STO thin films.

Hypothesis 3: It is expected that by tuning the deposition parameters, the procedure for the PLD growth of STO thin films on Si can be optimized and the structural and consequently the functional properties of the thin films can be enhanced.

Hypothesis 4: High temperatures and long time periods during the crystallization of the STO film lead to extended interface reactions while a certain amount of heat is needed for sufficient densification of the STO layer. Therefore, it is anticipated that by optimizing the overall thermal budget of the procedure for the growth of STO on Si by PLD, the reactions at the STO-Si interface can be decreased while reaching a high density of the STO layer.

Chapter 3

Synthesis and Characterization Methods

This chapter introduces the techniques and methodologies used for the growth, processing, and characterization of the STO/Sr/Si, Sr/Si heterostructures, and Si(001) surface studied in this work. The basic description of the PLD technique is given, followed by a brief theoretical background for scanning tunneling microscopy (STM). The chapter concludes by introducing the basic principles of a variety of conventional and advanced techniques used for additional characterization of the structure, chemistry, surface morphology, and ferroelectric properties of the prepared surfaces and thin films, together with the equipment and parameters used in the analysis.

3.1 Pulsed Laser Deposition

PLD is a physical vapour deposition (PVD) technique used for the growth of different heterostructures in the form of thin films [55]. This technique was first introduced soon after the technical realization of the first laser in the 1960s and reached a breakthrough in 1987 when the growth of high-temperature superconductors with superior quality was achieved [56]. Nowadays, PLD is widely used to prepare thin films and multilayer structures of metals, insulators and semiconductors, polymers, and even biological materials. For many systems, PLD offers superior film properties in comparison to films deposited by other PVD techniques which has been especially evident in the use of PLD for the epitaxial growth of multicomponent metal oxides [46].

PLD growth is carried out in a vacuum chamber as shown in Fig. 2. A pulsed laser beam is used to rapidly heat and evaporate a target material that is then transferred to a substrate where it condenses in the form of a thin layer. When a laser pulse hits the target, a dense layer of vapour is formed close to the target surface. This ionized vapour, which then expands from the target surface towards the substrate, is called a plasma plume.

The plasma plume consists of a mixture of energetic species including atoms, molecules, electrons, ions, clusters, micron-sized solid particulates, and molten globules. The kinetic energy of these particles can be as high as several hundred eV. To prevent sputtering of the substrate surface during the film growth, the velocity of the plume particles can be decreased by introducing a background gas. A background gas can also be introduced as a reactive medium. In the case of oxide film growth, an oxygen background pressure is used, so it can be incorporated into the grown layer together with the target material to achieve sufficient oxidation of the deposited material. It is possible to use different background gases or their mixtures over a wide pressure range. High-quality growth by PLD is not

straightforward. In order to achieve the desired properties of deposited material, many parameters need to be tuned, e.g.: energy density (fluence) of the laser light, laser spot size, pulse frequency, target-substrate distance, substrate temperature, background pressure, and the type (or mixture) of the background gas.

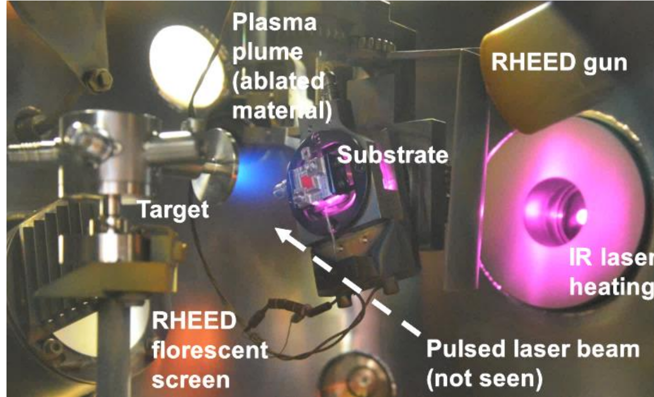

Figure 2: Insight into the deposition chamber taken during deposition of Sr onto a Si substrate heated by an infra-red laser.

PLD is operationally simple, orders of magnitude faster, and more versatile than any other PVD technique. The main benefits of using PLD for the growth of complex oxide material are the stoichiometric transfer of material from the target and the use of high oxygen background pressure up to 1 mbar. Furthermore, recently large-scale industrial PLD systems have also been demonstrated [45]. The main disadvantage of this technique is the possibility of ejecting µm-sized particulates from the target that are then incorporated in the ablated films. At the industrial scale, particulate reduction is being achieved mechanically through the use of particle filters [57].

Apart from PLD, the most common PVD techniques are MBE and sputter deposition. In MBE, the materials are sublimated from effusion cells, forming a molecular beam, which is deposited on an independently heated substrate at thermal energies. The absence of carrier gases, as well as the UHV environment, result in the highest achievable purity of the grown films. On the other hand, oxygen sources can be incorporated for depositing oxide materials but only in the low-pressure range. Because of its purity and gentle deposition of material, the MBE is the most commonly used technique at a laboratory scale, especially when it comes to basic research. However, the technique has its disadvantages that limit its potential use at an industrial scale, e.g. the slow growth rate and the constraints in the use of process gases at high pressures. In MBE, the material evaporated from effusion cells arrives at the substrate surface at thermal energies (0.1 eV), while in typical PLD systems, a high-energy laser pulse can generate a plume of supersaturated species that hit the surface at much higher kinetic energies (up to 1000 eV) if the deposition is carried out in vacuum. The main differences between the MBE and PLD deposition techniques are presented in (Table 1).

Table 1: Comparison of main features of typical PLD and MBE systems [3].

Method	**Energy range (eV)**	**Vacuum requirement**	**Multi-element rate control**	**Deposition rate (nm/s)**	**p > 1 mbar reactive gas**
MBE	0.1	UHV	Moderate	0.3	No
PLD	1-1000	HV	Easy	1	Yes

3.1.1 Materials and the PLD set-up

3.1.1.1 Substrates

Silicon substrates were used for the deposition of Sr and STO by PLD. The 5 mm × 5 mm substrates were cut from 200 mm diameter commercial wafers (Si-Mat, Germany) with a thickness of 525 µm (+/- 25 µm), single side polish and cut in the 100 direction (+/- 0.1°). Two sets of p-type Si(001) substrates with different concentrations of B dopants were used (Table 2). The thickness of the SiO_2 layer on the LD Si substrates was 2.0 +/- 0.2 nm [35]. The substrates were sonicated in acetone (5 min), rinsed with ethanol, and clamped with metal clips to a custom-built sample holder with a hole that allowed unobstructed heating of the substrate from the backside.

Table 2: Properties of the two types of Si substrates with different dopant concentrations.

	Lightly doped (LD)	**Highly doped (HD)**
Dopant concentration (at/cm^3)	1×10^{16}	1×10^{19}
Atom ratio (N_B : N_{Si})	1:1000 000	1:1000
Conductivity (ohm^{-1}) at RT	0.25	200

3.1.1.2 Sample holders

The choice of sample plate material for working with Si is quite limited. Any use of stainless steel (standard sample plate material) must be avoided as it contains different metal impurities (e.g. Ni, Fe, Cu) that can permanently contaminate the Si surface [58]. In addition, the material must have a melting point well above 1200 °C at which thermal deoxidation of Si takes place. Two materials that meet the listed requirements are high purity Mo and Ta. Therefore, all experiments were performed using a custom-made Ta (or Mo) sample holder with Mo (or Ta) screws and Ta (or Mo) washers. To prevent potential merging of the parts at high temperatures, a combination of different plate and screw materials was used.

The sample plates were manufactured by spark-erosion following a special design (Fig. 3). The plate is designed in a way that allows mounting subsequent substrates (it is reusable). The dimensions of the plates were adjusted so they can nicely fit in a PLD chamber, a vacuum suitcase, an XPS, and STM systems (presented in this chapter). The elevated central part of the plate allows for RHEED analysis at different azimuth angles. The bottoms of the plates were polished to enable easier transferring between the UHV systems. The smoothness of the plates is especially important for their manipulation in the STM system. Special adapters are used for handling the sample plates in the XPS and the PLD systems (Fig. 10 (b) and (c)). Before using the plates in experiments, the parts were thoroughly cleaned, first by sonification in soap (15 min), acetone (15 min), and ethanol (5 min). Then a dummy Si substrate was mounted on a plate, which was degassed at 650 °C for 72 h in a UHV chamber, followed by several flash annealings to 1200 °C to remove potential impurities [59]. It is worth noting that the use of Mo (and also Ta) in high oxygen pressures (O_2 pressure > 10^{-2} mbar for T > 400 °C) should be avoided as it leads to strong oxidation. Thus, for PLD of typical perovskite oxide films, a different sample plate should be used. In the growth of STO presented in this thesis, this was not an issue, as only very low oxygen pressures were used.

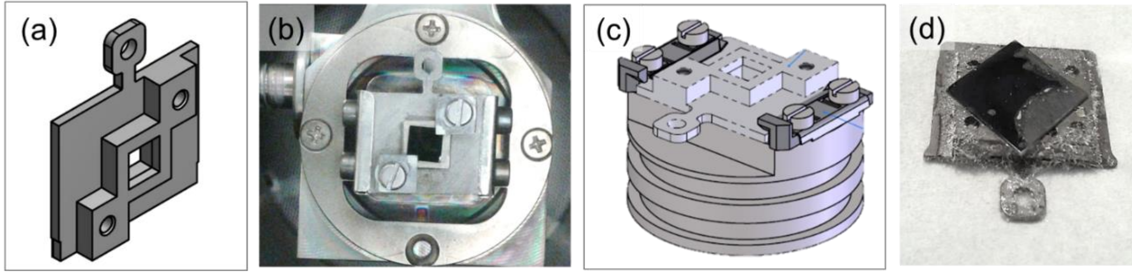

Figure 3: (a) Design of the sample plate. (b) The sample plate with a mounted Si substrate inserted in a PLD adapter. (c) Design of the XPS adapter with the sample plate. (d) An example of an oxidised Mo sample plate after performing STO homoepitaxy and cooling in high oxygen pressure (~0.02 mbar).

3.1.1.3 Targets

For the preparation of Sr-passivated Si surfaces, a strontium target with 99.9% purity (MaTecK, Germany) was used. Due to the high reactivity of elemental Sr, the target was stored in the glove-box with a N_2 atmosphere and inserted into the PLD chamber without exposure to air. A single crystal STO target (Plasmaterials, USA) was used as a source material for the deposition of STO thin films. The targets were preablated in UHV before every deposition.

3.1.1.4 PLD setup

Experiments were performed in a custom-made PLD system from Twente Solid State Technology (TSST) that consists of a vacuum chamber for deposition and a load-lock with a connection to a glove-box, which enables storage and transfer of reactive targets (elemental Sr) in N_2 atmosphere as shown in Fig. 4. Before every experiment, the PLD chamber was baked, which resulted in a base pressure of 2×10^{-9} mbar, with H_2, He, H_2O, O_2, and CO_2 being the main components of the residual gas. The deposition chamber is connected to an adjacent transfer chamber with a base pressure below 1×10^{-10} mbar. The transfer chamber also hosts a sample storage system and is connected to a docking station for a vacuum suitcase, which enables sample transfer under UHV conditions (see Appendix A).

A pulsed KrF excimer UV laser (Coherent COMPexPro 205) with a wavelength of 248 nm and a typical pulse duration of 20 ns was used for ablation. The laser beam passes through an attenuator module (Coherent) that allows adjustment of the UV pulse energy. The light continues its way through a mask placed in the central part of the beam that creates a homogeneous rectangular beam profile. Several optical mirrors are used to lead the laser light to a focusing lens placed before the deposition chamber. The lens-target distance is carefully adjusted to place the target in the focal spot of the lens. The size of the laser spot on the target is defined by the dimensions of the opening in the mask and the magnification which is determined by the mask-lens distance and the focal length of the lens. The energy density (fluence) on the target is set by measuring the energy of the UV beam passing through the laser window (quartz), the deposition chamber, and an energy-measurement window (outside of vacuum using a Coherent LabMax Top energy meter). This way the attenuation of the UV light by the entry window, caused by the contamination of the windows and other losses along the optical path, is taken into account. During depositions, the energy-measurement window can be protected from the plasma plume by closing a valve between the window and the deposition chamber.

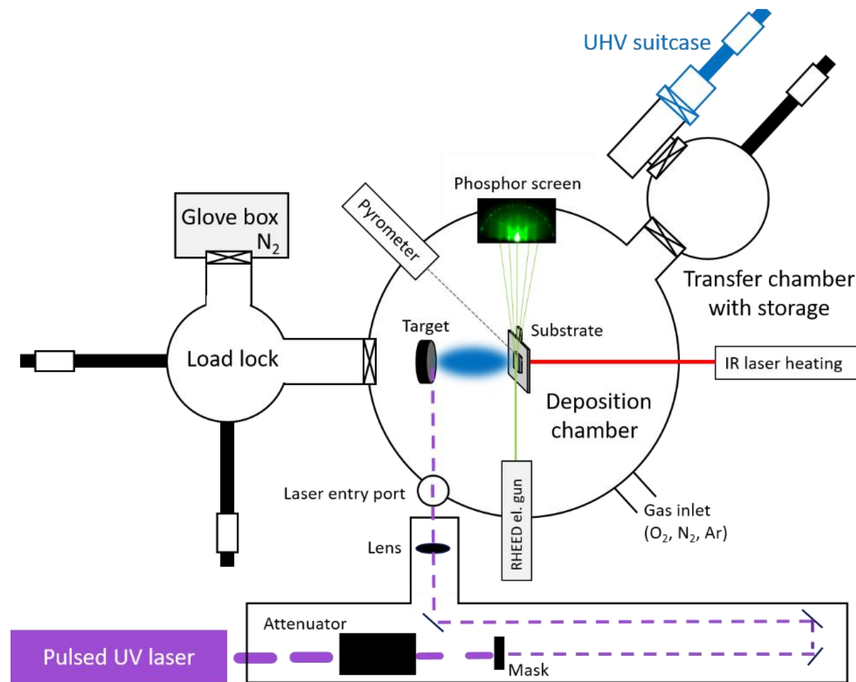

Figure 4: A schematic of the PLD system at the Advanced Materials Department (JSI, Ljubljana, Slovenia).

Up to five targets can be mounted on a detachable target holder, which can be transferred from the glove box into the deposition chamber without exposure to atmosphere. *In situ* target exchange is possible by rotating the target holder. The targets are scanned during laser ablation to decrease the emission of larger particulates. The substrates are mounted on specially designed sample plates (Omicron style) that can be heated by a continuous-wave near-infrared (IR) laser (Coherent, wavelength 800-820 nm) directed onto the back of the substrate through a hole in the sample plate. Direct heating of the substrate is crucial for obtaining a uniform temperature profile as it also helps to decrease the degassing of the sample holder. The temperatures are measured with an optical pyrometer (IMPAC, RS485) aimed at the substrate surface. The emissivity of 85% and 30% was used for Si and STO surfaces, respectively.

The deposition chamber is equipped with a differentially pumped RHEED system, which allows *in situ* observations of surface reconstructions and monitoring RHEED oscillations in up to 1 mbar oxygen pressure. Several different background gasses can be used: O_2 (purity 5.5), N_2 (purity 5.0), and Ar (purity 6.0). Gases are introduced into the PLD chamber by mass flow controllers (Brooks Instruments) that can be used for the regulation of pressures in the range from 10^{-6} mbar up to 5 bar. The pressure regulation is implemented by setting the mass flow controllers and by partially closing the motorized gate vale (to the same position for every set of experiments). Regulation in the low-pressure range (10^{-7} - 10^{-9} mbar) can be provided by a needle valve. Pressures of up to 5×10^{-5} mbar are measured with a Bayard-Alpert ion gauge (VG Scienta) while higher pressures are monitored simultaneously by a Pirani (Pfeiffer) and a capacitive (MKS Baratron) gauge. The system is mainly controlled by software from TSST and a personal computer.

3.2 Imaging Techniques

3.2.1 Scanning tunneling microscopy

STM is a precise analysis technique used for imaging conducting and semiconducting surfaces [60]. The most important feature of STM is the ability to provide local information, ultimately with atomic resolution, directly in real-space, in contrast to diffraction techniques, which provide only averaged information of extended periodic structures. Real-space information is particularly important for the study of defects (e.g. steps, dislocations, vacancies, impurity sites) and other chemical inhomogeneities.

While STM analysis can be performed in air or even in liquid, a UHV environment is typically provided in order to guarantee uncontaminated surfaces. STM measurements can also be performed over a wide range of temperatures, from less than 1 K to more than 1000 K [61]. The main advantages of using a low temperature (LT) STM are improved tunneling stability and reduced thermal drift, i.e., reduced mobility of surface atoms and surface adsorbates enabling stability of surfaces at the atomic level. Although in principle, STM is limited to conductors and semiconductors, it can also be applied to thin films of insulators supported on conductive substrates [62].

The microscope's probe is an atomically sharp metal tip approached to the sample surface in separation less than a nm. When a bias voltage is applied between the tip and the sample, an electron current can flow through the vacuum gap separating the two electrodes due to the quantum tunneling effect [60]. This tunneling current can be used to probe local physical properties at the sample surface as well as to control the separation between the tip and the sample. By scanning the tip over the sample surface while keeping the tunneling current constant by means of a feedback loop, one can follow the surface contours with the tip. By monitoring the vertical position z of the tip as a function of the lateral position (x,y), a three-dimensional image $z(x,y)$ can be constructed. Motion of the tip in all three directions can be realized with sub-atomic accuracy by means of piezoelectric elements (Fig. 5).

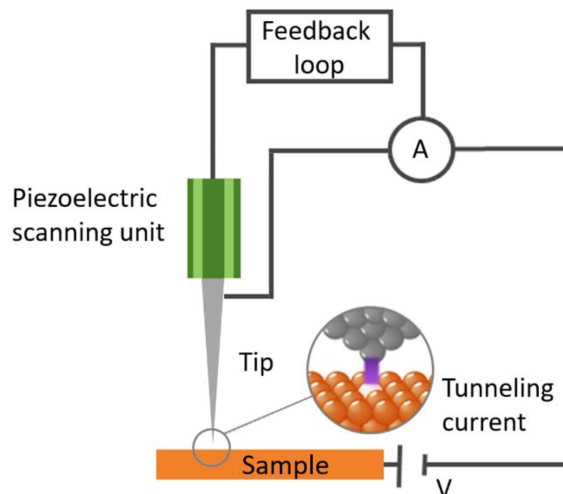

Figure 5: Schematics of the STM operation.

3.2.1.1 Tunneling current

To present the basic idea of the tunneling current, a simple one-dimensional (1D) model can be considered, where an electron with mass m and energy E, represented by its wavefunction $\psi(x)$, passes a potential barrier with a width d. The movement of the electron

in a rectangular potential given by $V(\mathrm{x})$ can be described by a time-independent Schrodinger equation [60]

$$\left[-\frac{\hbar^2}{2m}\nabla^2 + V(\mathrm{x})\right]\psi(\mathrm{x}) = E\psi(\mathrm{x}) \tag{3.1}$$

Inside the vacuum gap, the solution for the 1D Schrodinger equation is a decaying electron wave function

$$\psi(\mathrm{x}) \propto e^{-2d\kappa}, \kappa = \tfrac{\sqrt{2m(V-E)}}{\hbar} \tag{3.2}$$

In the limit of a strongly attenuating barrier ($\kappa d \gg 1$), the tunneling current is proportional to the probability for electrons tunneling through the vacuum barrier

$$I_x \propto T \propto |\psi(\mathrm{d})|^2 \propto e^{-2d\kappa} \tag{3.3}$$

From Equation 3.3 we can see that in the first approximation, the tunneling current is in an exponential relationship with the sample-tip distance. This exponential dependence is the origin of the high vertical resolution of STM in the sub-picometer range, meaning that even small changes in the sample-tip distance can have a significant effect on the tunneling current.

3.2.1.2 Bardeen formalism and the Tersoff-Hamann model

To explain the origin of the atomic resolution in STM, the basic theory of tunneling through a potential barrier needed to be extended to include the interactions between the lateral corrugation of the surface structure and the scanning tip. Following the Bardeen approach [63], Tersoff and Hamman used the time-dependent perturbation theory to calculate the tunneling current between two electrodes. According to Fermi's Golden Rule, the amplitude of electron transition rate can be determined by the overlap of the two wave functions of the two subsystems (tip and sample). This way the tunneling current can be given by:

$$I = \frac{2\pi e}{\hbar}\sum_{\mu\nu} f(E_\mu)[1 - f(E_\nu + eU)]\,|M_{\mu\nu}|^2\ \delta(E_\mu - E_\nu), \tag{3.4}$$

where $f(E)$ is the Fermi function, $M_{\mu\nu}$ is the tunneling matrix element, E_μ and E_ν are the unperturbed states in the absence of tunneling and U the sample bias voltage. The delta function restricts tunneling to occur only between electron levels with the same energy. The contribution of reverse tunneling has been neglected here. For small sample bias voltage and low temperature, the equation for the tunneling current can be written as

$$I \propto \int_{E_F}^{E_F+eU} |M_{\mu\nu}|^2 \rho_T(E - eU)\rho_S(E)\, dE, \tag{3.5}$$

where ρ_T is the density of states of the tip atom and ρ_S is the local density of states of the sample at the position of the STM tip, and E_F is the Fermi energy. The overlapping of the tip and surface wave functions ψ_μ and ψ_ν is described by the tunneling matrix element, while the square of the matrix element $|M_{\mu\nu}|^2$ represents the transmission matrix

$$|M_{\mu\nu}|^2 = -\frac{\hbar^2}{2m}\int d\vec{S}(\psi_\mu^*\nabla\psi_\nu - \psi_\nu\nabla\psi_\mu^*). \tag{3.6}$$

Determining the matrix element is quite challenging since the actual geometry and the chemical structure of the STM tip apex are generally unknown. Tersoff and Hamann

developed a model of vacuum tunneling for an atomically sharp tip where only the atom closest to the sample surface contributes to the tunneling current [64], [65]. They modelled the tip apex as a sphere of radius R (to resemble an s-type orbital at the tip apex), spaced from the surface by a distance h (Fig. 6).

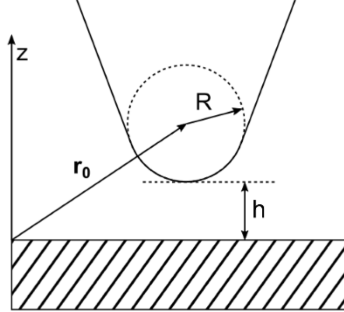

Figure 6: Tersoff-Hamman model of STM tip with an s-type orbital at the apex.

Assuming that the tip has a constant density of states within the given energy range and the Tersoff-Hamann approximation, the tunneling current can be fairly well approximated by:

$$I \propto \rho_T \int_{E_F}^{E_F+eU} \rho_S(E)\, dE. \tag{3.7}$$

Therefore, the constant current mode in STM represents the contour of constant surface local density of states.

3.2.1.3 Imaging semiconducting surfaces

It can be seen from Equation 3.7 that the STM image is a representation of the local electronic structure of the surface and not directly the atomic positions, which is especially important when it comes to the analysis of semiconductor surfaces. When imaging a semiconductor, the STM images differ depending on which side of the band gap the electrons contributing to the tunneling current come from. The occupied states of the sample, essentially the locations of high electron density, are imaged by tunneling from the occupied states of the sample to unoccupied states of the tip and vice versa, depending on the polarity of the applied bias voltage [66]. Since on normally doped semiconductor surfaces the Fermi energy is located within the bulk band gap, in the absence of metallic surface states, tunneling is only possible from the high-lying valance band states or into the low-lying conduction band states. When imaging semiconductor surfaces, sample bias voltages of the order of the band gap (~2 V) are usually used. Additionally, one has to have in mind that, due to the highly-oriented covalent bonds in semiconductors, the atomically resolved STM images can also differ depending on the tip-sample distance or equivalently, the tunneling current used in the constant current imaging mode.

There is one more thing to consider when it comes to imaging semiconducting surfaces. At LT, samples can become insulating. Below a certain temperature, the conductivity of semiconductors starts to decrease with decreasing temperature [67]. The LD Si substrates used in this work are non-conducting at 4.2 K and the microscope temperature needs to be increased to 60 K to achieve sufficient tunneling current for stable imaging. On the other hand, in the HD Si substrates with a dopant concentration of 1×10^{19} mbar, the number of charge carriers is high enough to enable electron tunneling in STM even at 4.2 K.

3.2.1.4 Calculated STM images

When it comes to forming atomic models of the surface structures, in most cases, the information acquired solely from STM results will not suffice. As mentioned in the previous subsection, the features observed in the STM images cannot be directly related to the atomic positions and the same is valid for the chemical composition of the observed structures. These drawbacks can be overcome by simulating various STM images. If calculated and experimentally observed STM images are the same, one can very reasonably assume that the proposed types of atoms and their positions represent true surface structures. To simulate STM images of a theoretical atomic-scale model, one first needs to perform a calculation based on density functional theory (DFT) [68]. The resulting output, i.e. the electronic density of states, is then used as the input information for the image calculation.

For the calculation of STM images, various software packages exist. In the HIVE program [69] used in this work, the constant-current STM images are generated based on the Tersoff-Hamann approximation presented in the previous subsection. This way a surface of constant current in an STM experiment can be identified with a surface of constant density of states in calculations. In the presented program, this is done by taking a point source and plotting a surface of constant density of states. It is important to stress that the resolution of the images calculated in such a manner is artificially increased.

3.2.1.5 Equipment and parameters in STM analysis and image calculations

A Joule-Thomson STM (SPECS) with a base pressure of 5×10^{-11} mbar was used for most of the STM measurements. The samples were cooled to 60 K to reduce thermal drifts while maintaining sufficient conductivity of the semiconductor surfaces. STM measurements were performed with an electrochemically etched W tip in the constant-current mode. Prior to STM imaging, the tip was conditioned on a Cu(111) surface by a controlled tip-sample interaction. The STM data were processed with the WSxM package [70].

The calculations were performed in collaboration with Dr. Wen-Yi Tong and Prof. Philippe Ghosez (Theoretical Materials Physics, Q-MAT, CESAM, University of Liège, B-4000-Liège, Belgium) based on DFT [71], [72] using the accurate full-potential projector augmented wave (PAW) method [73], as implemented in the Vienna ab initio Simulation Package (VASP) [74]. The exchange-correlation potential was treated in the PBEsol [75] form of the generalized gradient approximation with a kinetic energy cut-off of 600 eV. An $8\times8\times1$ and $12\times12\times1$ Monkhorst-Pack k-point mesh centred at Γ was adopted in the geometry optimization and self-consistent calculations, respectively. The convergence criterion for the electronic energy was 10^{-6} eV and the structures were relaxed until the Hellmann–Feynman forces on each atom were <10 meV/nm. The Sr/Si(001) surfaces were modelled using a slab geometry. The simulation substrates consist of five Si layers, similar to previous work [76]–[78]. A large 4×4 supercell with 16 Si atoms per atomic layer was adopted to do the relevant calculations of the interface. The dangling bonds of the Si atoms at the slab bottom were saturated with hydrogen atoms. To eliminate the spurious slab-slab interactions, a vacuum region of at least 1.5 nm was included between repeated slabs.

3.2.2 Atomic force microscopy

Atomic force microscopy (AFM) is a type of scanning probe microscopy used for the study of surface properties for both conductive and non-conductive samples on a nanometer and in some cases even atomic scale [79]. In AFM, a sharp tip attached to a cantilever is raster-scanned over a surface. The tip moves in response to tip–surface interactions, and this movement is measured by focusing a laser beam with a photodiode. An AFM is operated

in two basic modes: contact mode and tapping mode. In the contact mode, the AFM tip is in continuous contact with the surface. In contrast, in the tapping mode, the AFM cantilever is vibrated above the sample surface such that the tip is only in intermittent contact with the surface. This process helps to reduce shear forces associated with the tip movement. The tapping mode is the recommended mode that is commonly used for AFM imaging [80].

Ex situ AFM imaging was used for the investigation of surface topography of STO thin films. It was carried out on a Digital Instruments DimensionTM 3100 microscope, using Si probes with reflective Al coating (OTESPA-R3, Bruker). Tapping mode was employed in all of the measurements. Just like STM images, the AFM images were also processed using the WSxM software [70]. The root-mean-square (RMS) roughness value and relative error in analysis of STO thin films were obtained with three 5 mm × 5 mm images recorded in different areas of each sample.

3.2.3 Piezoresponse force microscopy

Piezoresponse force microscopy (PFM) is a version of AFM that allows the determination of local piezoelectric effect and manipulation of ferroelectric domains in piezoelectric/ferroelectric materials [81]. By bringing a sharp conducting probe in contact with a ferroelectric material and applying an alternating current bias between the probe tip and conductive substrate, a deformation of the sample can be achieved through the converse piezoelectric effect. The resulting deflection of the cantilever is detected by a standard split photodiode detector and then demodulated by use of a lock-in amplifier. This way, topography and local piezoelectric response and consequently the ferroelectric domains can be imaged simultaneously with high resolution.

PFM was used to investigate the ferroelectric properties of STO ultra-thin films on a Si substrate. The PFM images were recorded using a Molecular Force Probe 3D microscope (Asylum Research, CA, USA). The PFM images were recorded in PFM Vector mode. The scanning ac electric voltage of 15 V and frequency 425 kHz was applied between the doped Si substrate and a conductive Pt-coated Si tip (OMCL-AC240TM-R3, Olympus, Japan). A curvature radius of the tips was ~10 nm. The spring constant and the resonance frequency of the AFM tips were 2 N/m and 70 kHz, respectively.

3.3 Structure Determination by Diffraction

Diffraction techniques are the most important approach to the analysis of crystalline solids. By scattering X-rays or electrons at specific angles from sets of lattice planes in a sample, diffraction patterns are formed. These patterns can be used to determine long-range order properties, e.g., the symmetries, average unit cell dimensions, and orientations for individual crystalline phases present [82]. The intensities of the reflections in diffraction patterns are determined by the atomic positions within the lattice planes. Consequently, the diffraction patterns are the fingerprints of periodic atomic arrangements in a given material [83]. On the other hand, the deviations from the average, i.e., defects of some sort, show up as broadening of diffraction peaks, or, if they are periodic, as a splitting of peaks. Depending on the source and geometry used, bulk, thin film, or surfaces of different crystalline material can be analysed.

3.3.1 Grazing incidence X-ray diffraction

In X-ray diffraction (XRD), diffraction patterns are produced by constructive interference of an X-ray beam [84]. For the analysis of ultra-thin films (e.g., ~10 ML thick), the grazing

incidence XRD (GIXRD) technique with a synchrotron-light source is required in order to obtain sufficient signal and resolution. The advantage of this technique is that the X-ray probing depth can be greatly reduced by using a small incident angle, which has the effect of substantially improving surface sensitivity [85]. When coupled to a synchrotron radiation X-ray source (to produce an intense, parallel X-ray beam) ML sensitivity can be achieved. GIXRD can be therefore used to study surfaces, thin films and buried interfaces in a non-destructive way, yielding epitaxial relationship between the film and the substrate, and lattice parameters of ultra-thin films. [86].

GIXRD with a synchrotron-light source with a photon energy of 20 keV was used for crystallographic characterization of an STO thin film on Si (Sample $S_{CY,4}$). Reciprocal space mapping (RSM) of the asymmetric reflections was performed in order to determine the epitaxial relationship between STO films and the Si substrates. The analysis was performed at the beamline BM25-SpLine [87] of the European Synchrotron Radiation Facility (ESRF) using a six-circle diffractometer in vertical geometry, a photon energy of 20 keV and a beam spot size of 0.25 mm $\times$ 0.25 mm.

3.3.2 Electron diffraction

In low-energy electron diffraction (LEED) and RHEED, electrons are used to provide surface crystallographic information [82]. LEED uses normal incidence, with electron energies between 10 and 1000 eV, whereas RHEED (5-50 keV) uses grazing incidence and detection. In both cases, diffraction comes from two-dimensional rows of atoms.

In LEED, the diffraction pattern directly reveals the size and shape of the unit cell of the topmost, ordered material. It is possible to establish locations of atoms within the unit cell, give information on finite island sizes, strain, step densities, etc., however, these require complex analysis. LEED is routinely used to qualitatively check if the crystal surfaces are "well-ordered" and to determine the unit cell symmetries.

In practice, RHEED is used primarily to monitor *in situ* the nucleation and growth of epitaxial films. The grazing geometry leaves the surface open for the deposition process and enables acquiring RHEED information from the top few atomic layers, even though it is intrinsically less surface sensitive than the lower-energy LEED. In addition, it makes RHEED very sensitive to surface roughness effects such as island formation since the reflected beam is actually transmitted through island "asperities", giving rise to new diffraction features.

In this work, RHEED was used *in situ* and in real time to follow the Si(001) surface reconstructions during the deoxidation of the Si surface, during Sr deposition, and to assess the degree of crystallinity after the deposition of STO thin films and their crystallization. The electron gun of the RHEED system (Staib Instruments) was operated at an accelerating voltage of 30 kV. The diffraction patterns were monitored with a CCD camera and the recorded images were analysed with the KSA 400 commercial software (k-Space Associates).

LEED optics (SPECTRALEED, Scienta Omicron), situated in a preparation chamber of the STM system with a base pressure of 1×10^{-10} mbar, was used to inspect the stability of clean and Sr-passivated Si surfaces after their UHV transfer from the PLD to the STM system. About a half of the LEED screen appears darker because it is covered by a thin film that was accidently evaporated during a failed experiment unrelated to this work. The images of the LEED screen could be further processed by subtracting the background but were not altered as they are used solely for checking for potential changes in the surface reconstruction. The LEED patterns formed on the fluorescent screen were imaged by a digital camera.

3.4 X-Ray Reflectivity

X-ray reflectivity (XRR) is a surface-sensitive X-ray technique used to quantitatively determine the density, thickness and roughness of individual layers in a layer stack on a substrate [84]. The technique involves measuring the reflected X-ray intensity as a function of incidence angle over a range of angles close to the critical angle for total reflection. Above this critical angle, the specularly reflected intensity (where reflected angle is equal to incident angle) decreases, with a form that is dependent on the structural properties of the interface. A typical reflectivity curve is essentially a combination of the Fresnel reflectivity and an interference pattern (Kiessig fringes) from the scattering at different layers, e.g., in a thin film or a multilayer structure.

XRR is not a diffraction technique, but belongs to the larger group of scattering methods, however, the diffractometers used in XRD with their goniometer stages may equally be used for this type of measurements. As XRR does not depend on diffraction, it can be used on amorphous or crystalline matter.

The thicknesses and densities of the STO layers (S_{REC}, S_{OX}, S_{PR}, and S_{TR}) were measured *ex situ* by XRR, using an Empyrean diffractometer with PIXCel3D detector, (PanAnalytical, Netherlands). On the incident side, a 1/16° aperture was used, along with a fixed incident beam mask of 2 mm. On the diffracted side, a parallel-plate collimator with an acceptance angle of 0.27° and a PIXCel3D detector in the receiving-slit mode (all channels active) were used. The XRR spectra were acquired in the ω-2θ mode in the range from 0.1 to 5°, with a 0.005° step size and 11 s per step. The simulation of obtained curves was performed using the X'Pert Reflectivity software and a segmented fit procedure. The error in the parameters was obtained with the Error Analysis tool implemented in the software [88].

Sample $S_{CY,4}$ was analysed by XRR at the beamline BM25-SpLine [87] at the ESRF using the same diffractometer as for the GIXRD measurements. The synchrotron-based XRR data was fitted using the XRR refinement program GenX [89]. A layer model was first formed in the software. Based on this model, a reflectivity curve was simulated. The simulated curve was then fitted either by manually changing the parameters or running an automated fitting function until the figure of merit (e.g. the function that compares how well the simulation matches the measured data) was minimal while keeping the values of the parameters in the range of realistic physical values.

3.5 X-Ray Photoelectron Spectroscopy

XPS is a surface-sensitive spectroscopic technique that can provide qualitative and quantitative information on the elements present on the surface and in thin films of different materials together with the oxidation states of the detected elements. Surface analysis by XPS is accomplished by irradiating a sample with monoenergetic soft X-rays and analysing the energy of detected electrons. X-rays emitted from common laboratory sources (Mg Kα or Al Kα) have limited penetration power in a solid on the order of 1-10 μm. They interact with atoms in the surface region, causing electrons to be emitted by the photoelectric effect [90].

The chemical composition of Sr-passivated Si surface, the STO-Si interface, and the STO thin films was determined *ex situ* using a monochromatic XPS system (Physical Electronics, Inc., USA, E = 1486.6 eV) with a hemispherical analyser (resolution: 0.3 eV) and a multichannel detection system. The survey spectra were taken in the range of binding energies from 0 to 1200 eV with pass energy of 187.85 eV. The high-resolution spectra were taken at take-off angles of 20, 45 and 70° (the take-off angle is defined here as the angle of

the X-ray source with respect to the sample surface normal). The charge correction for samples exposed to atmosphere was made with respect to the adventitious C 1s component at 284.8 eV, while for samples transferred in UHV, the charge correction was made with respect to the Si 2p peak at 99.0 eV based on measurements of the Si substrates with the native oxide. For the purpose of qualitative and quantitative analysis of XPS spectra, the software programs MultiPak and XPS Peak were used. Relative sensitivity factors (0.368 for Si 2p, 1.992 for Sr 3d, 2.077 for Ti 2p, 0.733 for O 1s and 0.314 for C 1s) provided by instrument manufacturer were applied to calculate surface concentrations.

Chapter 4

The Si(001) Surface

4.1 Introduction

All Si crystals handled in air are covered with a thin amorphous SiO_2 layer. To create favourable conditions for epitaxial growth of STO, first the native oxide needs to be removed. Only a clean surface with a high degree of crystallinity can promote epitaxy. One of the most effective procedures for the removal of the native SiO_2 layer is thermal deoxidation [59], [91]. This procedure consists of two main steps. First, the substrate is degassed by prolonged annealing at a moderate temperature to remove the adsorbed carbohydrates and water, followed by short periods of heating the substrate to a temperature close to its surface melting temperature, also known as flashing. This way not only the native oxide is removed but also the majority of the metal impurities buried in the oxide layer. By flashing to ~1180 °C even the problematic SiC, known to cause roughening, can be removed from the surface [92]. However, a clean Si surface is extremely reactive. To avoid re-oxidation or contamination prior to the Sr-passivation step and STO growth, the surface must be isolated from oxygen and other reactive species, which can be achieved by performing the deoxidation process under UHV conditions.

To produce a defect-free Si surface, a Si substrate should be prepared in a UHV system with a base pressure in the 10^{-11} mbar range [59]. The substrate should be degassed until the pressure stays in the 10^{-10} mbar range, while the thermal deoxidation step should be performed without exceeding 1×10^{-9} mbar to avoid roughening of the Si surface. On the other hand, PLD systems typically operate in the HV regime with base pressures in the range from 10^{-8} mbar to 10^{-6} mbar.

Klement et al. used RHEED to study the thermal deoxidation of Si(001) in a PLD system with a base pressure much lower compared to typical PLD systems (~1×10^{-8} mbar) [93]. They found that despite the higher pressure, a clear 2×1 reconstruction indicating a clean Si surface can be observed after several flashes. However, after 15 min of exposing the surface to 1×10^{-8} mbar of residual atmosphere, additional spots appeared in the RHEED pattern due to C contamination. They pointed out that, although such contamination is unavoidable, it could be delayed by improving the vacuum conditions and passivating the surface promptly after the deoxidation step.

By solving some technical issues, we were able to decrease the base pressure in our PLD chamber but only to a certain point. The base pressure in the growth chamber after performing a bake-out is 2×10^{-9} mbar, while the pressure increases to 8×10^{-8} mbar after the degassing step and can exceed 5×10^{-8} mbar during the deoxidation step.

Since such vacuum conditions are still far from optimal, the first step of this work was to determine the morphology and level of surface contamination of Si surfaces exposed to a low level of residual atmosphere in order to assess the quality of the Si surface before the

Sr-passivation step and STO overgrowth in the production of STO-Si pseudo-substrates by PLD.

In the first part of this chapter, the Si(001) surface is introduced by a description of its ground state atomic structure, surface reconstructions, and the properties of vicinal Si(001) surfaces. This is followed by a presentation of results of surface morphology analysis of two types of deoxidised Si substrates with different dopant concentrations. Additionally, an atomic-scale study of a Si(001) surface exposed to a low level of the residual atmosphere is given. The chapter concludes with a discussion about problems with metal contamination.

4.1.1 The ideal Si(001) surface

In a bulk Si crystal, each atom forms four covalent bonds with the neighbouring atoms, resulting in a diamond crystal structure with a bulk lattice constant a_{Si}=0.543 nm. Cutting the crystal in certain directions leads to exposure of different types of surfaces. Surfaces cut in the (001), (113), (111), and (110) directions have the lowest surface energy and are therefore called primary surfaces (Fig. 7).

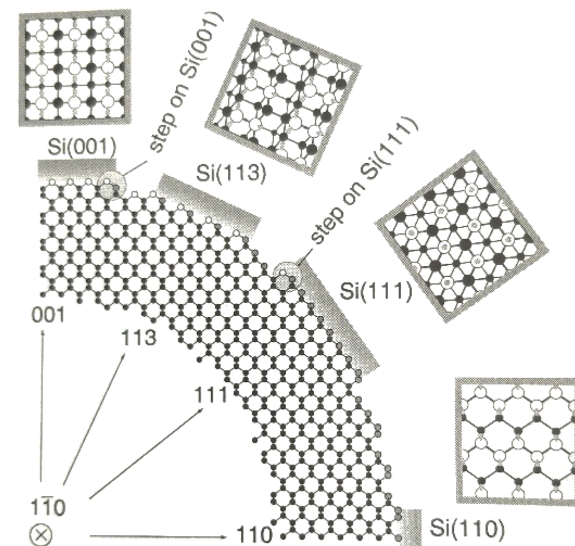

Figure 7: (a) Representation of different primary Si surfaces. Figure from [94].

Out of all primary surfaces, the Si(001) surface is at the same time the simplest and the most technologically relevant Si surface [94]. By cutting the crystal in the (001) direction, two bonds per surface atom are broken. As shown in Fig. 8(a), the (1×1) surface unit cell is rotated 45° relative to the bulk unit cell, and has a lattice constant of $a_S = a_{Si}/\sqrt{2}$, where a_{Si}. The energy needed to break one bond is E_b= ~2.3 eV, which gives a surface energy per area γ = 15 eV/nm^2 [94]. This breaking of bonds leads to a high degree of instability. To minimize the total free energy of the system, the surface atoms need to readjust, which leads to surface reconstructions.

The main building block which determines the properties of the Si(001) surface is a Si dimer. To reduce the surface energy, the top-most atoms move pairwise towards each other and form new bonds (Fig. 8(b)). By forming dimers, one of the two dangling bonds per surface atom is filled. The dimers lie in rows perpendicular to the dimer axes and oriented along either [$\bar{1}$10] or [110] directions, according to the bulk Si crystal. The two directions correspond to the two face-centered-cubic (fcc) sublattices that form the diamond lattice.

To further decrease the surface energy, the dimers shift from a symmetric position to a position where one atom is slightly elevated relative to the other. The dimers are said to

buckle. Along a row, the buckling direction must alternate to minimize variations in the bond length. This alternation leads to higher-order p(2×2) and c(4×2) reconstructions. Formation of the dimers is accompanied by considerable subsurface strain extending many atomic layers into the crystal [95].

It took researchers over 40 years of intense studies to clarify which of these reconstructions is the ground state atomic structure of the Si(001) surface [96]. In this context, STM has played an important role. At first, this Si surface was thought to reconstruct into the 2×1 structure composed of symmetric dimers. However, at room temperature (RT), the dimers only appeared to be symmetric because they dynamically flip between two possible buckled configurations at a rate too fast for the STM tip to follow. STM images only show the average of these two configurations, giving rise to the appearance of symmetric dimers. The c(4×2) structure was widely accepted as the ground state already in the 1990s. However, this view was challenged again at the beginning of the 2000s by STM observations of a 2×1 structure below 20 K [97]. On the contrary, when the ground state was studied by noncontact AFM at 5 K, the Si(001) surface exhibited the c(4×2) structure [98]. It was found that in the case of STM analysis, the tunneling current from the STM tip can excite the flipping of the dimers leading to the appearance of the 2×1 symmetry, while the interaction with the AFM tip is negligible. Today, it is established that the ground state structure of a clean Si(001) surface is the c(4×2) arrangement, constructed by buckled dimers. It should be stressed that the STM and LEED analysis of the clean Si(001) surfaces presented in this work was performed at RT, therefore the observed surface reconstruction was 2×1, as expected.

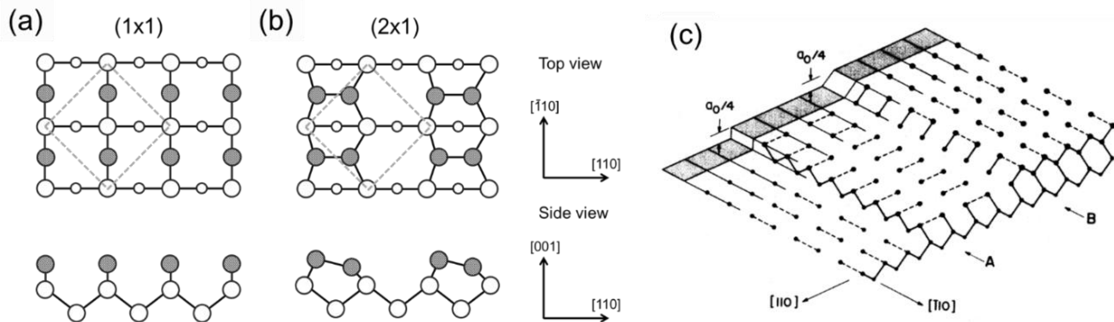

Figure 8: Schematic diagrams of the Si(001) surface (1×1) unreconstructed (a) and (2×1) reconstructed (b). The darker circles represent the top layer in which the atoms are paired to form dimers. The dashed line shows the projection of the bulk unit cell onto the surface. (c) Schematic diagram of a vicinal Si(001) surface tilted about [110]. The three terraces shown are separated by two monoatomic steps, one type A and the other type B, running from the upper left to the lower right. Note that the dimers, represented by dashed lines, alternate their directions between terraces. The bulk lattice constant is a_0. Figure from [99].

4.1.2 Surface defects: steps and terraces

Completely flat surfaces do not exist in real crystals. By cutting a crystal to produce a surface in the vicinity of the (001) plane, steps and terraces are created. Such surfaces are called vicinal, and the angle of the tilt with respect to the (001) plane is called a miscut angle, which is usually no more than a few degrees.

Clean Si(001) vicinal surfaces exhibit steps and reconstructed terraces. The average step spacing (terrace width) is given by $h/tan\alpha$, where h is the step height and α is the miscut angle. If the intersection of the vicinal cut with the well-oriented face is, for instance,

along [$\bar{1}$10] then the surface is said to be tilted toward the [$\bar{1}$10] zone [100]. The single-step height, *h*, is one atomic layer, which on the diamond lattice is $a_0/4$ (0.136 nm). Across a single step the direction of the dimer rows rotates by 90° because the two terraces belong to different sublattices. For a tilt in the [$\bar{1}$10] or [110] zone, we divide the steps into two classes, type A and type B, depending on the orientation of the step relative to the dimer rows on the upper terrace. On the terrace above the type A step, which is known as A terrace, the rows run parallel to the step edge (Figure 12(c)). Above the type B step, the B terrace has rows running perpendicular to the edge.

Due to additional polishing, the miscut and the tilt zones can be effectively different in substrates cut from the same wafer. As the direction of the tilt deviates from the [$\bar{1}$10] or [110] zone, the step edges become a mix of type A and type B segments separated by kinks. In the extreme case of steps running along [100], there is a kink at every dimer row so the lengths of the segments are reduced to $2a_S$.

Steps of the Si(001) surface can be either one or two atomic layers high [94]. For small miscut angles, less than 1-2°, the steps are monoatomic with a height of 0.136 nm. If the polar miscut angle exceeds 6-8°, steps are exclusively biatomic, while a combination of the two appears in between these two limits. In the case of double steps, the surface is said to be primitive or single-domain because the double steps allow only one of the two fcc sub-lattices to appear at the surface [91].

4.2 Surface Morphology of LD and HD Si Substrates

We analysed the surface morphology of two types of Si substrates with different dopant concentrations: lightly and heavily doped Si substrates that were later used in the preparation of Sr-passivated Si surfaces and in the growth of STO thin films by PLD. Both types of substrates were p-type and doped with boron (B). In most studies regarding the formation of STO-Si pseudo-substrates lightly doped (LD) Si substrates with a dopant concentration of ~1×10^{16} at/cm^3 are used, while heavily doped (HD) Si substrates with a dopant concentration of ~1×10^{19} at/cm^3 might represent a better choice when it comes to special applications, e.g. photo-electrochemical water splitting, where higher dopant concentrations are needed to achieve sufficient charge transfer. Since the samples need to be electrically conductive at 4.2 K, HD Si substrates are also needed in LT STM imaging.

4.2.1 Methods

HD and LD Si substrates were first cleaned by sonification in acetone (10 min), rinsed in ethanol and dried with N_2 gas. The substrates were mounted on a Ta holder with Mo clips. Any contact between stainless steel tools and Si substrates was avoided. Mounted substrates were inserted into the PLD system with a base pressure of 2×10^{-9} mbar where they were degassed for 12 h at 650 °C. After degassing, the native oxide was removed by flashing: the temperature was momentarily increased from 650 °C to 1200 °C, kept at this high temperature for 60 s, quickly cooled to 950 °C and then decreased with the rate of 100 °C min^{-1} until reaching 650 °C. The flashing was repeated once or twice more to reduce the maximum pressure during the flash occurring due to degassing of the sample holder. The maximum pressure during the final flash was ~1×10^{-7} mbar. During cooling, the pressure decreased and settled at 8×10^{-9} mbar. The deoxidation procedure was monitored *in situ* by RHEED. After RHEED analysis in the PLD chamber, the samples were transferred to a separate UHV system using a vacuum suitcase where they were analysed by LEED and STM.

4.2.2 Results and discussion

Fig. 9(a) shows a RHEED pattern of a LD Si substrate with the native oxide. The diffuse background indicates that the amorphous SiO_2 layer is still present after the degassing step. After flashing to 1200 °C, sharp streaks and spots appear in the RHEED pattern, indicating the removal of the oxide layer and the formation of the (2×1)+(1×2) reconstruction of the exposed crystal surface (Fig. 9(b)). Well pronounced first-order streaks in the zeroth Laue zone and spots in the ½ Laue zone can be observed, while no additional spots characteristic for carbon contamination appear. The RHEED pattern is a superposition of two reciprocal lattices corresponding to the (2×1) and (1×2) domains. The relation between the reciprocal lattice of the Si(001)(2×1)+(1×2) surface and its corresponding RHEED pattern is presented in Fig. 9(d).

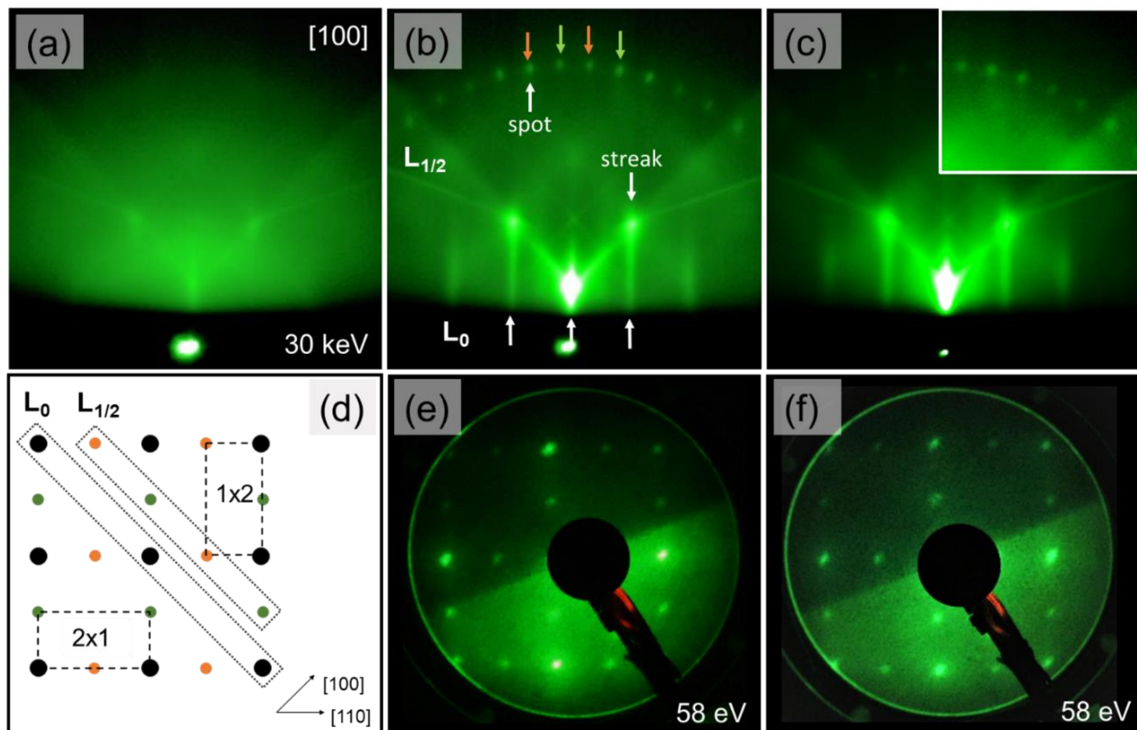

Figure 9: (a) RHEED pattern of an amorphous SiO_2 layer on a Si(001) surface, before deoxidation. (b) RHEED pattern of the Si(001) surface of a LD Si substrate, after deoxidation. (c) RHEED pattern of the Si(001) surface of a HD Si substrate, after deoxidation. The inset shows a part of the image with enhanced brightness. All RHEED patterns were taken in the [100] azimuth. (d) Schematics showing the reciprocal lattice of a double domain (2×1) (green) and (1×2) (orange) structure. The diffraction spots of the zeroth and 1/2 Laue zones in the RHEED patterns shown in (b) and (c) are marked. (e) and (f) LEED patterns of deoxidized LD Si and HD Si surfaces, respectively.

After the RHEED analysis, the samples were transferred to a separate UHV system using the vacuum suitcase. The two, LD and HD Si samples were transferred separately. LEED analysis (Fig. 9(e) and (f)) showed that the double domain 2×1 reconstruction was preserved in both cases. This indicates that the sample transfer was successful.

Large area STM images of the LD Si surface presented in Fig. 10(a) and (c) show a high level of contamination, however, terraces and steps can be easily distinguished. The average step spacing is ~45 nm. It is possible to estimate the direction of the dimer rows according to the shape of step edges. A and B terraces can be distinguished. Because the

dimer rows seem to run along and perpendicular to the step edges, it seems that the surface is tilted toward the [$\bar{1}10$] or [110] zone. Due to surface contamination, high-resolution STM imaging was not successful (Fig. 10(e)).

It is interesting that, even though clear electron diffraction patterns were observed, no dimer structures or any other periodic structures were identified by STM. The conflicting results arise from the difference in the sampling depths of the e.g. LEED and STM techniques. While STM typically images only the topmost atomic layer, LEED sampling depth can be 5-10 ML [100]. It appears that the periodic dimer structure is present on the Si surface but buried under a layer of contamination. We tried to remove the surface adsorbates by performing additional annealing of the sample in the preparation chamber of the STM system (10 min, ~300 °C, p=5×10^{-10} mbar), however, no substantial improvement of the surface quality was achieved.

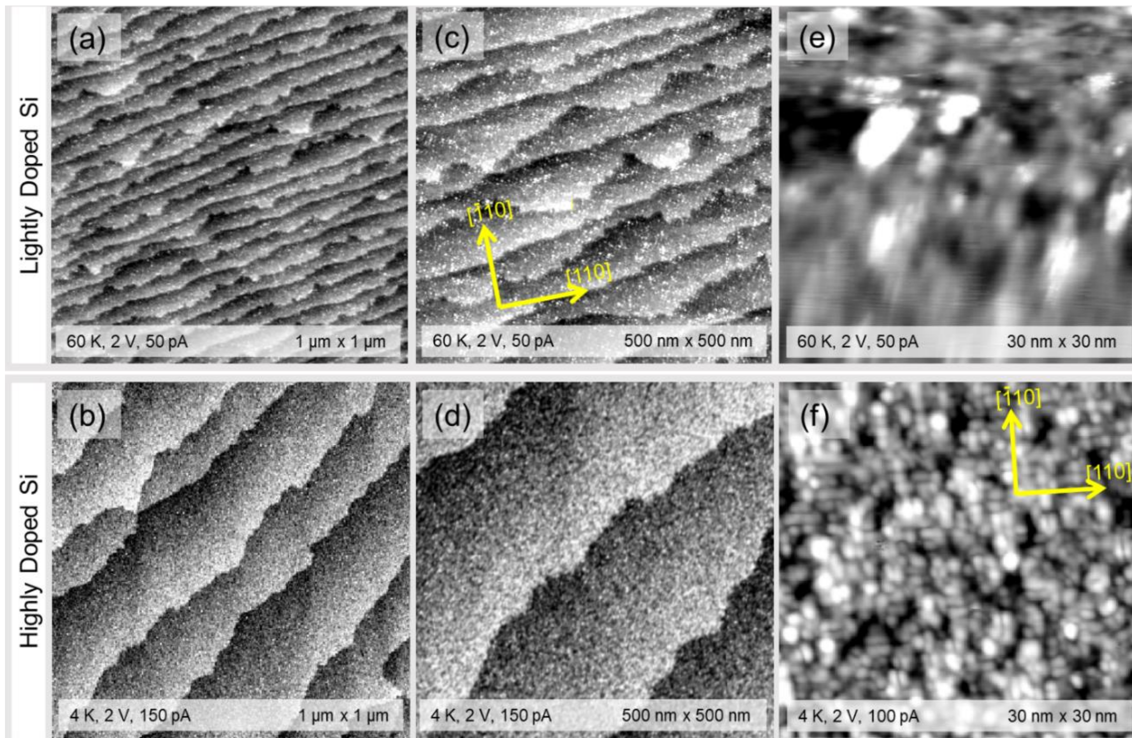

Figure 10: (a) and (b) Large area STM images of LD and HD Si(001) surface, respectively. (c) and (d) Comparison of step spacing of LD and HD Si substrates, respectively. (e) and (f) High resolution STM images of LD and HD Si, respectively.

Large area STM images of the HD Si substrate show an evenly stepped surface, as seen in Fig. 10(b) and (d). The shapes of neighbouring step edges exhibit similar features and it is difficult to determine the orientations of the dimer rows. It seems that the step edges are a mix of type A and type B segments separated by kinks and that the direction of the tilt is in the [100] zone. The step spacing ranges from 120 to 280 nm, with an average step spacing of ~200 nm. In the high-resolution STM image shown in Fig. 10(f), elongated features oriented in two preferential directions can be observed. However, the surface contamination is too high to see a clear (2×1) dimer structure.

It is interesting that the average step spacing of the HD Si substrates presented in this chapter is ~5× larger compared to the terrace sizes of LD Si substrates (~ 40 nm), even though both types of Si substrates were bought from the same provider under the same specifications (a miscut angle in the range of -0.1° to +0.1°). However, after calculating the

step spacing for different miscut angles in the rage from 0 to 0.1°, one realizes that the difference in the step density can be quite high, as presented in Table 3. In the future, it might be interesting to see how the substrate step density influences the epitaxy of thin films.

Table 3: Step densities of Si(001) surfaces with monoatomic steps for different miscut angles.

Miscut angle [°]	Step spacing [nm]	Step density [/µm]
0.1	1.4	717
0.01	14	71
0.0035	40	25
0.001	140	7
0.0007	200	5

4.3 Atomic Structure of Si(001)

The main goal of the work presented in this section was to determine the quality of the deoxidised Si surface prior to the Sr-passivation step. We needed to check if the deoxidation procedure was successful and if the Si surface remains clean prior to the deposition of Sr. During the time between the deoxidation and Sr-passivation steps (~ 5 min), the Si surface is exposed to a pressure of residual atmosphere in the 8×10^{-9} -1×10^{-8} mbar range, which equals a surface exposure of ~2 L. On the other hand, 10-15 min are needed to transfer the samples from the PLD system to the vacuum suitcase, yielding a 2-3× higher surface exposure compared to the exposure between the deoxidation and Sr-passivation steps. Because it was not possible to decrease the surface exposure in the PLD system at JSI, we had to use a more advanced vacuum system with *in situ* sample transfer possibilities to simulate the exposure of the Si surface to ~2 L of background gas and perform surface analysis without additional surface contamination during sample transfer.

The samples were prepared and studied in a special UHV system at the Institute of Applied Physics, Vienna University of Technology (TU Wien), Austria. This UHV system interconnects several vacuum chambers with PLD, XPS, LEED, and RT STM equipment enabling fast *in situ* transfer between the chambers. Furthermore, a base pressure of 5×10^{-10} mbar can be reached in the TU Wien PLD chamber, which is much lower compared to the base pressure in the JSI PLD system. The comparison of base pressure of the TU Wien and JSI PLD systems at different stages of the sample preparation is presented in Table 4. With a lower base pressure, together with a faster transfer procedure, the surface exposure was decreased to the point resembling the exposure of the Si surface between the deoxidation and passivation steps in the JSI PLD system.

Table 4: Comparison of base pressures in the TU Wien and JSI PLD systems at different stages of the thermal deoxidation procedure.

	p after BO	p after degassing	p max at last flash	transfer time*
JSI	2×10^{-9} mbar	7×10^{-9} mbar	1.6×10^{-8} mbar	~ 10-15 min
TU Wien	5×10^{-10} mbar	2×10^{-9} mbar	1.3×10^{-8} mbar	~ 5 min
*from the PLD chamber to a chamber with $p<1\times5^{-10}$ mbar				

4.3.1 Methods

LD Si substrates were attached to a Mo plate with a slightly recessed pocket and a 4 mm × 4 mm hole by spot welded Mo strips (Fig. 11(a)). Prior to mounting, the plate was cleaned by dipping in nitric acid (20%) for 60 s and sonicated in ultra-pure water (3 × 15 min) in a fresh beaker. The Mo oxide was removed using a SiC grinding paper. Mo strips were cut from foil and sonicated in acetone (10 min) and isopropanol (10 min) in a fresh beaker. Si substrates were sonicated in acetone (15 min) and isopropanol (10 min) and dried with CO_2 gas. No stainless steel tools were used during handling and mounting of the Si crystals.

Experiments were performed in a PLD system from TSST. The system allows for rapid *in situ* transfer of as-deposited samples from the deposition chamber to a surface analysis system combining an STM (SPECS Aarhus 150), XPS (non-monochromatic Mg or Al Kα source, SPECS Phoibos 100), and LEED (Omicron SpectaLEED) [101].

The sample plate with a "dummy" Si substrate was first degassed by annealing and flashing in UHV. Then, a fresh Si substrate was mounted, inserted into the PLD chamber, and degassed at 650 °C for 12 h using IR laser heating. The spot size of the IR laser spot on the sample plate was about 1 cm in diameter (Fig. 11(b)). The native oxide was removed by flashing to 1200 °C. After 3 flashes, the sample was transferred from the PLD chamber via a transfer chamber to the analysis chambers without breaking vacuum. The STM experiments were performed at RT, using electrochemically etched W tips. LEED was performed in the same analysis chamber with a base pressure below 6×10^{-11} mbar.

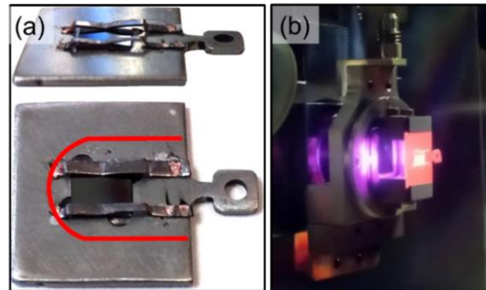

Figure 11: (a) Mo sample plate with Si substrate mounted by spot-welding Mo strips. The red U marks the area of the plate that has a limited height in order to fit into the STM. (b) Image taken during a flash at 1200 °C. Not only the sample but also the plate is heated because the spot size of the IR laser on the plate is 1 cm in diameter, which is larger than in the case of IR laser heating in the PLD system at JSI.

4.3.2 Results and discussion

LEED analysis showed a (2×1)+(1×2) surface reconstruction (Fig. 1(a2)), an indication of a clean Si(001) surface. STM analysis performed at RT revealed a smooth surface with evenly distributed steps and terraces as shown in Fig. 12(b) and (c). The average step spacing is ~20 nm, and the step edges are a mix of type A and type B segments separated by kinks with the tilt direction close to the [100] zone. In Fig. 12(c), a cluster of contamination can be observed. The source of such local contamination is usually the STM tip.

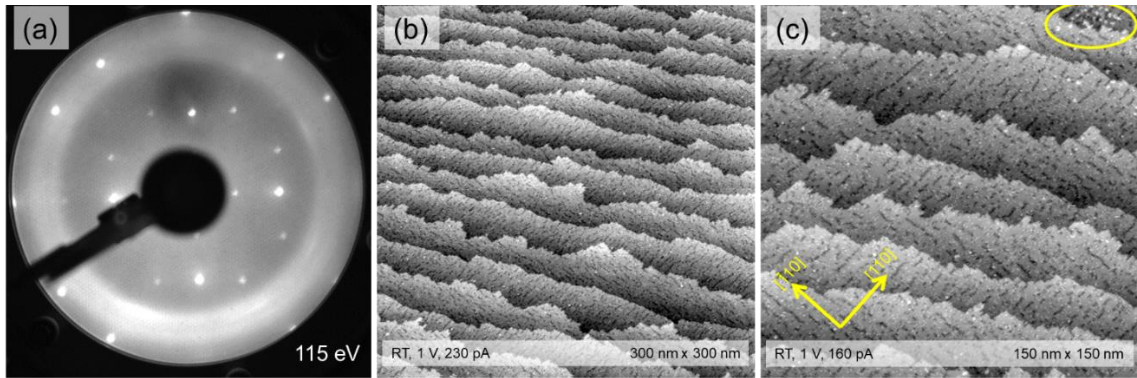

Figure 12: (a) LEED pattern of a (2×1)+(1×2) surface reconstruction. (b) Large-area STM image. (c) STM image of steps and terraces. Contamination from the tip approach is marked.

Fig. 13(a) and (b) show high-resolution STM images of the empty states. Rows of dimers can be well distinguished. When determining the exact positions of the dimers relative to the rows one has to be careful because the interpretation of STM images of semiconductors is not straightforward. STM does not observe the positions of atoms but the distribution of electron density of states. In the case of empty states images, the bright features represent areas that can be filled with electrons. When it comes to the Si(001) surface, these are the dangling bonds. However, STM images of the dangling bonds can also differ depending on the tip-sample distance, which is related to the tunneling current [100]. In the presented case, the STM tip scans the empty states from a large distance (low current) and the bright rows are centred between the dimer rows. Here, the dimer vacancy defects can be used as reference points.

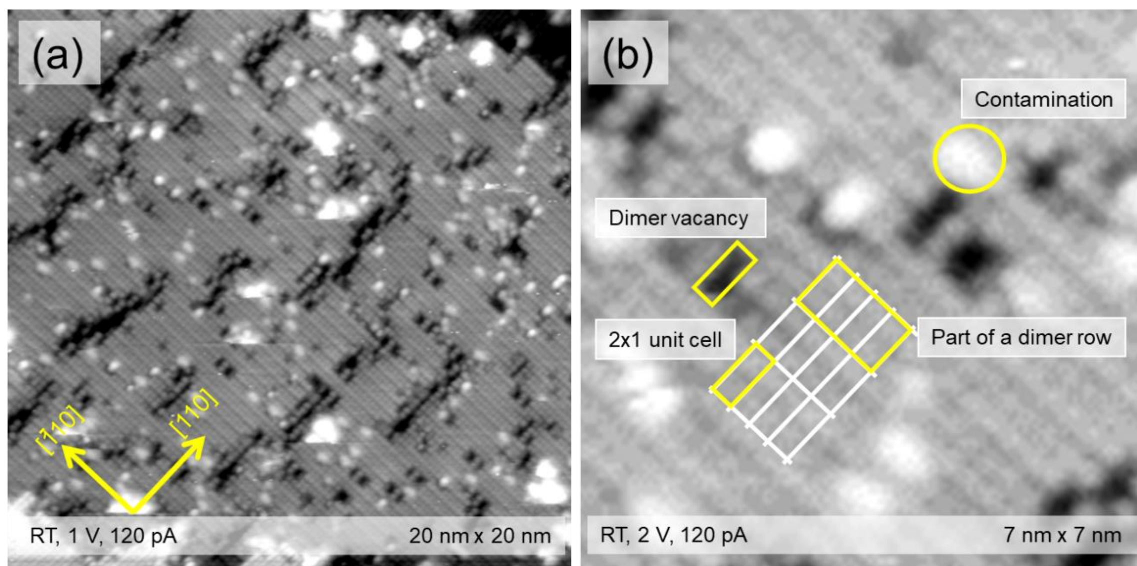

Figure 13: (a) High-resolution empty states STM image. (b) Close up where the main features of the Si(001) surface are marked.

Two types of surface defects can be observed. The bright protrusions unevenly distributed across the surface can be attributed to impurities adsorbed from the residual atmosphere, which is in accordance with traces of C and O detected by XPS. These impurities are weakly bonded and can be easily displaced by the STM tip. The other type

of defects are dimer vacancies. Single and double dimer vacancies can be observed, while the majority of dimer vacancies are arranged in lines perpendicular to the dimer rows. Single and double vacancies are intrinsic defects of the Si surface [94], but their aligning into rows is specific to metal contamination.

The XPS survey showed presence of Si, C, O and Ni (Fig. 14(a)). The high-resolution XPS spectrum from the Si 2p region exhibits a single peak at ~99 eV, with no extra peaks detected at higher binding energies. This indicates that the native SiO_2 was completely removed from the Si surface and no additional silicates were formed (Fig. 14(b)). C and O species were adsorbed from the residual atmosphere. It seems that a 5-min surface exposure to ~1×10^{-8} mbar residual atmosphere is low enough to prepare a well ordered Si surface with only minor traces of non-metal contamination.

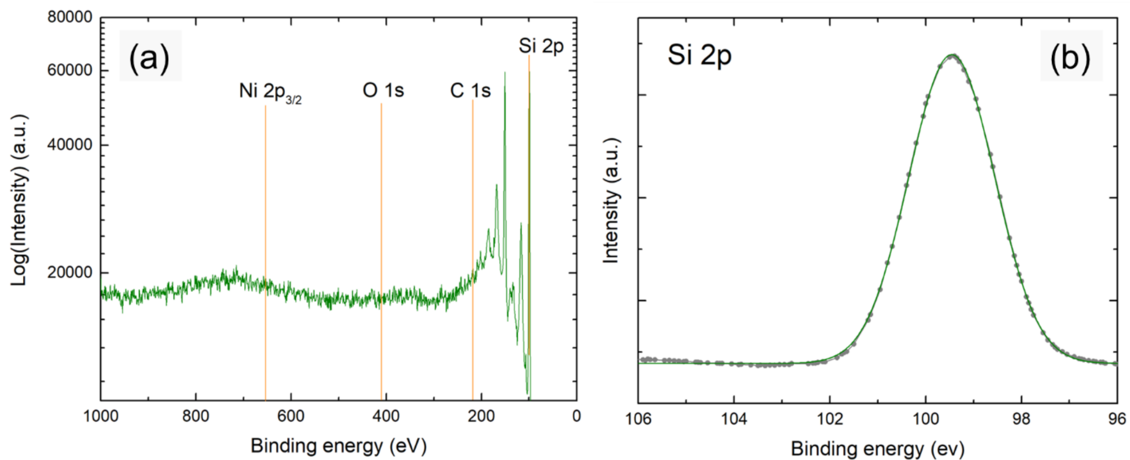

Figure 14: (a) XPS survey of the deoxidised Si substrate. (b) High-resolution XPS spectrum in the Si 2p region.

4.3.2.1 Ni contamination

The presence of Ni was not expected, however, it explains the high density of dimer vacancies observed in STM images. After finding the Ni contamination, we attempted to remove the metal atoms from the Si surface, by performing additional flashes at 1200 °C. After 8 flashes in total, the 2×1 LEED pattern remained unchanged (Fig. 15(b)). After 3 additional flashes, a $(2\times n)$ + $(n\times2)$ surface reconstruction appeared (Fig. 15(c)).

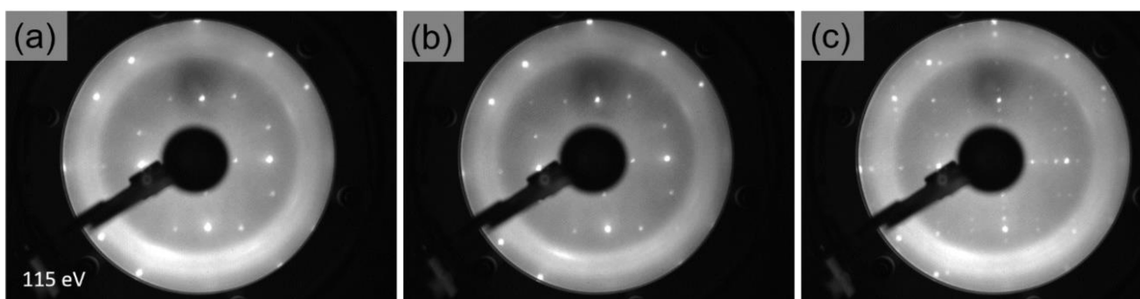

Figure 15: (a) A clear (1×2)+(2×1) surface reconstruction after 3 flashes. (b) The surface reconstruction is preserved even after 5 additional flashes (8 flashes total). (c) LEED pattern after a total of 11 flashes exhibiting the $(2\times n)$ + $(n\times2)$ surface reconstruction.

XPS analysis of the Si surface was performed after 3 and after 11 flashes in total. The XPS spectra from the C 1s, O 1s and Ni $2p_{3/2}$ regions are presented in Fig. 16. It can be seen that Ni concentration was actually increased by subsequent flashing. At the same time, the concentration of O was decreased, while C concentration remained about the same. In order to identify the source of Ni, additional XPS scans were performed on the Mo sample plate and clips, yet no Ni was detected there.

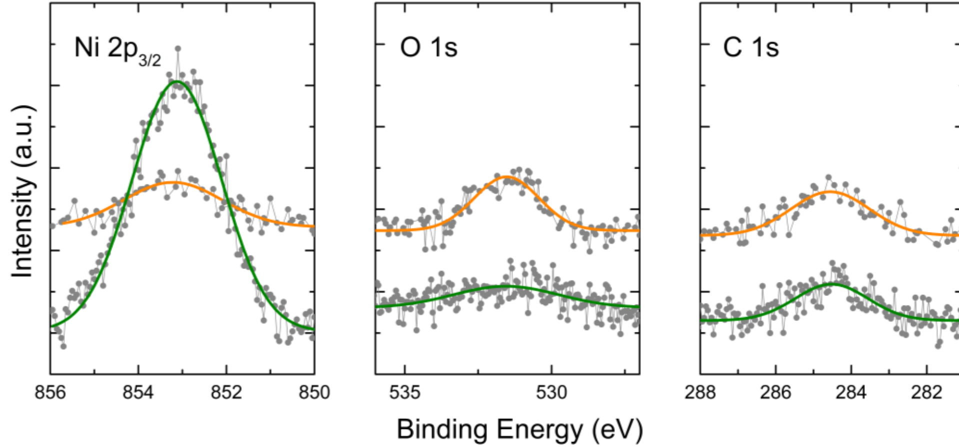

Figure 16: XPS spectra of the deoxidized Si(001) surface after performing 3 (orange) and 11 (green) flashes.

In principle, the Si(001) $2\times n$, ($5 < n < 13$), surface reconstruction represents one of the metastable reconstructions of the nominally clean Si(001), however, it most often indicates contamination, particularly with Ni, but also with Cu or Ag. Niehus et al. discovered that the dimer vacancy arrays with a long-range order resulting in a Si(001)(2×8) phase can be stabilized by as little as 1% of Ni surface concentration [102]. Contamination atoms are not a basic ingredient of the $2\times n$ structure. Nonetheless, Ni contamination stabilizes the dimer vacancies and promotes the $2\times n$ reconstruction on the Si(001) surface. In a very recent study, Kuzmin et al. found that a dimer vacancy line structure includes one Ni atom per defect [103]. They suggested that, according to the chainlike dimer vacancy structure with the ($2\times n$) periodicity, the Ni atoms are arranged in regular atomic rows with a spacing of $2a_s$ along a row and an inter-row separation of $n\times a_s$, although, the binding site of the impurity atom is still unknown in detail.

Ni contamination can come from stainless steel tools, from sample holders during high-temperature annealing or it can also be back-sputtered from walls of the UHV chamber. It is said that Ni contaminates Si so easily that touching the sample with a stainless steel tool can bring enough impurities to invoke a $2\times n$ superstructure on the Si(001) surface [104]. This metal impurity is more troublesome than other constituents of steel (Fe, Cr) because Fe and Cr form silicides that vaporize during annealing while Ni remains on the surface even above 1200 °C. In the presented study, only plastic and Teflon tools were used when handling the substrates, and pure Mo was used for the holder parts. Thus we suspect that the source of Ni were the spots where Mo clips were welded to the sample plate. Because the welding spot was clearly visible, some material from the welding tools must have been transferred to the sample plate.

According to the literature, it is possible to remove Ni contamination by prolonged annealing. Such methods were described by Ukraintsev and Yates [58]. They were able to restore the Si(001) surface to its condition before contamination by multiple annealings at 1200 °C with a total annealing time exceeding 3h. In their study, cooling with a stop at

730-870 °C for 2 min, followed by slow ~2 °C/s cooling, was used to produce a Si(001) surface with minimal surface defects. They also observed that fast quenching from 1200 °C to RT leads to a higher Ni surface concentration and elevated density of surface defects. In their case, the source of Ni was a Ta sample holder. By etching the holder in concentrated and boiling hydrochloric acid, together with the described annealing procedure, they managed to decrease the contamination below the sensitivity of Auger Electron Spectroscopy. Since removing Ni from Si is beyond the scope of this work, we did not continue with similar experiments.

4.4 Conclusions

We investigated the surface properties of two types of commercial Si substrates with different dopant concentrations. In both cases, a thermal deoxidation procedure was used for the preparation of a clean Si surface, which proved to be a successful method for the removal of the native oxide, as shown by XPS and STM analysis.

The surface of the LD Si substrates consists of steps and terraces with an average width of 40 nm. The step spacing and the orientation of the dimers relative to the stairs can vary between substrates cut from the same Si wafer. The average step spacing of the HD Si substrates (200 nm) is much larger compared to the LD Si substrates (20-40 nm), for the analysed Si substrates. According to the manufacturer, the miscut value should be similar for both types of substrates. However, a small difference in the miscut angle can result in a large difference in the step spacing (i.e. terrace sizes). Since the density of steps on a substrate surface might affect the oxide epitaxy, it is advised to inspect the properties of individual substrates before the film growth.

By exposing a clean Si surface to ~2 L of the residual atmosphere in the TU Wien PLD system, we were able to reconstruct the conditions of the surface exposure between its deoxidation and Sr-passivation steps performed in the JSI PLD system. We found that this level of surface exposure allowed for the preparation of a well-ordered, crystalline Si(001) surface with a clear (2×1)+(1×2) reconstruction and only a low level of C-O contamination.

Furthermore, we found that the results of the electron diffraction analysis alone are not enough to confirm that the Si surface is indeed chemically clean and structurally-ordered, as very similar diffraction patterns can be obtained from pure Si surfaces and Si surfaces covered with a thin layer of C-O contamination. Nevertheless, Ni contamination can be overlooked by electron diffraction, as a sufficient concentration of Ni is needed to form a characteristic $2\times n$ diffraction pattern. Thus, it is important to use complementary surface analysis techniques such as XPS and STM in determining the appropriate procedures for the preparation of clean Si surfaces. Considering that even a low concentration of Ni substantially increases the Si surface defect concentration, it is questionable if Ni contaminated surfaces are suitable for further use in the growth of STO/Sr/Si heterostructures.

Chapter 5

The Sr-Passivated Si(001) Surface

5.1 Introduction

After the deoxidation of a Si substrate, a crucial step in the growth of STO on Si is the passivation of the exposed Si surface. In 1998, McKee and co-workers achieved a breakthrough in the direct epitaxial growth of single-crystal perovskite STO on Si(001) by using 1/2 ML of Sr deposited on a clean Si(001)(2×1) surface as a template [28], [105]. At 1/2 ML coverage, Sr atoms occupy positions between Si dimer rows and inhibit the formation of an amorphous SiO_2 layer during the subsequent STO deposition in a relatively wide range of temperatures and oxygen partial pressures [28], [78], [105]. Conveniently, the Sr-induced Si surface reconstruction is well compatible with the STO unit cell. Nowadays, Sr-passivation has become a standard step in the procedure for the production of STO-Si pseudo-substrates, especially when MBE is used for material deposition [9].

Submonolayer Sr-structures on Si(001) have been extensively studied both theoretically [77], [78], [106], [107] and experimentally using diverse analytic techniques [108]–[114]. Recently, an atomic model of the ½ ML Sr on Si(001)(2×1) was introduced by Kuzmin et al. based on a combined DFT-STM study [115]. In most studies, Sr is deposited by MBE. Because the energies of the species impinging the substrate surface in MBE and PLD are two orders of magnitude apart (~1 eV and up to 100 eV, respectively), the density and variety of surface defects in the resulting Sr-Si surfaces are expected to differ. The difference in the type and density of defects might be further increased by surface contamination during and after the deposition, given that the pressure of the residual atmosphere in vacuum systems used for PLD is typically higher compared to the base pressure in typical MBE systems.

When it comes to Sr deposition on Si by PLD, only a few studies exist [93], [116]. The procedure for the Sr-passivation of the Si(001)(2×1) surface using PLD was developed a few years ago in our research group by Klement et al. [93]. In this procedure, elemental Sr is deposited on a deoxidized (2×1)+(1×2) reconstructed Si(001) surface at an elevated temperature, in UHV at a slow rate of 0.25 Hz and fluency of 1 J/cm^2 as illustrated in Fig. 17. The slow rate is used to help an operator to easily follow the reconstructions of the Si surface occurring at increasing Sr coverage by *in situ* RHEED. It is known that the Sr-Si surface forms a clear (3×2)+(2×3) reconstruction at 1/6 ML Sr coverage [109]. Following the number of laser pulses used to reach that coverage, one can calculate the number of pulses necessary to complete the 1/2 ML Sr coverage needed for successful passivation of the Si surface.

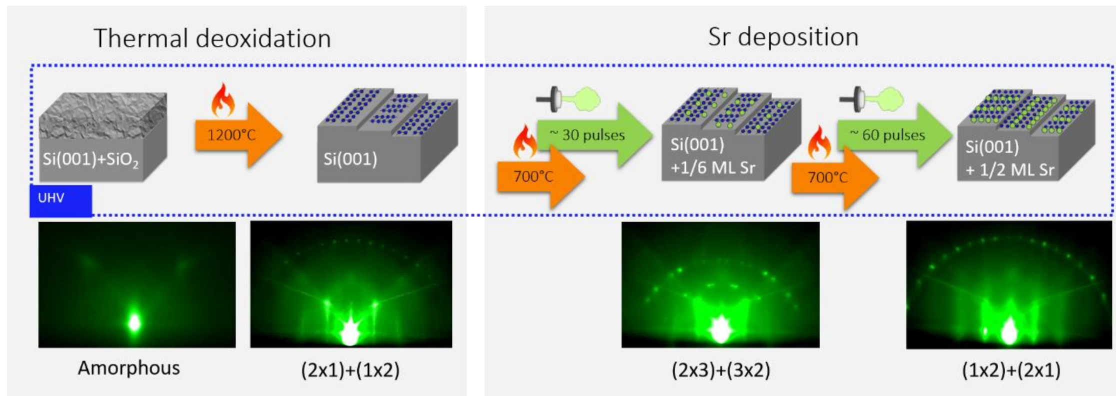

Figure 17: Procedure for the preparation of the Sr-passivated Si surface by PLD. RHEED patterns were taken in the [100] azimuth.

So far, the PLD-prepared (½ ML) Sr-Si surface has been characterized only using RHEED, which showed a clear (1×2)+(2×1) surface reconstruction indicating a well-ordered and smooth surface. However, additional characterization was needed to provide information regarding the surface morphology, local atomic structure, the variety and density of surface defects, and the chemical composition of the PLD-prepared Sr/Si(001)(1×2) surfaces.

In this chapter, first, the mechanism for the Sr-passivation of the Si surface will be introduced, together with Sr-Si surface reconstructions occurring at different Sr-coverages and various approaches for Sr deposition on the Si surface. The main part of this chapter is dedicated to the presentation of results from extended analysis of the Sr-passivated Si(001) surface on LD Si substrates using RHEED, LEED, STM, DFT, and XPS techniques. Additionally, attempts of decreasing the growth dynamics by introducing an inert background gas in the PLD chamber during the Sr deposition will be presented. The chapter concludes with an analysis of the morphology of a Sr-Si surface prepared on HD Si substrates. The presented results allow us to extract vital information for the development of an all-PLD growth procedure for the preparation of STO/Sr/Si pseudo-substrates and provides new insight into Sr-induced Si(001) surface reconstructions.

5.1.1 Ordered structures of Sr on the Si(001) surface

After the removal of the native SiO_2 layer, the Si surface reconstructs to a (2×1)+(1×2) structure by forming dimers. However, one bond per surface atom remains free, presenting the source of the high reactivity of the Si(001) surface. It has been shown that the remaining dangling bonds can be successfully passivated by deposition of 1/2 ML of elemental Sr: the resulting surface displays a $SrSi_2$ stoichiometry and exhibits a (1×2)+(2×1) reconstruction where the Sr atoms sit between the Si dimer rows, preventing the formation of an amorphous SiO_2 layer [2].

Apart from the (1×2) Sr-Si surface reconstruction, different Sr-induced reconstructions have been observed experimentally. In the study by Fan and co-workers from 1990, LEED was used to inspect several long-range-ordered structures of Sr on the Si(001) surface, under high-temperature anneals after the adsorption of various amounts of Sr [108]. They found that, between 1/6 and 1/3 ML of Sr on Si(001), a 3×2 reconstruction is dominant. In the range of 1/3 - 1/2 ML of Sr, a 2×1 reconstruction is most stable, and a 5×1 reconstruction occurs at approximately 0.7 ML coverage. For the 0.8 ML coverage, a 7×1 reconstruction is stabilized and a 3×1 reconstruction is observed at a higher Sr coverage [105]. In their

study, Sr was deposited on the Si(001) surface at RT by thermal evaporation, followed by annealing to 800 °C.

However, deposition of Sr at RT is not the most appropriate approach in the scope of PLD. Due to the higher base pressure in a typical PLD system, a bare, deoxidised Si surface contaminates during cooling, after the high-temperature flash. Therefore, deposition of Sr on a substrate at high temperatures is more convenient. An interesting fact is that the mechanism for the Si-surface reconstructions, occurring during the high-temperature deposition, is quite different compared to RT-deposition. Reiner et al. used single terminated Si substrates to demonstrate that a ½ ML of Sr, deposited at a high temperature (650 °C), replaces the top ML of Si, causing a 2×1→2×3→1×2 transition of the surface symmetry [113]. This transition is illustrated in Fig. 18. The movement of Si is driven by a formation of a 2×3 structure at 1/6 ML Sr, which removes 2/3 of the surface Si atoms. After the Sr coverage is increased up to ½ ML, another 1/3 of the top Si atoms are removed, exposing dimers that run perpendicular to the direction of the dimers of the former top layer. It was shown that both, RT and HT deposition processes, create well-ordered surfaces that result in epitaxy [113].

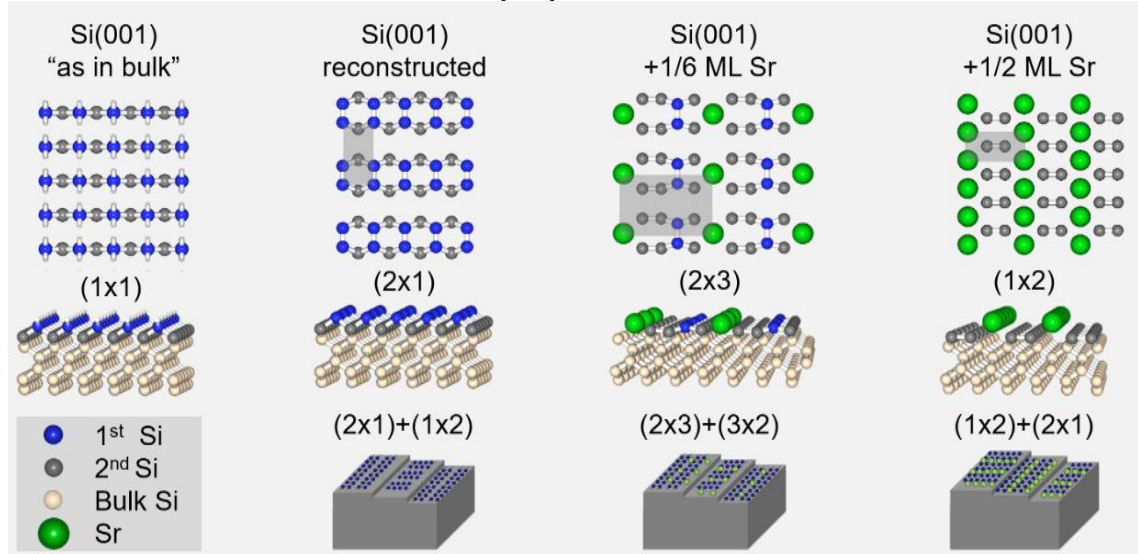

Figure 18: Si surface reconstruction transitions induced by Sr deposition at high temperatures.

5.2 Properties of the Sr/Si(001)(1×2) Surface

5.2.1 Methods

A LD Si substrate was mounted on a Ta holder with Mo clips and inserted in the PLD chamber. The substrate was degassed using IR laser heating for 12 h at 650 °C. The native oxide was removed by flash annealing for 60 s at 1200 °C, two times. The deoxidation was monitored by RHEED which showed a clear (2×1)+(1×2) reconstruction of the Si(001) surface after the second flash. Before the Sr deposition, the temperature of the substrate was decreased to 700 °C. During the deposition of ½ ML of Sr in UHV (p~8×10^{-9} mbar) on the clean Si surface, the Si surface reconstructions were monitored by RHEED. The Sr target was ablated with a 0.14 mm^2 laser spot size and a fluence of 1 J/cm^2 at a 55 mm target-to-substrate distance and a 0.25 Hz repetition rate. The number of laser pulses needed to complete the ½ ML Sr coverage was in the range of 85-105. After the deposition, a clear (1×2)+(2×1) surface reconstruction was observed. Before transfer, the sample was

cooled to T < 200 °C and transferred first to a LEED-STM system and later to an XPS system using the vacuum suitcase. The suitcase was attached to the load-lock of the LEED-STM system, which was baked for 12 h to decrease the base pressure below 5×10^{-10} mbar before the sample was inserted. With a total transfer time of 20 h, the total exposure of the sample surface was ~14 L. After the transfer, the stability of a sample surface was inspected using LEED. Before the STM analysis, the samples were cooled to 60 K to reduce the thermal drifts and to ensure sufficient conductivity of the examined surface. The STM measurements were performed with an electrochemically etched W tip in the constant-current mode. Prior to the STM imaging, the tip was conditioned on a Cu(111) surface using a controlled tip-sample interaction. After the STM analysis, the sample was transferred to an XPS system. The XPS-suitcase connection was also baked before the samples were inserted to the XPS chamber for analysis. The total exposure of the sample surface was similar as during the first transfer ~14 L.

5.2.2 Results and discussion

5.2.2.1 Controlling the Sr coverage by monitoring Si surface reconstructions

In situ RHEED patterns taken at different growth stages are shown in Fig. 19(a)-(c). The pattern shown in Fig. 19(a) was taken after the removal of the native SiO_2 and consists of well pronounced first-order streaks in the zeroth Laue zone and spots in the ½ Laue zone corresponding to a (2×1)+(1×2) surface reconstruction. Once the Sr deposition was initiated, the (2×1)+(1×2) reconstruction began to fade and a (2×3)+(3×2) pattern started to appear. Fig. 19(b) shows a RHEED pattern taken at the peak of the (2×3)+(3×2) reconstruction that occurs at 1/6 ML coverage, where spots corresponding to the 1/6 and 1/3 Laue arcs can be seen [107]. After further Sr deposition, the (2×3)+(3×2) RHEED pattern gradually transformed into a (1×2)+(2×1) pattern and reached its maximum intensity at ¼ ML coverage, which persisted until the deposition was terminated at ½ ML of Sr coverage. Fig. 19(c) shows a RHEED pattern taken after the sample was cooled to RT. The narrow first-order streaks and the sharp spots of the (1×2)+(2×1) reconstruction indicate a smooth Sr/Si(001) surface with a well-defined crystal structure.

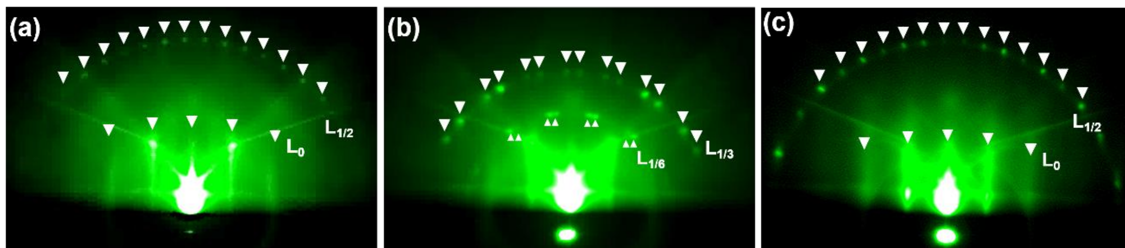

Fig. 19. RHEED patterns of the Si(001) surface reconstructions for different Sr coverages (θ_{Sr}) recoded along the [100] high-symmetry direction: (a) (2×1)+(1×2) reconstruction of the deoxidised Si(001). (b) (2×3)+(3×2) reconstruction at θ_{Sr} =1/6 ML. (c) (1×2)+(2×1) reconstruction at θ_{Sr} = 1/2 ML. The Laue zones seen in the RHEED patterns are marked with L_x.

5.2.2.2 Surface morphology

After the RHEED analysis, the sample was transferred to the LEED-STM system without breaking vacuum. The LEED pattern exhibited a clear (1×2)+(2×1) reconstruction,

indicating that the surface reconstruction remained unchanged after the transfer, as seen in the inset of Fig. 20(a). A large-scale STM image of the Sr/Si(001) surface in Fig. 20(a) shows a surface composed of terraces separated by single atomic steps (0.14 nm high). No μm-sized particulates that are sometimes observed in PLD-grown samples were detected. The observed step edges are jagged, with no significant difference in the degree of roughness between the neighbouring step edges. In comparison, the terraces of a clean 2×1 reconstructed Si(001) surface, with monoatomic steps usually exhibit alternating smooth and jagged step edges, which can be seen from an STM image of a deoxidised Si surface, prepared as described in subsection 4.2.1 and displayed in Fig. 20(b).

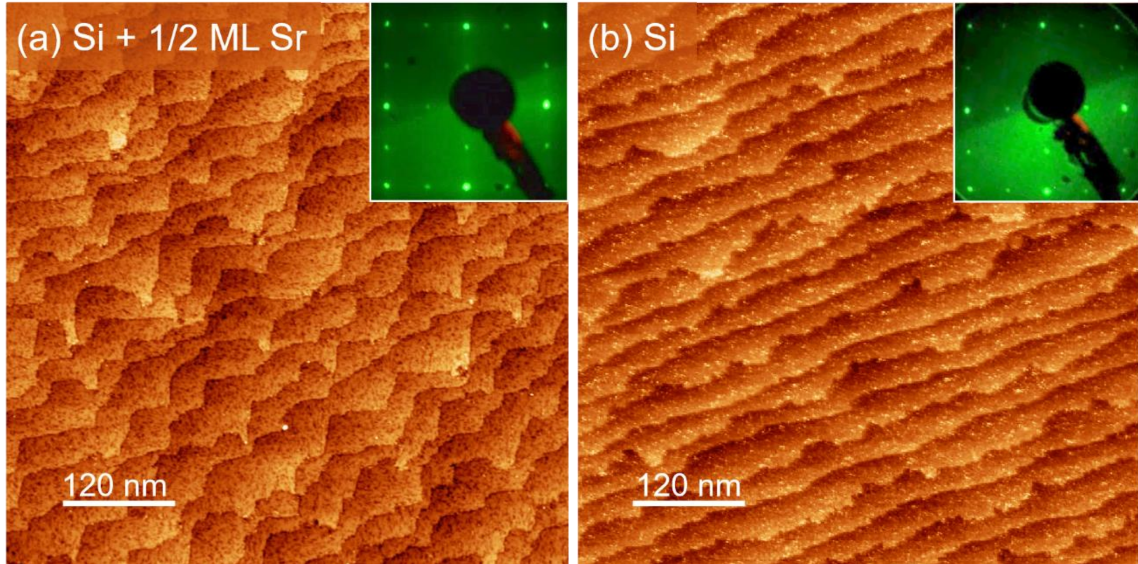

Figure 20. (a) Large-scale STM image recorded after the deoxidation of the Si(001) surface and the deposition of ½ ML of Sr. The resulting Sr/Si(001)(1×2) surface exhibits rough-edged terraces, separated by monoatomic steps. (b) Large-scale STM image of a deoxidised Si surface exhibiting straighter A terraces and jagged B terraces. LEED patterns of the Si and Sr-Si surfaces recorded at E=58 eV exhibiting the (2×1)+(1×2) and the equivalent (1×2)+(2×1) surface reconstruction, respectively, are shown in the insets. The STM images were taken at T=60 K, U=2 V and I=50 pA.

When Sr is deposited at elevated temperatures, the morphology of the terraces and step edges of the Si(001) surface undergoes a drastic change as a result of the surface diffusion of Si atoms [113], [117]. While the Si dimers remain localized during the Sr deposition at RT, the Si atoms from the top-most layer become mobile if the Sr deposition is carried out at temperatures between 700 K and 1000 K [107], [113]. The surface, therefore, undergoes several reconstructions, during which the top layer of Si atoms is re-located. At 1/6 ML Sr coverage, 2/3 of the Si dimers are transferred to and incorporated at the step edges, forming the 2×3 surface reconstruction. As the Sr coverage is further increased, the remaining 1/3 of the Si dimers also move towards the step edges, and a 1×2 pattern is subsequently formed on the newly exposed Si layer, which exhibits dimer chains rotated by 90° with respect to the original chains and rough step edges [113].

5.2.2.3 Atomic structure

High-resolution STM images of the Sr/Si(001) surface with ½ ML Sr coverage exhibit a well-ordered surface constructed of two different domains, each composed of 1D chains, running along the [011] and [0-11] directions on neighbouring terraces, as seen in Fig. 21(a). The high-resolution STM image in Fig. 21(b) shows a low-amplitude corrugation along the chains with a period of 0.39 nm, while the chains themselves are separated by 0.78 nm. The two values were derived from a Fourier transformation of an STM image of a single terrace (not shown). The measured distances agree well with the dimensions of the Si(001)(2×1) surface unit cell (0.384 nm) [100].

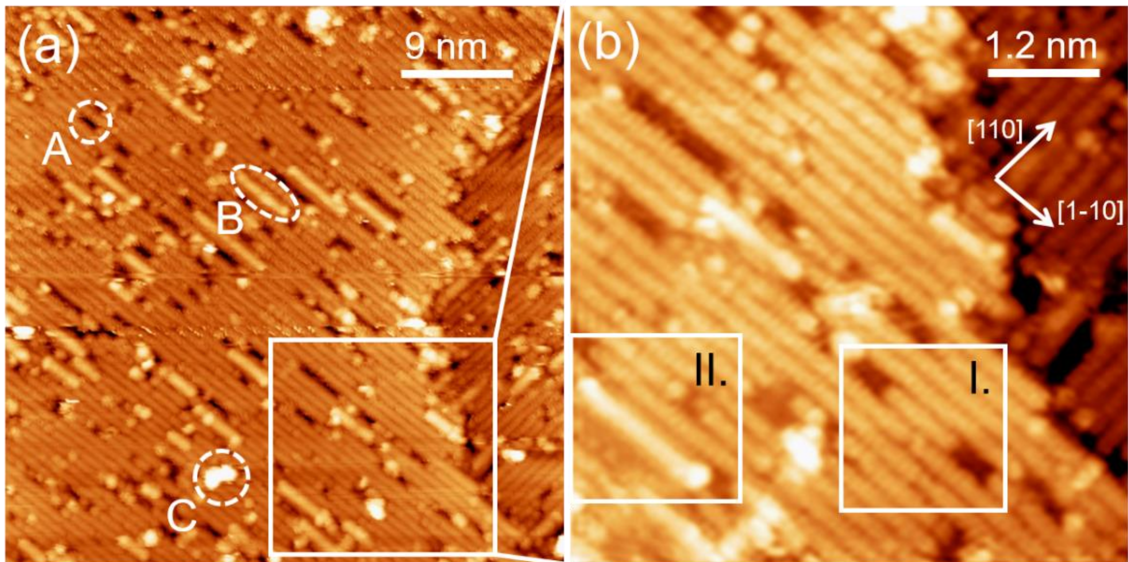

Figure 21. (a) Filled-state STM image of a Sr/Si(001)(1×2) surface composed of 1D chains running in the [0-11] and [011] directions on neighbouring terraces. Different types of surface defects are marked. (b) A high-resolution filled-state STM image exhibiting corrugation along the 1D chains. The STM images were taken at T=60 K, U=-2V and I=120 pA.

In order to identify the features in the STM images, we performed a DFT study based on a model presented in Fig. 22(d). According to our DFT calculations, the Sr atoms energetically prefer to sit in the valley-bridge sites between the Si dimer rows (A-site in Fig. 22(d)). By comparing the calculated filled-state STM images (Fig. 22(a)) to the experimental ones (Fig. 22(e) and (f)), we identified the 1D chains as rows of Sr atoms. The filled-state STM images are characterized by single large protrusions, which are related to the Si bonds participating in the bonding with Sr atoms. This is in agreement with the atomic model proposed by Kuzmin et al. [115].

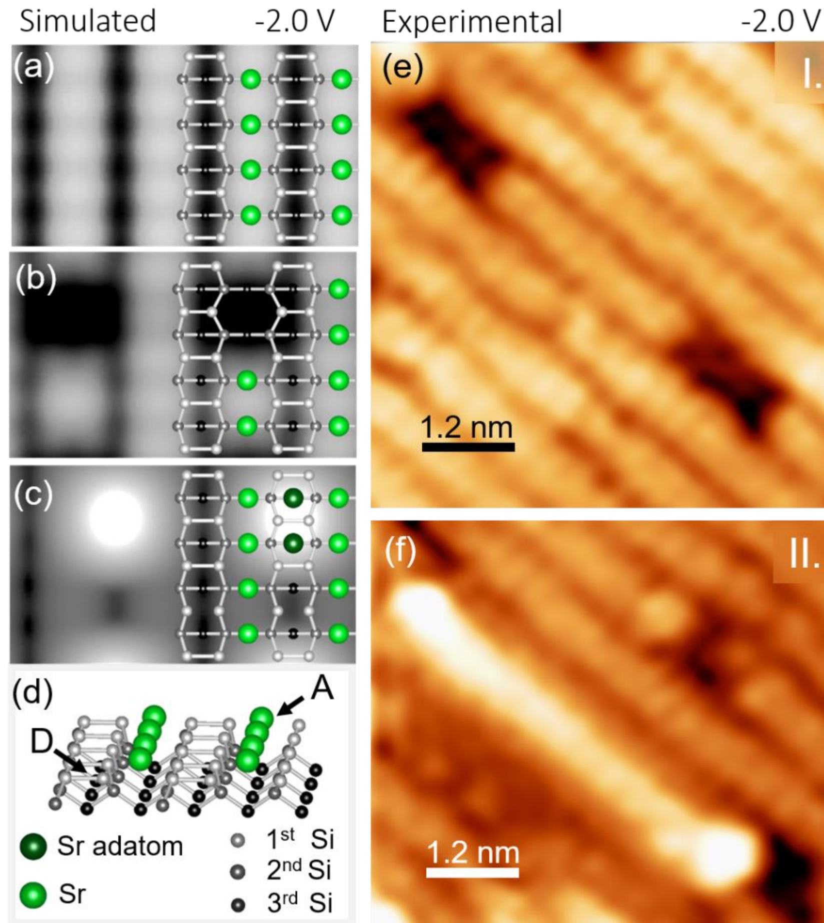

Figure 22. Simulated STM images of the Sr/Si(001)(1×2) surface: (a) the ideal structure, (b) with two Sr vacancies, and (c) with two Sr adatoms. (d) Schematics of the atomic model with marked A and D sites. (e) and (f) Magnification of the area I and II of Fig. 21(b) exhibiting an array of Sr vacancies and Sr adatoms, respectively.

5.2.2.4 Surface defects

Apart from the periodic structures, we observed three types of surface defects, as marked in Fig. 21(a). Type-A defects appear as depressions along the 1D chains with the measured length and depth ranging typically from 0.5 to 4.5 nm, and from 0.14 to 0.17 nm, respectively. Type-B defects appear as arrays of protrusions in-between the 1D chains, while the irregularly shaped and rather large protrusions randomly distributed across the surface are marked as type-C defects. The distribution of these different types of defects is homogeneous across the terraces. Furthermore, we did not observe any variation in the concentration of the defects close to the step edges. The type-A and type-B defects remained stable during STM imaging, even at a relatively high bias (up to -3 V) and tunneling currents up to 120 pA, while the type-C defects were often displaced by the STM tip during imaging, even under more moderate tunneling conditions. Thus, we conclude that the type-A and type-B defects were probably formed during the Sr deposition, while the type-C defects represent impurities, adsorbed after the Sr deposition and during the sample transfer from the PLD to the STM system. To identify the type-A and B defects, we performed further DFT calculations.

5.2.2.4.1 Type-A defects: Sr vacancies

To study the origin of the type-A defects we simulated a filled-state STM image based on the model of an ideal Sr/Si(001)(1×2) surface with two Sr atoms missing in a single chain of Sr atoms. The absence of Sr atoms causes the appearance of depressions in the simulated STM images, which are depicted in Fig. 22(b). These calculated results are perfectly consistent with the experimental image shown in Fig. 22(e). Thus, we identified the type-A defects as Sr vacancies.

As observed in Fig. 22(e), the Sr vacancies tend to arrange themselves in arrays along the 1D chains. We calculated the formation energies for a single Sr vacancy ($E_A = 0.585$ eV) and a pair of Sr vacancies in a single chain ($E_{2A} = 0.438$ eV). The case with two Sr vacancies possesses lower formation energy. This means that it is energetically favourable for the vacancies to pair, decreasing their surface mobility, and forming a nucleation site where other vacancies can agglomerate, creating arrays as a result.

5.2.2.4.2 Type-B defects: Sr adatoms

Based on the comparison between the calculated and experimental STM images, the type-B defects were identified as Sr adatoms adsorbed on top of Si dimers (site D in Fig. 22(d)). Similar to Ashman et al. [78], our DFT calculations showed that for cases with Sr adatoms, the global minimum in energy appears when the Sr sits in the trench between the dimer rows and the centre of 4 surrounding dimers (site A in Fig. 22(d)). Site D, located on top of a dimer row, in-between two dimers, is the second energetically most favoured adsorption site with an energy difference of 0.41 eV. The simulated STM images in Fig. 22(c) confirmed that the strong protrusions in the experiments (Fig. 22(f)) correspond to the local density of states of Sr adatoms located at sites D. We calculated the energy needed to form such a single Sr adatom. The resulting energy $E_B = 1.408$ eV is much higher than the vacancy-formation energy.

5.2.2.4.3 Possible adsorbates at the D-site

Aside from Sr we also considered alternative adatoms and molecules adsorbed on the D-site of the Sr/Si(001)(1×2) surface that might originate from the residual atmosphere, such as atomic O, atomic C and the CO molecule, or ones that could migrate to the top of the Sr/Si(001) surface during the surface reconstruction where Si atoms are the most likely candidates. Our first-principle calculations indicated that compared to the Sr case, the distances between the Si surface and these adatoms are relatively small, causing completely different STM features (Fig. 23) with respect to those obtained experimentally. Such theoretical results provide the support to identify the type-B defects as Sr adatoms on the D-sites of the Sr/Si(001) surface.

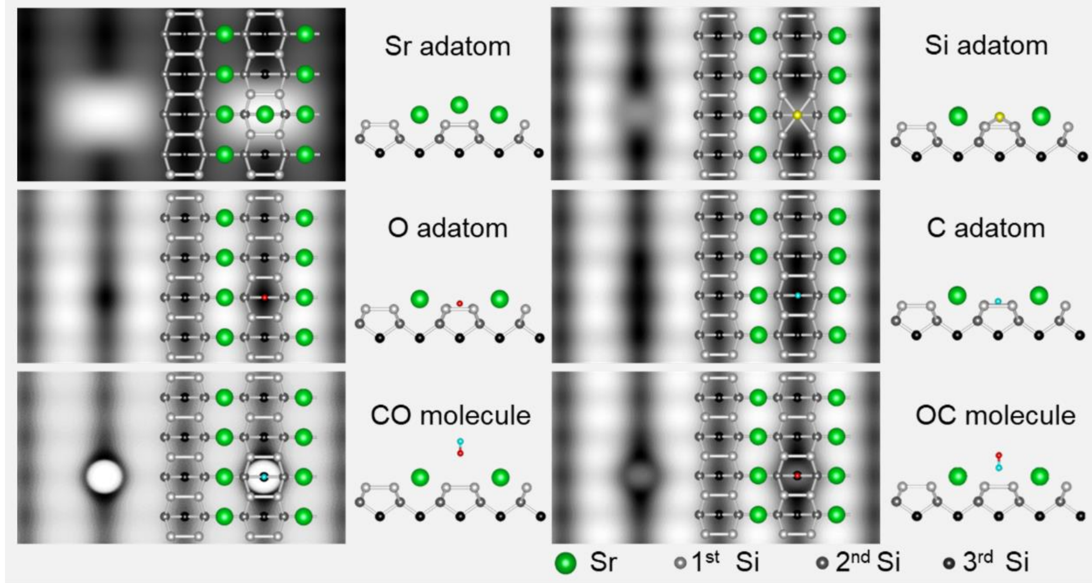

Figure 23: Simulated filled-state STM images (U=-2 V) of the Sr/Si(001)(1×2) surface with different adatoms adsorbed on the D-site.

5.2.2.4.4 Comparison of surface defects in PLD and MBE grown surfaces

The arrangement of vacancies across the Sr/Si(001)(1×2) surface observed in PLD-prepared samples is different to that found in comparable MBE-prepared samples. In the latter case, the neighbouring vacancies in the adjacent chains are frequently connected to each other and shifted by a unit cell with respect to each other along the chains. A sequence of such vacancy pairs can even agglomerate in a short chain along the [021] directions [112]. In the case of the MBE-prepared samples, the observed Sr vacancies are a consequence of the coverage being below the saturation coverage at ½ ML, and for this reason a part of the adsorption sites for Sr atoms can remain unoccupied. In the case of PLD-prepared samples, the vacancies can be formed in two ways: either they represent unoccupied sites or they were created by removing a primarily adsorbed Sr atom during a collision with the impinging Sr species. While the MBE deposition occurs near thermodynamic equilibrium with kinetic energies of the order of 0.1 eV, the Sr ions in the plasma plume during the PLD deposition can gain up to 100 eV when the deposition is carried out in vacuum, as in the presented case. Such kinetic energies are sufficiently high to form Sr vacancies.

Surface defects like Sr adatoms have not been reported when it comes to MBE-prepared Sr-Si surfaces. The energy needed to form a Sr adatom (E_B = 1.408 eV) is substantially higher than that for a Sr vacancy (E_A = 0.585 eV). However, in the case of PLD, such energy can be provided by the high-energy particles from the plasma plume. Apart from the high mean kinetic energy, the plume can reach a high degree of supersaturation, causing a rapid nucleation of very small clusters, relative to the steady-state deposition at the same average rate [118]. On this basis we propose two possible mechanisms for the formation of Sr adatoms: the displacement of Sr atoms from site A to site D due to high-energy particles impinging on the surface and nucleation caused by the local saturation of Sr atoms.

The overall density of the surface defects in the presented PLD-prepared surfaces is higher than in the cases of MBE-prepared surfaces. Primarily, the density of the defects is increased because of the nature of the PLD deposition, while some defects can be related to the higher base pressure in the PLD chamber during the sample preparation. While the

Si(001) surface normally requires a base pressure lower than 5×10^{-10} mbar to remain clean for longer periods of time [59], we observed that the surface can be successfully passivated even at a base pressure of 2×10^{-9} mbar if the Sr deposition is carried out in a short time (less than 5 min) after the removal of the native oxide. Overall, we conclude that the Si(001) surfaces prepared using the presented procedure can be successfully passivated.

5.2.2.5 Problems with surface contamination and STM analysis

Before the analysis of the Sr-Si sample presented in this chapter, similar Sr-Si samples were prepared at slightly higher base pressures in the PLD chamber (from 9×10^{-9} mbar to 2×10^{-8} mbar after bake-out). The first attempts of STM analysis of these samples were not very successful as seen in Fig. 24. RHEED and LEED showed clear and sharp features as presented in the inset of Fig. 24(a). Large area STM images showed an evident step-terrace morphology as seen in Fig. 24(a) and (b). High-resolution images showed elongated features oriented in two preferential directions perpendicular to each other on neighbouring terraces, however, we were not able to achieve atomic resolution due to a high level of surface contamination most likely caused by oxygen species from the residual atmosphere (Fig. 24(c)). We tried annealing the samples in the preparation chamber of the STM system (10-15 min, ~300 °C, 5×10^{-10} mbar) to improve the surface quality, but there was no major effect. We found that the PLD chamber was the main source of the surface contamination because the base pressure after Sr deposition can be quite high (p~5×10 mbar). After decreasing the base pressure in the deposition chamber (to 2×10^{-9} mbar by removing leaks and improving the bake-out procedure) and decreasing the time needed to transfer the samples from the PLD chamber to the vacuum suitcase (from ~25 min to 5-10 min), we were able to substantially improve the surface quality and produce STM images that reached atomic resolution. However, for regular STM analysis of PLD samples in the future, the base pressure of the PLD system should be further decreased (starting by changing the motorised valve which is not UHV tight) to enable preparation of cleaner surfaces and a higher output of STM results.

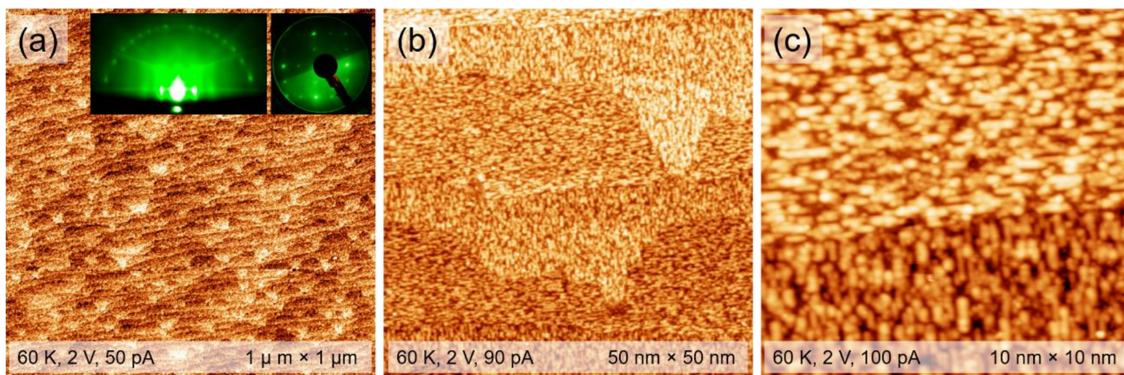

Figure 24: STM images of ½ ML Sr on Si(001) surface. (a) Large-area image showing steps and terraces. The insets show a RHEED and a LEED pattern of the Sr-Si surface. (b) STM image showing 6 terraces. Elongated features oriented in two principle directions can be observed. (c) A high-resolution STM image showing two neighbouring terraces. The elongated features run in two perpendicular principal directions.

5.2.2.6 Chemical composition

After the STM analysis, the Sr-Si sample was transferred to the XPS vacuum system using the vacuum suitcase. The composition of the sample was assessed by XPS. A survey scan of the Sr-Si sample showed the presence of a small amount of O and C, besides Si and Sr. Fig. 25(a) shows XPS spectra of the O 1s, C 1s, and Sr 3d regions. In the spectrum from the C 1s region, an additional Sr peak (Sr 3p1) can be observed at lower binding energies. Angle-resolved XPS was performed at 3 different take-off angles. As mentioned in Chapter 3, the take-off angle is defined as the angle of the X-ray source with respect to the sample surface normal, meaning that more signal from the bulk is collected at lower take-off angles. The elemental concentration as a function of the take-off angle is presented in Fig. 25(b). It seems that the O and C contributions can be related to a minor surface contamination of the sample during the transfer between UHV systems.

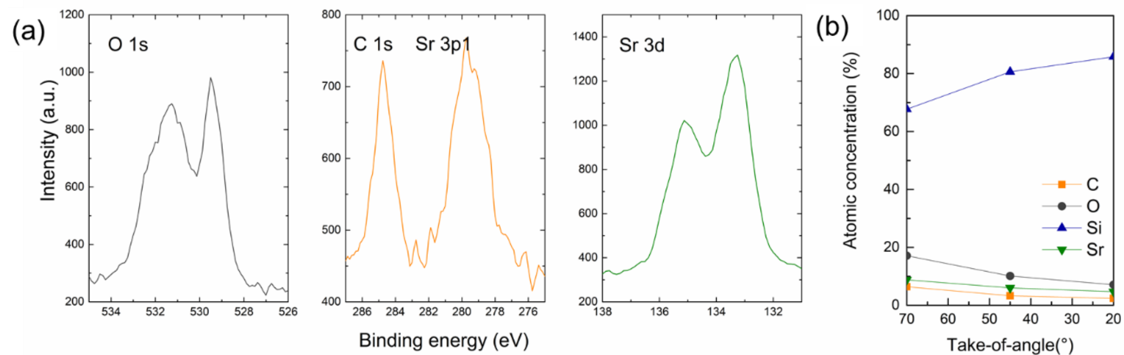

Figure 25: XPS spectra of the O 1s, C 1s, and Sr 3d regions for the Sr-passivated Si sample, taken at a take-off angle of 70° (more signal from the surface).

The main information regarding the success of the Si deoxidation and Sr-passivation can be extracted from the Si 2p region spectra. Fig. 26 shows high resolution XPS spectra of the Sr-Si sample and, for comparison, a Si substrate with the native oxide. The Si substrate with a SiO_2 layer was taken from the same wafer and sonicated in ethanol before its insertion into the XPS UHV system. The spectrum of SiO_2/Si in Fig. 26(a) has two main features. The first one, located around 99.0 eV, shows a peak doublet (Si $2p_{3/2}$ and Si $2p_{1/2}$) and corresponds to the bulk substrate signal. The other feature, located roughly around 103 eV, shows a wider peak related to the SiO_2 layer. It is clear that after thermal deoxidation, the SiO_2 layer is completely removed from the Si(001) surface.

In the XPS spectrum taken at 70° take-off angle in Fig. 26(b), an additional feature can be observed at higher binding energies. The peak disappears when the bulk signal is increased. The extra peak is represented more clearly in the fitting of the XPS spectrum in Fig. 27. The peak's appearance can be related to some surface reactions with O and C species from the residual atmosphere. Herrera-Gomez et al. found that a Si^{1+} peak starts to appear with slight oxidation of the Si surface (at 0.2 L) [110]. A small shoulder that developed at the high binding energy side of the Si bulk peak was also observed by Liang et al. after oxidation and annealing of a Sr/Si(1×2) surface [109]. Their study suggests that the source of the additional peak could be either a silicate or a reduced SiO_2 phase.

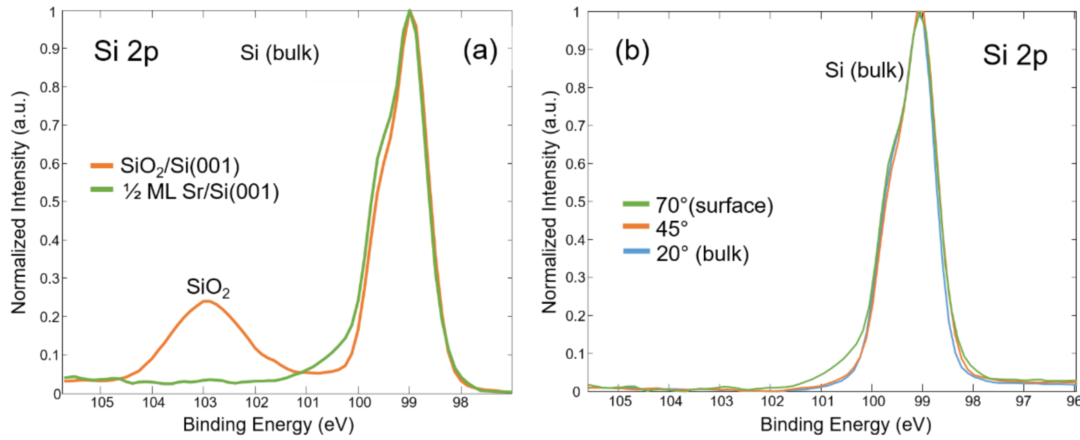

Figure 26: (a) XPS spectra of the Si 2p region for a Si substrate before and after the deoxidation and Sr-passivation steps. Take-off angle: 70° (b) Angle-resolved XPS spectra of the Si 2p region for Si substrate after deoxidation and passivation taken at different take-off angles.

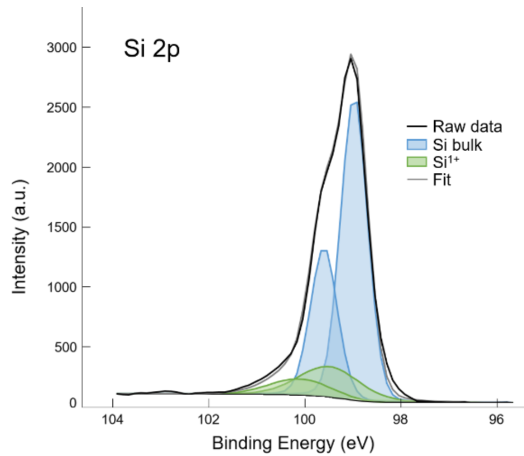

Figure 27: Fitting of the XPS spectrum of the Sr-Si surface, taken at a 70° take-off angle.

5.3 Deposition of Sr in an Inert Background Gas

One of the drawbacks of PLD of Sr performed in UHV is the high energy of plasma plume species bombarding the substrate surface [119]. When metal targets are ablated in UHV, the shape of the plasma plume is highly directional and its species can reach kinetic energies up to 100 eV that can significantly affect the substrate, e.g. by sputtering of the growing film, amorphisation, intermixing of layers or even back-contamination of the target materials [120]. There is a range of kinetic energies for the impinging particles for which surface mobility and reactivity are enhanced while the bulk remains unaffected [121]. The upper limit in this range depends on the bond strengths, but generally lies at about 50 eV. The kinetic energies of neutral species in a typical ablation plume normally lie below the threshold for bulk damage, but the energies of the ions can exceed 100 eV. However, by deposition in a noble background gas, it is possible to substantially thermalize the plasma plume through multiple collisions and therefore reduce the formation of crystallographic defects. In this section, the possibility to deposit Sr on Si(001) by PLD in an Ar background pressure was investigated.

5.3.1 Methods

A HD Si substrate was mounted on a Ta holder with Mo clips and inserted in the PLD chamber with a base pressure of 6×10^{-9} mbar. The Si substrate was first degassed and deoxidized as described in Section 4.2.1. After the second flash to 1200 °C, the substrate's temperature was decreased to 700 °C. At this point a 0.05 mbar Ar background pressure (purity 6.0) was introduced into the deposition chamber. Right after, Sr was deposited by 90 laser pulses on the Si(001) surface at 700 °C, at a 0.25 Hz frequency, and a 1 J/cm^2 fluency. These parameters are the same as for the Sr deposition described in Section 5.2.1. The deoxidation and deposition procedures were monitored *in situ* by RHEED. After the Sr deposition, Ar was removed from the PLD chamber and the sample was transferred to the LEED-STM system using the vacuum suitcase.

5.3.2 Results and discussion

Fig. 28(a) shows RHEED patterns of the Si(001) surface before, during and after Sr deposition. The typical (2×1)→(3×2)→(1×2) transition between the surface reconstructions was not observed. At the end of deposition, a RHEED pattern with sharp streaks and a few spots in the first Laue zone was displayed, indicating a partially ordered surface.

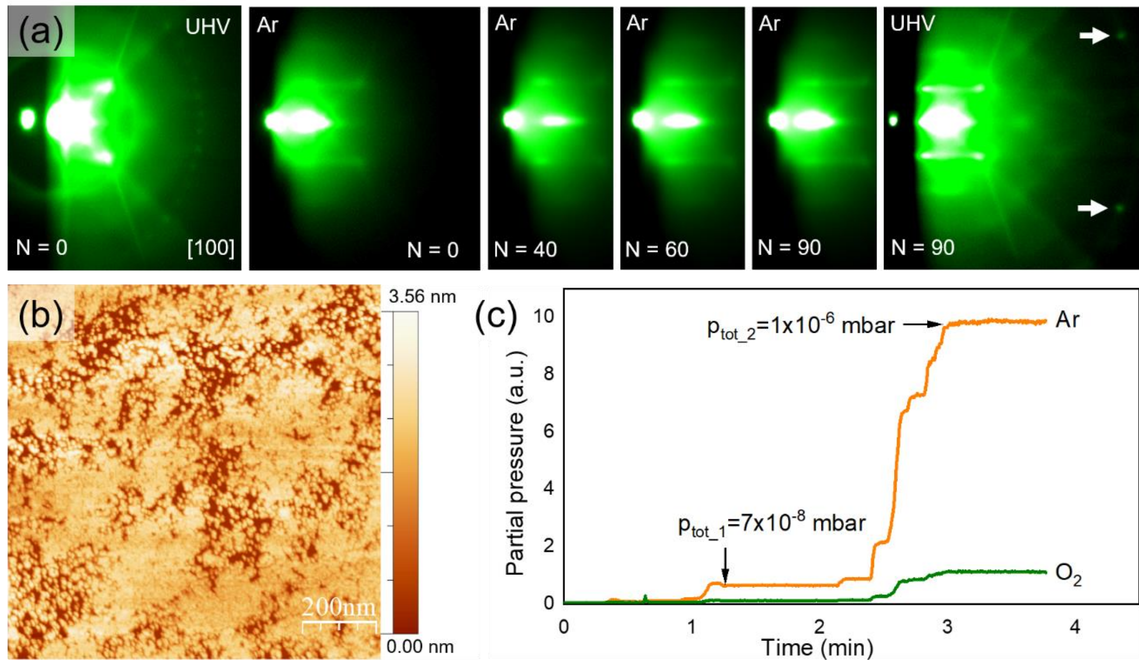

Figure 28: (a) RHEED patterns taken in the [100] azimuth of (i) a bare Si surface in UHV, (ii) a bare Si surface in Ar, the Si surface after deposition of (iii) 40, (iv) 60, (v) and 90 pulses in Ar, (vi) and a RHEED pattern of the final Sr-Si surface taken in UHV. (b) STM image of a slightly oxidised the Sr-Si surface. (c) Measurement of Ar and O_2 partial pressures as a function of time. Two events when the total pressure was increased by an operator are marked.

After transferring the sample to the STM system, LEED analysis showed a strongly diffuse pattern. STM analysis revealed a rough surface with groups of islets and formations of larger islands with a maximum height of about 3.5 nm as shown in Fig. 28(b).

The composition of the Ar atmosphere in the PLD chamber was inspected utilizing mass spectroscopy, which showed the presence of air components, such as N_2, O_2 and water

vapour in addition to Ar. Fig. 28(c) shows a measurement of the Ar and O_2 partial pressures as a function of time. The two arrows mark two events when the flow of the Ar gas was increased. The O_2 to Ar partial pressure ratio was as high as 1:10.

It was found that the contamination of the Ar gas line was caused by air leaks in valves with non-metal sealing. To prevent leakages, the valves should be replaced with UHV-compatible parts with exclusively metal seals. The second problem is the length of the Ar gas line from the gas bottle to the deposition chamber, which prevents thorough degassing, causing water vapour to remain in the line. In the future, a shorter Ar line should be installed. The purity of the Ar atmosphere could be further improved by completely separating the Ar gas line from the O_2 line and by installing gas purifiers. This way the contamination of the Si surface during the Sr deposition in Ar could be avoided and it would be possible to continue with the analysis of Sr deposition in the diffusion regime.

5.4 Sr Deposition on Heavily Doped Si Substrates

While LD Si substrates are usually used in the production of STO-Si pseudo substrates, HD Si substrates might be needed in applications where higher charge carrier concentrations are required as in the case of photoelectrochemical water splitting. Using the MBE technique, it has been shown that a Si-based photocathode with a capping epitaxial STO layer can provide efficient and stable hydrogen production from water [122]. HD Si substrates are also convenient for LT STM analysis as they are conductive at 4.2 K. We tested the Sr-passivation procedure on HD Si substrates and found interesting changes in the surface morphology.

5.4.1 Methods

After the preparation of a clean Si(001) surface, ½ ML of Sr was deposited on an HD Si substrate by PLD, following the procedure presented in Subsection 2.2.1. The deposition was monitored by RHEED. After the deposition, the sample was transferred to a separate UHV system, without breaking vacuum, where it was inspected by LEED and analysed by LT STM at 4.2 K.

5.4.2 Results and discussion

The inset in Fig. 29(a) shows RHEED and LEED patterns that were taken before and after the sample transfer, respectively. Both diffraction patterns exhibit a clear $(1\times2)+(2\times1)$ surface reconstruction characteristic for a Si(001) surface with ½ ML Sr coverage. Large-area STM images are presented in Fig. 29(a) and (b). The morphology of the terraces is greatly altered compared to the shape of the terraces present on pure Si(001) surfaces. Step edges are transformed into finger-like elongated shapes. No dimer structures or chain-like structures were observed as seen in the high-resolution STM image presented in Fig. 29(c).

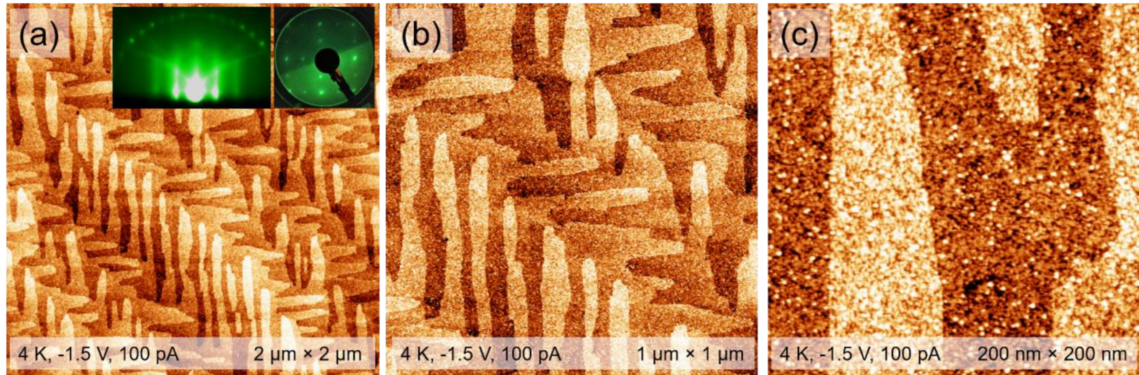

Figure 29: (a)–(c) STM images of the Sr/Si(001) surface prepared by Sr deposition on an HD Si substrate. The inset in (a) shows RHEED (left) and LEED (right) patterns of the (1×2)+(2×1) reconstruction at θ=1/2 ML Sr coverage.

The unusual modification of the surface morphology can be attributed to the accumulation of the B dopant atoms at the Si surface. The accumulation is caused by the diffusion of the dopants from the bulk due to prolonged high-temperature annealing of the Si substrate. Similar step roughening, in the form of comb-like features, has been observed at steps on vicinal Si(001) surfaces during Si homoepitaxial growth [123] and also on annealed, deoxidized HD Si surfaces [124]. Jones et al. found that by using a certain annealing temperature, sample miscut, and B doping, it is possible to produce Si(001) surfaces covered with self-organized, quasiperiodic, nm-scale step structures, with adjustable size and shape [124]. The alternation of the steps shape is a consequence of significant tensile strain induced by short B-Si bonds at high levels of B present at Si surfaces [125]. Such structures can be prepared by flashing at 1200 °C, followed by annealing at temperatures in the range from 700 °C to 950 °C, with a total time ranging from 15 min to several hours, followed by quenching to RT. Segregation of B on the Si surface was observed even on Si(001) surfaces prepared by degassing at 600 °C for 6 h, followed by several cycles of flashing at 1200 °C for only 1 s [126]. Unfortunately, the temperature profile used in these two procedures is very similar to the temperature profile in the procedure used for the Sr-passivation of Si by PLD. By shortening the annealing periods, especially after the deoxidation step, and increasing the sample cooling time after the Sr deposition, the B surface concentration on HD Si substrates could be reduced, however, it is highly unlikely to avoid it completely.

The different morphologies of the Sr-Si surfaces presented in this chapter might influence the epitaxy of STO. It is important to keep in mind that step edges present the main surface defects and their density could affect the density of dislocations in the STO film, especially because the out-of-plane parameter of the STO unit cell does not match the size of a Si(001) surface step. If one would like to create an atomically sharp interface between STO and Si, this aspect is even more important. Here STM analysis can provide crucial information, compared to RHEED and LEED analysis. Fig. 30 shows a comparison of RHEED, LEED, and STM results for HD and LD Sr-Si samples prepared in a similar manner (see Subsections 5.2.1 and 5.4.1 for Sr/LD Si and Sr/HD Si, respectively). The morphologies of the Sr-Si surfaces imaged by STM are quite different, while the diffraction patterns are very similar. In the future, it would also be interesting to study how the Sr-Si surface morphology induced by the B-accumulation influences the growth of STO thin films.

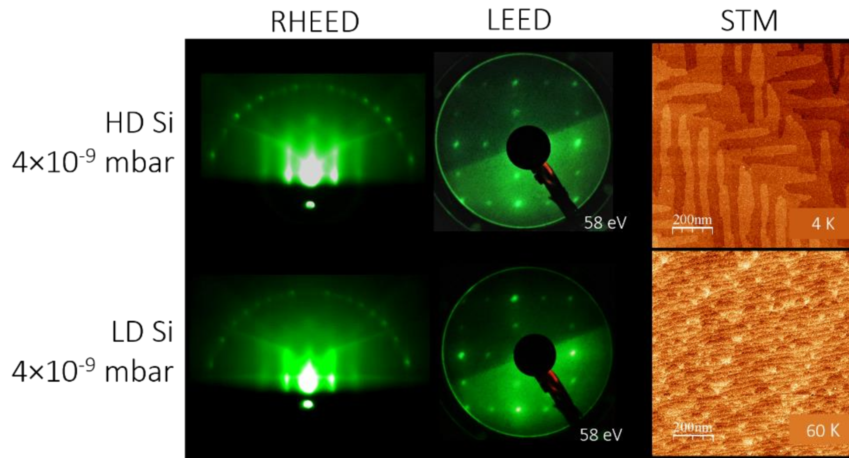

Figure 30: Comparison of RHEED, LEED and STM analysis results of a 1/2 ML Sr/Si(001) surface formed on a heavily and lightly doped Si substrate.

5.5 Conclusions

The Si(001) surface was passivated by depositing ½ ML of Sr using PLD and analysed by *in situ* RHEED, LEED, LT-STM, and XPS. RHEED monitoring during Sr deposition revealed clear Si surface reconstruction transitions from Si(001)(2×1) to Sr/Si(001)(2×3) followed by a Sr/Si(001)(1×2) reconstruction. The STM images revealed an atomically ordered surface with terraces composed of 1D chains running along perpendicular directions on neighbouring terraces. The 1D chains are separated by 0.78 nm and exhibit a low-amplitude corrugation with a period of 0.39 nm. These unit cell parameters agree well with the (1×2) unit cell size observed on similar MBE-prepared Sr-Si surfaces, while the density and variety of the surface defects are somewhat higher in the presented case. According to simulated STM images based on DFT calculations, two types of surface defects were identified and explored: arrays of Sr vacancies and Sr adatoms. The presented results show that the main difference in the types of surface defects observed in PLD-prepared Sr-Si surfaces originates from the higher energy of the particles produced during PLD performed in UHV, in comparison to particles arriving at the sample surface at thermal energies during MBE deposition of Sr on Si. XPS analysis showed that the Sr-Si surface is free of SiO_2 and only a minor silicate formation is present at the surface. These results represent the first local structural analysis of a PLD-prepared Sr-passivated Si surface. We have shown that PLD can be applied to grow high-quality Sr-passivated Si surfaces needed for the controlled epitaxy of STO and other complex oxides on Si substrates which can lead to an all-PLD integration of complex oxides with Si.

Additionally, we studied the deposition of Sr on Si in an inert background gas. During the deposition of ½ ML of Sr at 0.05 mbar Ar pressure, the Si surface was contaminated. We found that the source of the contamination were air leaks in the Ar gas line. Before any further attempts of Sr-deposition studies in Ar, the gas lines of the PLD system should be shortened and the valves should be replaced to prevent air leakages and oxidation of the Si surface prior to its passivation in a high background pressure.

Furthermore, we studied Sr deposition on HD Si substrates. STM analysis of the Sr/Si(001) surface showed a strongly modified surface with step edges with finger-like features. We found that the morphology of the surface was altered due to dopant segregation from the bulk Si to the surface. It is not clear how the altered surface atomic structure containing Si-B bonds and the surface morphology of such a Sr-Si surface would affect the STO epitaxy.

Chapter 6

$SrTiO_3$ Thin Films on Si(001)

6.1 Introduction

The two key challenges in the growth of STO on Si lie in obtaining an adequate stoichiometry and a sharp oxide-Si interface. The first can be overcome by optimizing the laser parameters, such as fluency, frequency, and laser spot size and also target composition [127], but the minimization of the interface reactions can be more difficult, since the layers grown at RT are usually amorphous, and heating during or after the deposition is required for the crystallization of the deposited material, which usually leads to the formation of amorphous silicate phases [128]. Even though the Si surface is first buffered with Sr, in the growth of the first 5-15 ML issues like oxygen diffusion into the oxide-Si interface and inadequate growth parameters can lead to reactions at the interface and a decrease of the overall properties of the oxide layer. The procedures developed for the growth of STO on Si are therefore commonly multi-staged with the deposition of the first monolayers of the oxide in an inert atmosphere or low O_2 conditions, preventing the direct oxidation of the interface; and the rest in higher O_2 pressure, so a correct stoichiometry is achieved [6], [129]. For a similar reason, the films are deposited near RTs and crystalized by post-deposition annealing in UHV.

The deposition of the STO on Si by PLD was established previously in our group by Klement et al. [54]. The multistage procedure mimics successful MBE epitaxial growths of STO on Si [130], [131] and it can be summarized in the following steps:

(1) Si deoxidation by flash annealing in UHV.
(2) Growth of ½ ML Sr buffer layer in UHV by PLD.
(3) Growth of 1-4 ML of STO in an Ar atmosphere (5×10^{-2} mbar) and RT.
(4) Exposure of the freshly grown STO to O_2 (9.3×10^{-7} mbar, 5 min, RT).
(5) Repetition of steps (3) and (4), until the desired thickness is achieved.
(6) Crystallization by annealing in UHV, after deposition of 1-3 ML of STO.
(7) Repetition of steps (3)-(5) until a thickness of 10-12 ML is achieved, thus forming an STO seed layer.
(8) For the preparation of an STO-Si pseudo-substrate, additional STO is deposited on the STO seed layer by continuous growth at high temperature and high oxygen pressure until a thickness of ~50 nm is achieved.

In this chapter, first, optimization of the procedure for the formation of an STO seed layer on Si by PLD will be presented, followed by an investigation of the evolution of the Si-STO interface structures. The chapter concludes with an analysis of the properties of the STO seed layer on Si prepared by the optimized growth procedure.

6.2 Optimization of STO Growth on Si by PLD

Previous research efforts made by our group studied the impact of parameters, such as laser fluence, substrate temperature and growth pressure, on the quality of the STO layers grown by PLD [35], [54]. It was shown that proper optimization of the laser fluence led to optimal STO stoichiometry and avoidance of large particulates formation, while an adequate argon pressure led to smoother STO layers and better crystallinity. The impact of the substrate temperature was lightly explored, but it was shown that temperatures over 545 °C led to interface reactions and polycrystallization of the films. In this work, several other growth parameters were optimised. Four groups of experiments were performed testing:

(i) The total coverage before every oxidation stage, which will be referred to as: Coverage per oxidation.
(ii) The total coverage before every crystallization stage, referred to as: Coverage per crystallization.
(iii) Crystallization procedure.
(iv) Crystallization temperature.

The research presented in Section 6.2 was led by Daniel Diaz Fernandez and published in RSC Adv. in 2017 [132]. I actively participated in all parts of this research.

6.2.1 Methods

STO thin films were deposited by PLD on LD Sr-passivated Si substrates. The Sr-Si surface with a (2×1)+(1×2) surface reconstruction was prepared as described in Chapter 5. After the deposition of ½ ML of Sr at 700 °C, the samples were cooled to RT and STO was grown following the steps described in Section 6.1. The pressures and temperatures used at each step of the Sr deposition and STO growth are summarized in Table 5. The variable parameters are presented in Table 2, together with the names of the samples.

Table 5: Fixed parameters used for the Sr deposition and growth of STO.

Parameter	Sr deposition	STO deposition
Substrate temperature (°C)	700	25
Deposition pressure (mbar)	UHV	5×10^{-2} (Ar)
Fluence (J cm^{-2})	1	1.5
Repetition rate (Hz)	0.25	1
Spot size (mm^2)	0.14	0.58

Table 6: Variable deposition parameters for all samples in this study.

	Cov_{OX} (ML)	Cov_{REC} (ML)	T_{REC} (°C)	t_{REC} (min)	Cov_{FINAL}(ML)	Sample name
Default conditions	1	2	545	15	10	S_D
Coverage per recrystallization	1	2	545	15	10	$S_{REC,1}=S_D$
	1	3	545	15	12	$S_{REC,2}$
	1	4	545	15	12	$S_{REC,3}$
Coverage per oxidation	1/2	2	545	15	10	$S_{OX,1}$
	1	2	545	15	10	$S_{OX,2}=S_D$
	2	2	545	15	10	$S_{OX,3}$
	2	2	545	15	10	$S_{PR,1}$

Crystallization process	2	2	Heating stops when streaks appear in RHEED pattern		10	$S_{PR,2}$
Crystallization temperature	2	2	485	15	10	$S_{TR,1}$
	2	2	515	15	10	$S_{TR,2}$
	2	2	545	15	10	$S_{TR,3}$

Two crystallisation procedures were used. In the first one ($S_{PR,1}$) the crystallization was performed at 545 °C for 15 min. In the second one ($S_{PR,2}$), the sample was heated with the same temperature ramp until slight signs of crystallization were seen in the *in situ* RHEED patterns. If 545 °C were reached and no crystallization signs were observed, the sample would stay at the temperature for 15 min, and then it would be cooled down, effectively mimicking the original crystallization procedure. The first crystallization of sample $S_{PR,2}$ was performed at 545 °C for 15 min, but in the subsequent crystallizations, progressively lower temperatures were necessary for the RHEED images to show some crystallization signs (500, 435, 315, and below 250 °C, respectively).

6.2.2 Results and discussion

6.2.2.1 Interface

XPS (Si 2p region) and XRR were used to explore changes in the structure and sharpness of the interface. The XPS Si 2p spectra (Fig. 31(a)) show two main spectral features.

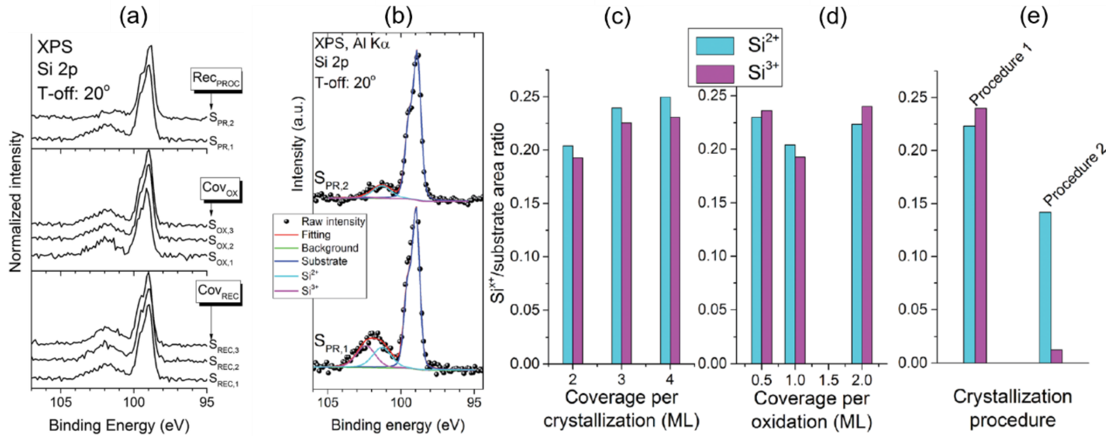

Figure 31: (a) XPS spectra of the Si 2p region for all the samples studied. Take-off angle of all the spectra: 20°. (b) XPS Si 2p region spectra fittings for samples $S_{PR,1}$ and $S_{PR,2}$. (c)-(e) Normalized (with respect to the bulk substrate signal) intensity of the Si^{2+} and Si^{3+} contributions for all samples.

The first one, a peak doublet (Si $2p_{3/2}$ and Si $2p_{1/2}$), located around 98.9 eV, corresponds to the bulk substrate signal. The other feature, located roughly at 101.9 eV, shows a wider peak and corresponds to additional phases formed at the interface, such as strontium silicates or (sub-)stoichiometric Si oxides [122]. At a first glance, all spectra show the same basic features, except for sample $S_{PR,2}$ which shows a less intense silicate phase peak that, upon careful inspection, seems shifted to lower binding energies (~101 eV). Fig. 31(b) shows fittings for samples $S_{PR,1}$ and $S_{PR,2}$ as an example, since all spectra are satisfactorily fitted using the same basic features; and they reveal that the silicate signal is actually composed of two contributions: one at 101.3 eV, and another at 102.4 eV. These contributions are assigned to Si^{2+} and Si^{3+} states, respectively [133]. Fig. 31(c)-(e) show the normalized (with

respect to the bulk substrate signal) Si^{2+} and Si^{3+} peak intensities for all the samples studied. It is clear from the data that the changes in the crystallization and oxidation coverages do not influence the intensities of these contributions. However, the intensity of both peaks, and especially that of Si^{3+} decreases in sample $S_{PR,2}$ (Fig. 31(e)). The decrease in the intensity of these peaks is a clear indication that this sample has a sharper interface, and since the rest of the samples were recrystallized for longer periods of time and at higher temperatures, it can be inferred that the interface sharpness improves when the thermal budget of the overall process is decreased. The different decrease in the ratio of these peaks suggests that this contribution is more related to the crystallization process itself.

The XRR spectra are presented in Fig. 32(a), along with the model used for the fittings. We added a thin Si layer with smaller density to the model, aside from STO and the interface layer. The additional Si layer enables to simulate possible ion implantation due to the energetic nature of the PLD deposition [134] and fits well with the data.

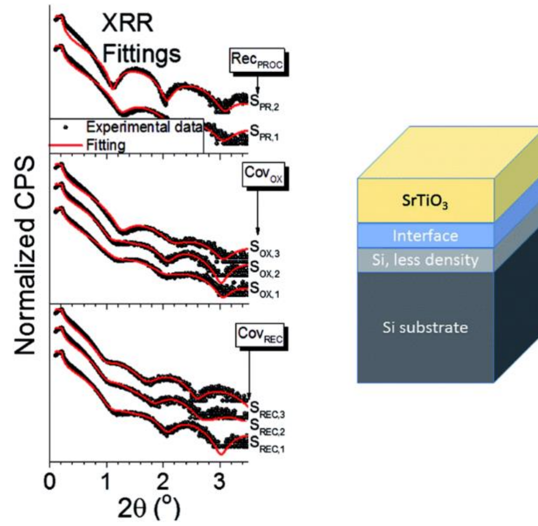

Figure 32: (a) XRR spectra for all the samples studied in this section.

Table 7: XRR fitting results for the silicate layer.

Sample	Thickness (nm)	Density (g cm^{-3})
$S_{REC,1}$	1.2 ± 0.2	4.0 ± 0.3
$S_{REC,2}$	1.5 ± 0.1	3.9 ± 0.2
$S_{REC,3}$	1.6 ± 0.2	4.1 ± 0.3
$S_{OX,1}$	1.3 ± 0.1	3.8 ± 0.2
$S_{OX,2}$	1.2 ± 0.1	3.8 ± 0.4
$S_{OX,3}$	1.2 ± 0.1	3.8 ± 0.4
$S_{PR,1}$	1.2 ± 0.1	3.8 ± 0.4
$S_{PR,2}$	0.9 ± 0.1	4.0 ± 0.5

For the interface layer, strontium silicates ($SrSiO_3$ and Sr_2SiO_4) and Si oxides were tested: the best results were obtained using a strontium silicate, with no definite improvements found when one of them was used over the other. A model without the interface layer was also tested, but the quality of the fittings decreased noticeably. The results of these fittings for the interface layer are presented in Table 7. For all samples, the density of the strontium silicate ranges from 3.8 to 4.1 g cm^{-3}, which are close to the nominal density of both $SrSiO_3$ and Sr_2SiO_4 (3.65 and 3.84 g cm^{-3}, respectively [135]). The thickness ranges from 1.2 to 1.6 nm, except for sample $S_{PR,2}$ which shows a thickness of

around 0.9 nm. These values all agree with what has been observed by XPS, and confirm that the interface sharpness is improved once the thermal budget of the experiment is minimized.

6.2.2.2 $SrTiO_3$ (seed) layer

The surface crystallinity of the STO layer was examined with *in situ* RHEED. Previous results by our group showed that, using similar conditions, STO grows on 1/2 ML Sr/Si(001) surfaces with in-plane [110] and out-of-plane [001] orientations, which agrees with previous results on similar MBE-grown STO on Si using a Sr buffer layer [50], [114]. Fig. 33 shows the RHEED patterns obtained after the final crystallization for the S_{REC} and S_{OX} samples.

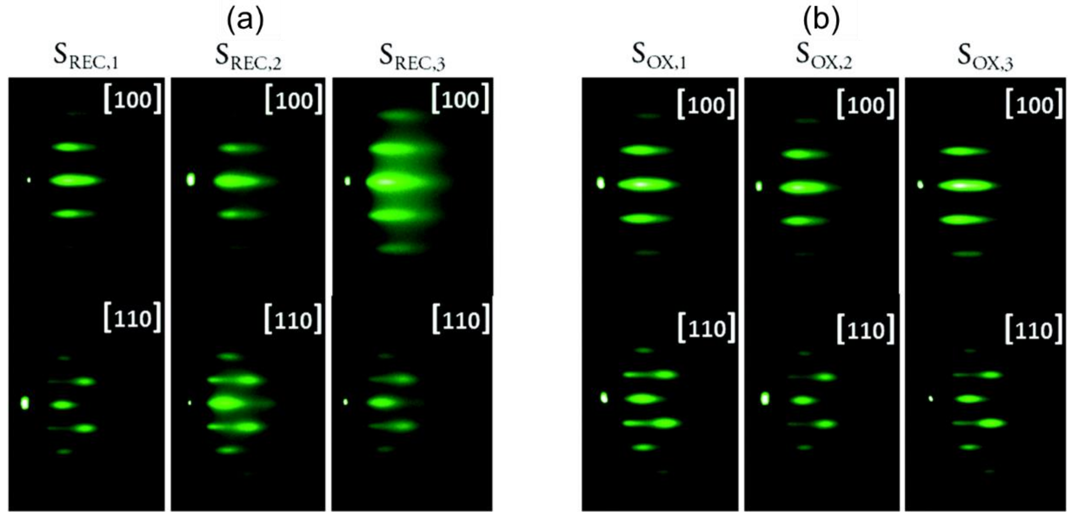

Figure 33: RHEED patterns for (a) S_{REC} an (b) S_{OX}, after the final crystallization. The respective coverages can be found in Table 6.

Results from sample $S_{PR,2}$ are not presented since the crystallization is stopped once the slightest hint of streaks is observed, which makes the RHEED data from that sample not directly comparable with the rest. Samples S_{REC} and S_{OX} show streaks in both azimuths, which means that the growth has a high degree of epitaxy, and that the orientations of these samples are consistent with the literature and our previous results. The [110] azimuth shows some streak modulation, which is consistent with previous results for epitaxial MBE growths of STO on Si [122] but indicates that the growth in this direction is not as smooth as in the [100] azimuth.

In order to extract more information from these patterns, line profiles were taken for the [100] azimuth, and the properties of the [00] streak were assessed via Gaussian fittings. The results for the FWHM of this streak for each crystallization coverage of samples S_{REC} and S_{OX} are shown in Fig. 34, along with the minimum temperature when the streaks start to be first visible in the RHEED patterns. These two sets of data serve as a qualitative comparison between samples, so the optimal parameters can be selected. Results from the second crystallization onwards are shown because no clear streaks were observed during the first one.

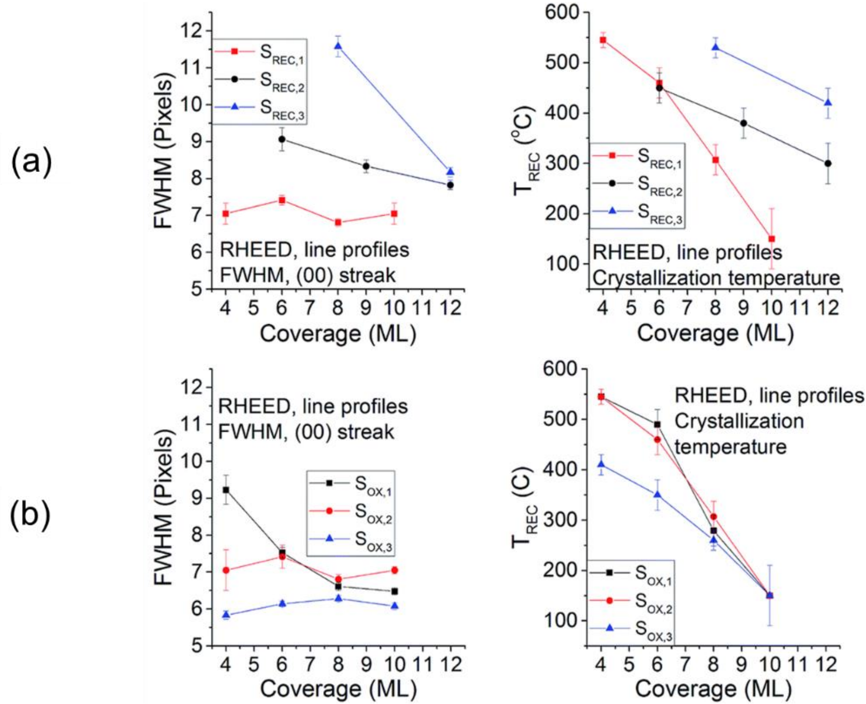

Figure 34: FWHM of the (00) streak in RHEED patterns and temperature of the sample at the time of appearance of streaks for (a) S_{REC} and (b) S_{OX} samples.

All samples show a decrease in the temperature with the coverage, which is a common property of ultra-thin layers that is caused by a combination of critical thickness, stress and interface energy effects. The graphs in Fig. 34(a) show that the best results are obtained when the crystallization is performed every 2 ML. This is especially noticeable at low coverages (2–6 ML), where the differences in the FWHM can be of up to 5 pixels; while for the final coverages of each sample (10–12 ML), the differences between the FWHM of the samples become lower (maximum of 2 pixels). The differences seen in the S_{OX} samples (Fig. 34(b)) are less important than what can be seen in the S_{REC} samples, but they show definite improvements when the sample is oxidized every 2 ML. This means that the coverage per crystallization is a more significant parameter in this growth than the coverage per oxidation. It is important to notice also that $S_{OX,3}$ was the only sample that yielded slight signs of crystallization for a 2 ML coverage, which confirms the higher quality of this sample with respect to the others.

The morphological properties and thickness of the STO samples were explored with AFM and XRR. AFM images for samples $S_{REC,1}$ and $S_{OX,3}$ are shown in Fig. 35(a) as an example, since all samples show a similar planar morphology.

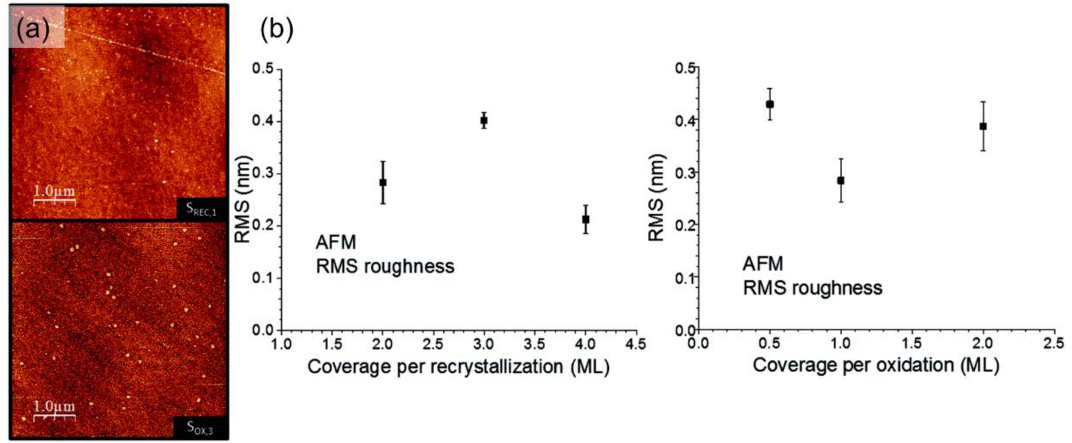

Figure 35: AFM images for samples $S_{REC,1}$ and $S_{OX,3}$. (b) RMS values for S_{REC} and S_{OX} samples.

Some small particles can be seen in some samples, with heights ranging from 3 to 4 nm, and widths from 50 to 110 nm: they could be attributed to small particulates from the STO deposition, or even contamination (the AFM images are performed *ex situ* in air). The RMS values found for S_{REC} and S_{OX} samples (Fig. 35(b)) range from 0.2 to 0.45 nm, and no trend can be observed with the variation in the crystallization or oxidation coverage. It can be therefore concluded that the variation of these parameters has no impact on the morphology of the samples. The XRR fitting results (the fittings were already shown in Fig. 32) for the STO layer are shown in Table 8.

Table 8: XRR fitting results for the STO layer.

Sample	Thickness (nm)	Density (g cm^{-3})
$S_{REC,1}$	3.1 ± 0.2	5.1 ± 0.3
$S_{REC,2}$	3.3 ± 0.3	5.1 ± 0.4
$S_{REC,3}$	3.4 ± 0.1	4.9 ± 0.4
$S_{OX,1}$	3.4 ± 0.1	5.1 ± 0.1
$S_{OX,2}$	3.1 ± 0.1	5.1 ± 0.3
$S_{OX,3}$	3.1 ± 0.3	5.1 ± 0.5
$S_{PR,1}$	3.1 ± 0.3	5.1 ± 0.5
$S_{PR,2}$	3.1 ± 0.3	3.6 ± 0.5

The thicknesses of the samples are consistently around 3.1 nm, except for samples $S_{REC,2}$ and $S_{REC,3}$ where 12 ML were deposited instead of 10. The densities are satisfactorily close to the nominal density of STO (5.11 g cm^{-3}), except in the case of sample $S_{PR,2}$ where the fittings yield a value of 3.66 ± 0.08 g cm^{-3}. This smaller value is an indication that the second crystallization procedure, while it minimizes the interface reactions and increases its sharpness, does not supply enough energy to the STO layer to fully densify.

The composition of the samples was assessed using XPS. Fig. 36 shows the XPS spectra for the Sr 3d, Ti 2p and O 1s regions, all taken at a 20° take-off angle. All the spectra show the expected STO contributions in these three regions (O 1s: 529.5 eV; Ti $2p_{3/2}$: 458.3 eV; Sr $3d_{5/2}$: 132.9 eV) [136]. The O 1s region also shows an extra contribution at ~531 eV, and a small shoulder at 533 eV: both of these contributions can be assigned to atmospheric contamination during the sample transport from the PLD to the XPS chamber.

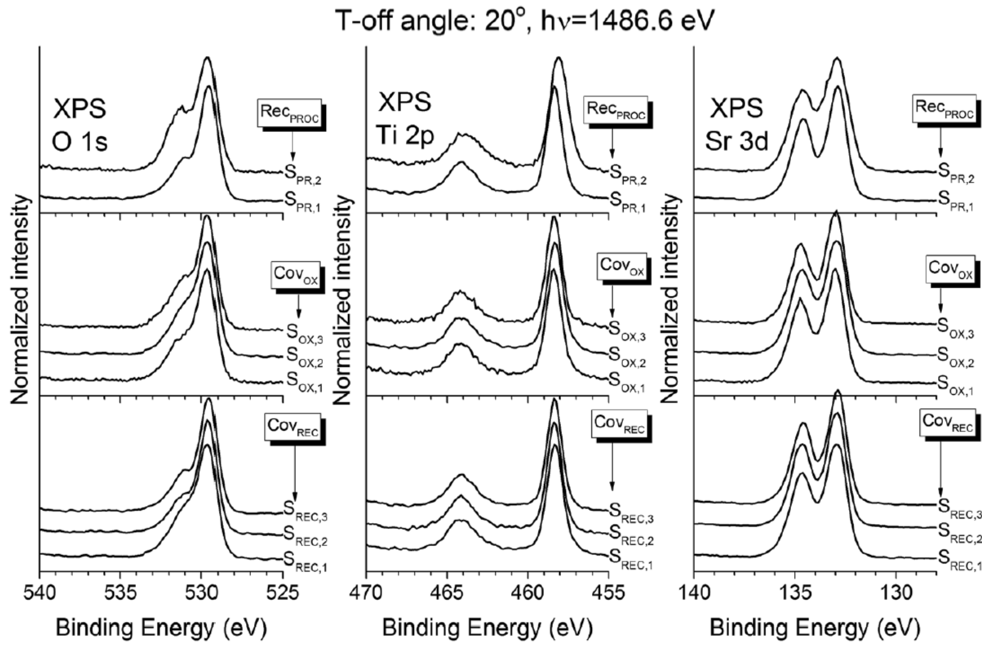

Figure 36: XPS spectra of the O 1s, Sr 3d and Ti 2p regions of all the samples, taken at a take-off angle of 20°.

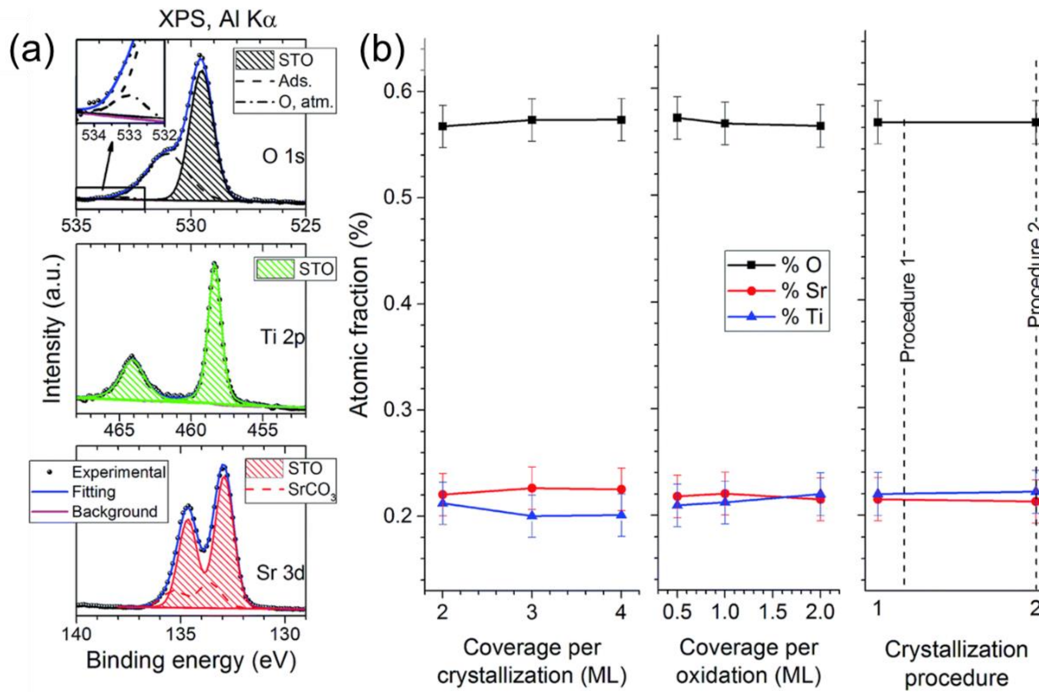

Figure 37: (a) Examples of fittings for the O 1s, Ti 2p and Sr 3d spectra of sample $S_{REC,1}$ (b) O, Sr, Ti atomic fractions for all the samples studied.

Fittings were performed in all spectra in order to assess these contributions: Fig. 37(a) shows them for sample $S_{REC,1}$. Aside from the previously discussed STO peaks, an extra contribution appears in the Sr 3d (133.6 eV), which could be attributed to surface $SrCO_3$ [137]. The formation of $SrCO_3$ at the surface is caused by the on-air sample transportation from the PLD chamber to the XPS equipment, and it is attributed to the reaction of the

topmost Sr atoms of the STO surface with CO_2. The composition of the STO layers was calculated using the STO contribution peaks, and the atomic sensitivity factors supplied by the spectrometer manufacturer were corrected by measuring a stoichiometric STO substrate cleaned in UHV conditions. Fig. 37(b) shows the results for all samples studied. All of them show atomic fractions close to the stoichiometric STO composition (60% O, 20% Sr and 20% Ti). Samples $S_{REC,1}$ and $S_{OX,3}$ show less differences in the Sr/Ti ratio than the rest, which correlates nicely with the improved surface crystallinity properties seen in Fig. 34. Meanwhile, SPR samples show almost no differences in their composition, which means that the crystallization procedure has an important effect on the density of the layer, but not on its composition.

6.2.2.3 Crystallization temperature

After determining the optimum values for coverage per oxidation, coverage per crystallization and choosing the better crystallization procedure, the study of the crystallization temperature was performed. Three 10 ML-thick STO samples, labelled as presented in Table 6, were deposited on 1/2 ML Sr/Si(001) surfaces. The same combination of parameters used for the STO overgrowth of samples was selected, and crystallization temperatures of 545 °C ($S_{TR,1}$), 515 °C ($S_{TR,2}$) and 485 °C ($S_{TR,3}$) were used. The samples were analysed by RHEED, XRR and XPS.

The RHEED patterns obtained after the last crystallization, along with the FWHM of the (00) streak obtained after each crystallization, are shown in Fig. 38. The patterns of samples $S_{TR,1}$ and $S_{TR,2}$ present almost no differences between them, showing (001)-oriented STO with a good degree of crystallinity, but the pattern corresponding to sample $S_{TR,3}$ shows broader and modulated streaks, as well as a higher background noise. The data extracted from the FWHM of the (00) streak agrees with these observations: the lowest values for the final STO crystallization are achieved in samples $S_{TR,1}$ and $S_{TR,2}$, while those for sample $S_{TR,3}$ are almost 3 pixels higher. The changes of the FWHM value with the coverages for samples $S_{TR,1}$ and $S_{TR,2}$ show that high crystallinity is achieved from the beginning when 545 °C is used, while that of the samples annealed at 515 °C improves with the coverage. Another important evidence that can be extracted from this RHEED study is that sample $S_{TR,2}$ is the only one that presents some streak structure, and therefore, some surface ordering, for a coverage of 2 ML, while the other two start presenting their first discernible streaks at coverages of 4 or even 6 ML.

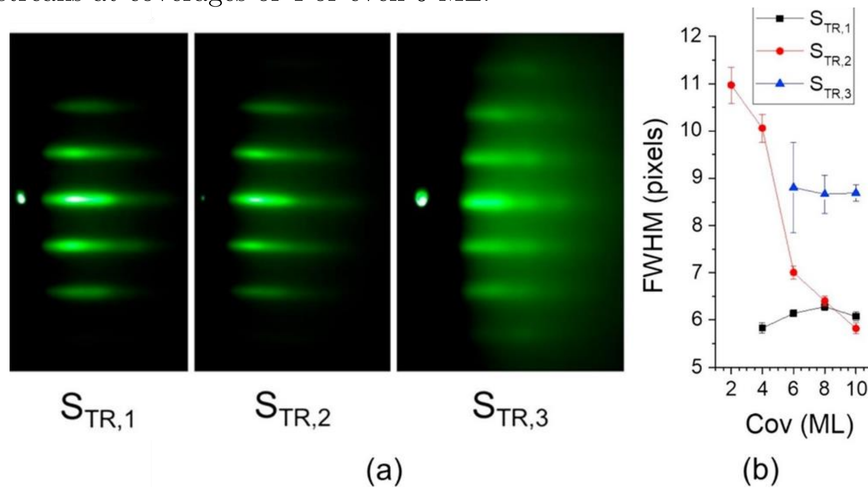

Figure 38: (a) RHEED patterns after the final crystallization of the S_{TR} samples, taken in the [100] azimuth. (b) FWHM of the (00) streak after the final crystallization.

The fittings of the XRR data, along with the values obtained from the fittings, are presented in Fig. 39 and Table 9, respectively. Samples $S_{TR,1}$ and $S_{TR,2}$ have a density satisfactorily close to that of bulk STO, but the value for sample $S_{TR,3}$ (4.5 g cm^{-1}) is noticeably lower. This can be interpreted as a consequence of the lower crystallization temperature used in this sample (485 °C).

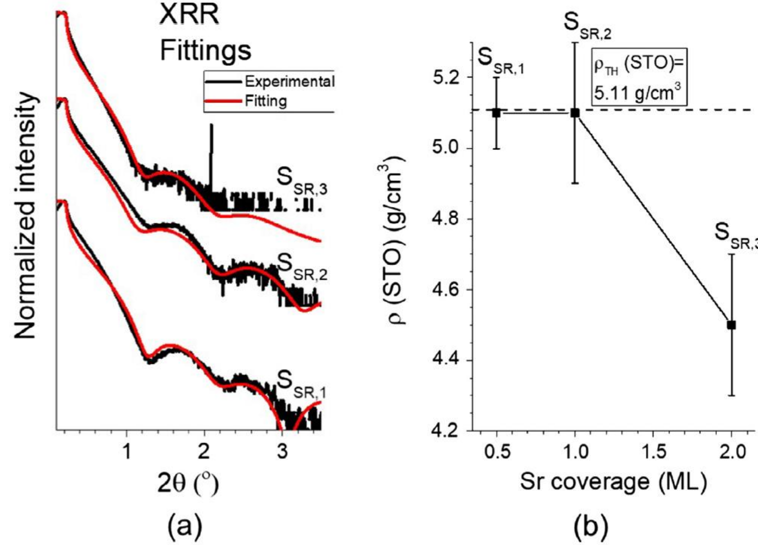

Figure 39: (a) XRR data of the S_{TR} samples with fittings. (b) Density of the S_{TR} samples, as obtained from the fittings of the XRR data. The nominal STO density (5.11 g cm^{-1}) is marked with a horizontal dashed line.

Table 9: XRR results for samples S_{TR}.

Sample	Cov_{STO} (XRR, nm)	Cov_{Silic} (XRR, nm)	Cov_{Tot} (XRR, nm)
$S_{TR,1}$	3.1 ± 0.3	1.2 ± 0.1	4.3 ± 0.4
$S_{TR,2}$	3.1 ± 0.3	1 ± 0.2	4.1 ± 0.5
$S_{TR,3}$	3.4 ± 0.2	0.9 ± 0.1	4.3 ± 0.3

Meanwhile, the Sr, Ti and O atomic percentages extracted from XPS fittings of the O 1s, Ti 2p and Sr 3d regions (Table 10) show that all the samples are oxygen-deficient, independently of the crystallization temperature chosen, and that samples $S_{TR,1}$ and $S_{TR,2}$ have the Ti/Sr ratios closer to the stoichiometric one, while that for sample $S_{TR,3}$ is further away from it, in agreement with the higher FWHM values and lower density measured.

Table 10: Sr, O and Ti atomic percentages of samples $S_{TR,}$ as extracted from XPS fitting calculations.

Sample	% O	% Ti	% Sr	% Ti/% Sr
$S_{TR,1}$	57 ± 6	21 ± 2	22 ± 2	96 ± 18
$S_{TR,2}$	58 ± 6	21 ± 2	21 ± 2	99 ± 19
$S_{TR,3}$	56 ± 6	18 ± 2	26 ± 3	70 ± 14

6.2.2.4 Optimized parameters for PLD of the STO seed layer

The presented results indicate that the best combination for the growth of the highest quality STO samples is the deposition of 2 ML of amorphous STO, oxidation of these 2 ML, and crystallization of the oxidized 2 ML at a temperature of 515 °C for 15 min. They also show that decreasing the thermal budget leads to an interface sharpness improvement, but decreasing it too much leads to a STO layer with a lower density. These results can be explained as a result of the necessary balance between the minimization of the thermal budget, critical crystallization thickness, and sufficient coverage of the buffer layer. As it was clear from the XPS results of the interface, the thermal budget has to be minimized as much as possible in order to increase the interface sharpness, but the decrease in the density of sample $S_{PR,2}$ means that a minimum amount of time and temperature needs to be applied to the sample in order to fully densify the STO layer. The results shown in this work suggest that a UHV heating of 515 °C for 15 min fulfils these two conditions satisfactorily. Meanwhile, the combination of 2 ML for the crystallization and oxidation stages can also be explained in the same terms. A higher coverage needs more energy to crystallize, so it should be minimized as much as possible; but a certain amount of material should be deposited so the coverage is above the critical thickness. The results show that 2 ML is the best amount of amorphous STO in order to achieve this balance during the crystallization phase. Meanwhile, the amount of material deposited before the oxidation stage must be as high as possible to ensure a full coverage of the Sr-passivated Si surface.

Taking into account all the data gathered from these four sets of experiments, as well as that from the previous studies of our research group [35], it can be concluded that the combination of parameters which yields the best balance between STO stoichiometry and density and interface thickness for the growth of ultra-thin STO samples is that of sample $S_{TR,2}$, which are as follows:

(i) Sr buffer layer growth: 1/2 ML, fluence of 1 J/cm^2, frequency of 0.25 Hz, spot size of 0.14 mm^2, and a substrate temperature of 700 °C.

(ii) STO layer: fluence of 1.5 J cm^{-2}, frequency of 1 Hz, spot size of 0.58 mm^2, growth of 2 ML of STO in an Ar atmosphere of 5×10^{-2} mbar, followed by an exposure to 9×10^{-7} mbar of O_2 for 5 min, and an UHV annealing for 15 min at a temperature of 515 °C.

The combination of parameters used for sample $S_{TR,1}$ also yield satisfying properties, but the better crystallinity observed at low coverages in the sample (from 2 ML onwards instead of four) is a striking feature that, in our opinion, makes it more desirable as a pseudo-substrate. Our results prove that this temperature provides an optimal balance between interface reactions and minimal crystallization energy: 545 °C provides the system with enough energy for the STO to properly crystallize, but it promotes a higher rate of reactions at the interface, creating a thicker interface (1.2 nm according to XRR, Table 8), and disrupting the proper crystallization of the first two ML of material; while 485 °C preserves the interface as effectively as 515 °C (0.9 nm according to XRR, Table 8) but at the cost of the lower STO density.

6.3 Properties of STO Ultra-Thin Films

After the optimization of the parameters for the growth of STO ultra-thin films, our research focused on the formation of the STO-Si interlayer during the film growth and the properties of the resulting ~10 ML thick STO films. These thin films can serve as a basis for the integration of thicker STO films and functional oxides with Si substrates. In the article by Diaz-Fernandez et al. [138] that followed the work presented in Chapter 6.2, a 50 nm thick film was grown in a continuous manner (higher O_2 pressure and high substrate temperature) on a 10 ML thick STO film prepared using the optimized growth procedure. TEM analysis of the resulting STO-Si pseudo-substrate showed that a 1–2 nm thick silicate layer is present at the Si-STO interface.

In the last part of this thesis, the formation of the silicate interlayer will be carefully explored in order to answer the following questions: at which steps of the STO film growth does the silicate interlayer form: (i) does it evolve through the preparation process, (ii) does the majority of the silicate interlayer form during the deposition of the first 2 ML of STO, (iii) or after subsequent annealings? Finally, the crystal structure, the chemical composition and the functional properties of the nominally 10 ML thick STO films will be presented.

6.3.1 Methods

Four samples with different thicknesses of the STO film were prepared by PLD following the optimized multi-step procedure for the growth of STO on Si (presented in Chapter 6.2). STO films with 2, 4, 6 and 10 ML nominal thicknesses were prepared.

The nominal thicknesses were assessed based on results from a separate experiment where XRR was used to determine the thickness of a thicker STO film. A 37.6 nm thick STO layer was prepared by deposition of 6000 pulses of STO on a Sr-passivated Si surface. Conditions for the STO deposition were the same as for the preparation of the STO seed layer (0.05 mbar (Ar), RT, 1 Hz, 1.5 mJ cm^{-2}, 0.58 mm^2). The thickness of the prepared film was determined based on XRR fitting (Fig. 40). The model used for the fitting consisted of a single 37.6 nm thick layer of STO on a Si substrate. Other fitting parameters are given in the inset of Fig. 40. It was found that the deposition rate of STO under the presented conditions is 1/86 ML per pulse, or in other words: the number of pulses needed to achieve 1 ML of STO coverage is 86.

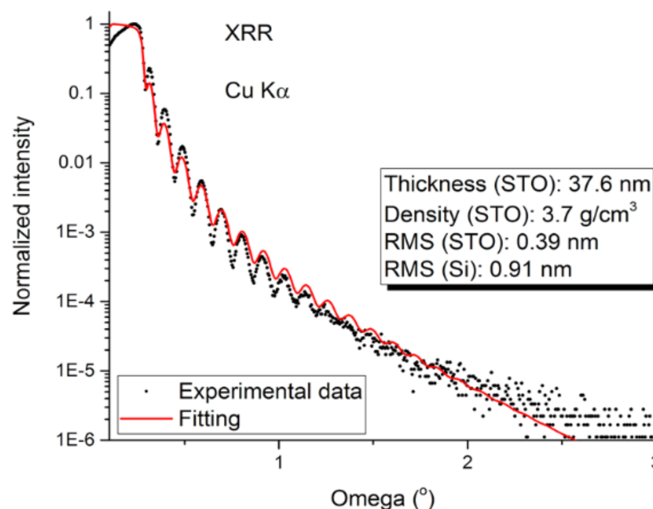

Figure 40: XRR data and fitting. The main fitting parameters are listed in the inset.

However, it is important to keep in mind that it is not necessary that the total amount of deposited material results in the same amount of a crystallised STO film – a part of the deposited amount could participate in the formation of a silicate layer. With that in mind, the samples in this chapter will be distinguished according to the number of deposition-oxidation-crystallization (D-O-C) cycles that were used in the preparation of the STO films, as presented in Table 11.

Table 11: Growth parameters for samples S_{CY}.

Number of laser pulses	Number of D-O-R cycles	Sample name
2×86	1	$S_{CY,1}$
4×86	2	$S_{CY,2}$
6×86	3	$S_{CY,3}$
10×86	5	$S_{CY,4}$

Samples $S_{CY,1\text{-}4}$ were analysed by RHEED and XPS, while the properties of sample $S_{CY,4}$ were additionally studied by GIXRD with a synchrotron source of radiation and PFM.

6.3.2 Results and discussion

The surface crystallinity of the STO films was examined using *in situ* RHEED. Fig. 41 shows the RHEED patterns taken at two different azimuth angles. All four STO films were deposited on high-quality Sr-passivated Si surfaces (Fig. 41(a)). Fig 41(b) shows a RHEED pattern of the sample surface after the deposition of the first 2 ML before the oxidation and crystallization steps (similar for all 4 samples). It can be seen that the surface crystallinity is lost after the deposition of STO − the film deposited at RT is amorphous (see Apendix B). Every deposition of a 2 ML STO film is followed by an oxidation and a crystallization step. Fig 41(c) shows RHEED patterns obtained after the final crystallization for samples S_{CY} with different thicknesses. It can be seen that the surface crystallinity is increasing with increasing number of D-O-C cycles. Sample $S_{CY,4}$ shows clear streaks in both azimuths, indicating a high degree of crystallinity of the 10 ML STO film. The streak modulation in the [110] azimuth is a sign of a decreased surface smoothness in this direction in comparison to the [100] azimuth.

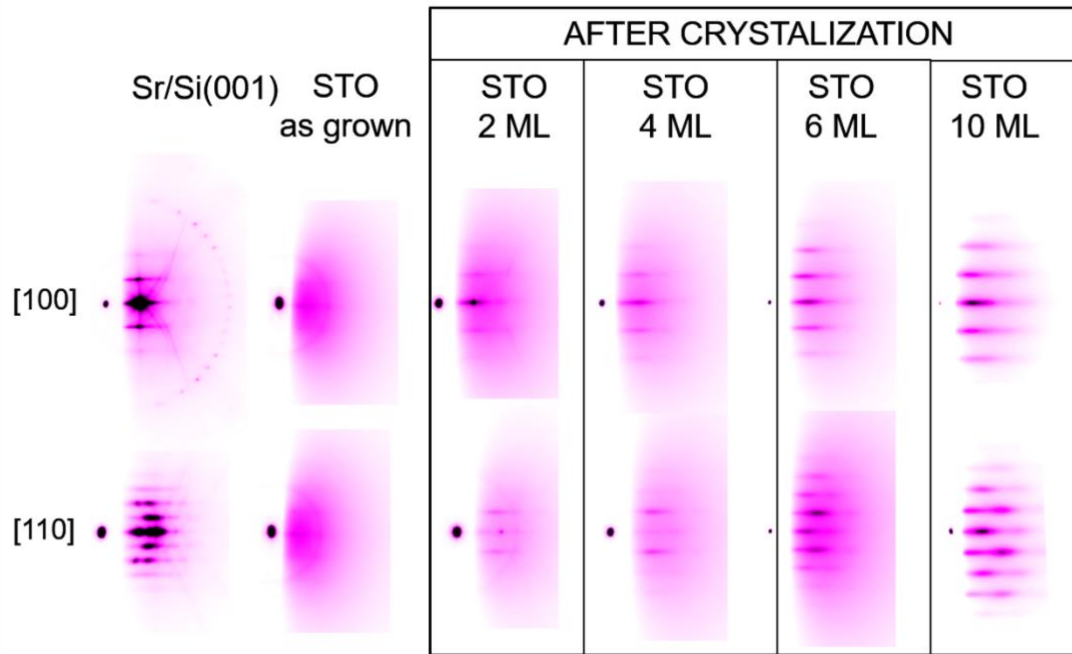

Figure 41: RHEED patterns of the surfaces of samples S_{CY} taken: (a) before STO deposition, (b) after the deposition of 2 ML STO film, and (c) after the final crystallization for all four samples. The negatives of the original RHEED pattern images are presented to allow for a higher resolution of the figure in the printed version of this work.

The chemical composition of the S_{CY} samples was studied using XPS. Samples $S_{CY,1}$ and $S_{CY,3}$ were transferred from the PLD to the XPS system using the vacuum suitcase, while samples $S_{CY,2}$ and $S_{CY,4}$ were exposed to air for a short time during transfer from the PLD to the XPS system. XPS spectra for the O 1s, Ti 2p, C 1s, Sr 3d, and Si 2p regions, all taken at a 20° take-off angle, are presented in Fig. 42.

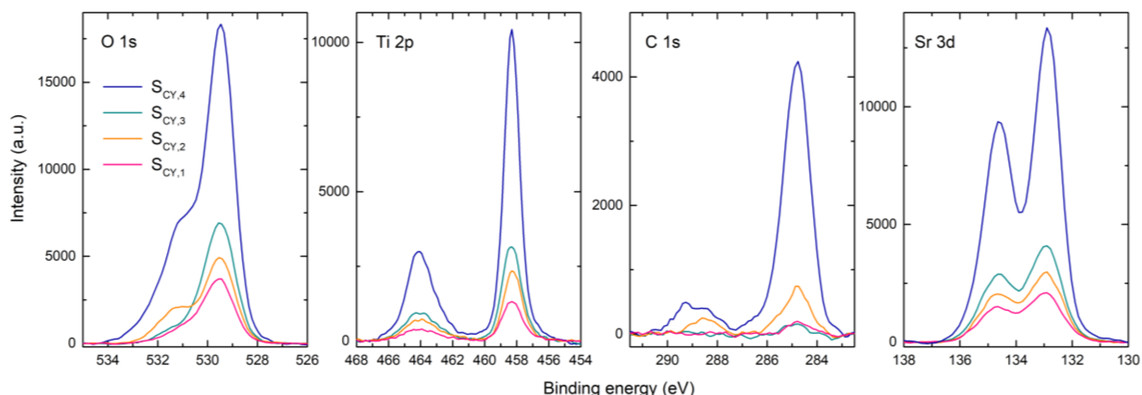

Figure 42: XPS results for samples S_{CY}.

The binding energies of these spectra were adjusted according to the elemental Si peak (99.0 eV). The effect of exposing the samples to air can be seen in the spectra from the C 1s and O 1s regions. In the C 1s region, two peaks can be observed. The peak at 284.8 eV, present in all four spectra, is substantially higher for samples $S_{CY,2}$ and $S_{CY,4}$ and can be attributed to the adventitious carbon contamination, while the peak at ~288.8 eV, present only in spectra from samples $S_{CY,2}$ and $S_{CY,4}$, can be assigned to surface $SrCO_3$. The

formation of $SrCO_3$ is due to reactions of the surface Sr atoms of the STO film with CO_2 from air [137]. In the O 1s region, an additional contribution can be observed at higher binding energies (~531 eV) in spectra for samples $S_{CY,2}$ and $S_{CY,4}$, (see the fitting in Fig. 46 for sample $S_{CY,4}$). An extra peak can also be observed in the Sr 3d region (133.6 eV) for sample $S_{CY,}$, regardless of whether the samples were exposed to air or not, which gives us reason to believe that this additional peak can be attributed to formation of silicates at the STO-Si interface and not to surface $SrCO_3$ as considered in our previous work (Subsection 6.2.2.2). However, the origin of the different contributions in the spectra from the Sr 3d region is difficult to interpret because compounds with different composition can have peaks at the same energy.

6.3.2.1 The STO-Si interface

The most relevant information regarding the STO-Si interface can be extracted from the Si 2p region scan. The XPS Si 2p spectra (Fig. 43(a)) show two main spectral features. The first one, located around 99.0 eV, corresponds to a peak doublet (Si $2p_{3/2}$ and Si $2p_{1/2}$) of the bulk substrate signal. The other feature located at higher binding energies ranging from 101.5 eV to 103 eV shows a wider peak, and corresponds to additional phases formed at the interface, such as strontium silicates or (sub-)stoichiometric Si oxides [139]. As described in Subsection 6.2.2.1, the silicate peak is a convolution of Si^{3+}, Si^{2+} and Si^{1+} oxidation states. Since we were not interested in the contributions of individual oxidation states at this point of the study, we considered the silicate peak as a whole. The Si substrate peak was fitted as a doublet, while the silicate peak was fitted by a single peak. The ratio of the silicate peak area to Si^0 peak area for samples exposed to a different number of D-O-R cycles is presented in Fig. 43(b). It can be seen that the ratio is increasing with increasing number of cycles – the silicate interlayer expands with every D-O-R cycle. During the annealing step, the diffusion of atoms is increased which leads to additional reactions at the STO-Si interface and consequently to an expansion of the silicate interlayer.

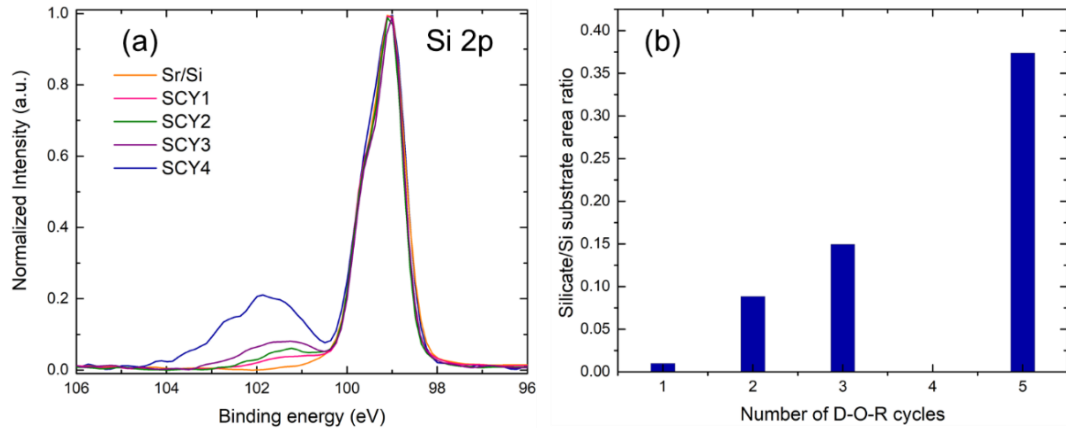

Figure 43: (a) XPS Si 2p region for samples S_{CY}. (b) Silicate/Si substrate peak area ratio as a function of number of D-O-R cycles.

6.3.2.2 The STO thin film

In order to examine the in-plane orientation and epitaxial relationship between the STO film and the Si substrate, we performed reciprocal space mapping (RSM) of an asymmetric STO reflection using synchrotron radiation with a photon energy of 20 keV. The results presented in Fig. 44(a) show two distinct reflections, a clear (111) Si reflection and a very

faint and broad (101) STO reflection. The K value of the STO peak corresponds to the diagonal of the STO unit cell, which shows that STO grows along the (001) direction, rotated in-plane by 45° in respect to the Si lattice. A magnified region around the (101) STO reflection is presented in Fig. 44(b). There is a wide spread of contributions without an obvious peak in intensity which makes this data difficult to interpret. It is hard to separate the contributions from the spread in crystallite orientations and the spread in unit cell parameters. However, some assumptions can be given.

We divided the STO reflection to three regions and assigned representative K and L values to those three regions. We took line profiles at 3 different K values: one close to the Si reflection, one in the middle of the STO reflection and one at lower K values as shown in Fig. 44(b). The line profiles were fitted by Gaussian curves. The central L values along with FWHM of the peaks are presented in Table 12. The in-plane and out-of-plane lattice parameters were calculated according to the representative K, L values, as presented in Table 11. Region 2 was inspected in more detail by performing RSM at L=1.37 and a L scan at fixed H and K (H=K=1.38) as presented in Fig. 44(c) and (d), respectively.

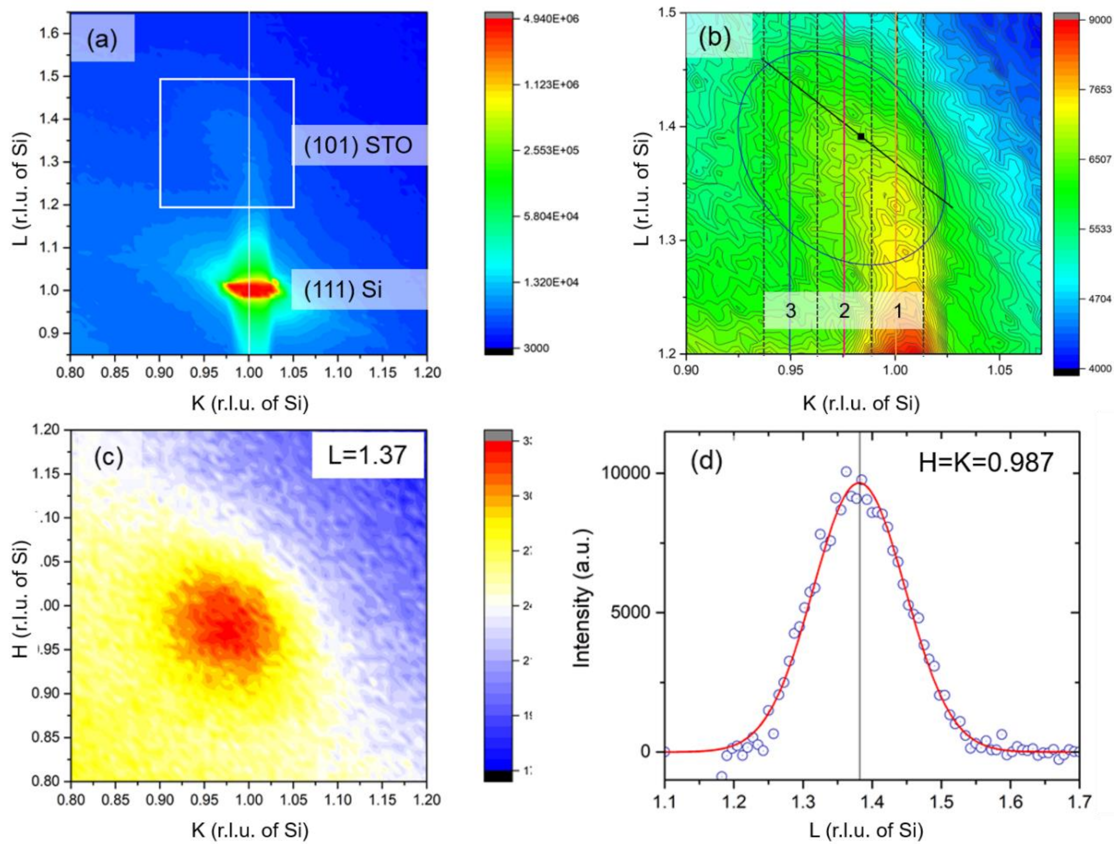

Figure 44: (a) K-L RSM of sample $S_{CY,4}$. (b) Magnification of the area marked in (a) with the (101) STO peak. The K, L values corresponding to the STO bulk lattice parameters are marked by a black dot. The black line represents pairs of K, L values corresponding to a constant unit cell volume equal to STO bulk unit cell volume, assuming H=K. The coloured lines marked with numbers represent 3 line profiles for 3 representative parts of the STO reflection. (c) A RSM taken at L=1.37. (d) L-Scan at H=K=0.987. Data points are marked with blue circles, while the red line represents the Gaussian curve fit. The analysis was performed using synchrotron radiation with a photon energy of 20 keV.

Table 12: Values for 3 different regions.

Region	K (r.l.u. of Si)	L (r.l.u. of Si)	FWHM (%)	a (nm)	c (nm)	$\%V_{\text{STO bulk}}$ (%)
3	0.950	1.39	10.4	0.404	0.391	107
2	0.975	1.38	10.0	0.394	0.393	102.5
1	1.000	1.37	8.2	0.384	0.397	99
STO bulk	0.984	1.390	/	0.3905	0.3905	100

A part of the STO film (Region 1) is compressed in the in-plane direction and expanded in the out-of-plane direction, with the unit cell volume similar to the bulk STO value. To compensate the in-plane compression, the cell expands in the out-of-plane direction in order to maintain a constant unit cell volume. The in-plane compression can be attributed to the strain induced by the STO-Si lattice mismatch. The values from Region 2 represent a part of the STO film exhibiting a cubic unit cell with a slightly larger volume compared to the bulk, while a small part of the STO film (Region 3) is expanded more in the in-plane direction than in the out-of-plane direction with a unit cell volume about 7% larger than the bulk unit cell. The expansion of the unit cell could be related to tensile strain induced due to the large difference of the coefficients of thermal expansion between the film and the substrate [140] or to off-stoichiometry [141], [142]. Stoichiometric STO films have the same lattice constant as that of the single crystal STO, while nonstoichiometric STO films, both Sr-rich and Ti-rich, show lattice expansions proportional to the degree of off-stoichiometry. The unit cell expansion could also be a consequence of oxygen vacancies, which are expected to arise due to PLD growth of STO in an oxygen-free atmosphere [143].

To further explore the origin of the STO unit cell expansion, we performed XPS analysis of the STO film from sample $S_{CY,4}$. The sample was transferred from the PLD to the XPS system in air. The normalized XPS spectra for the O 1s, Ti 2p, C 1s and Sr 3d regions, all taken at a 20° take-off angle, together with the XPS spectra of an STO single crystal, are presented in Fig. 45. The charge correction of these spectra was made with respect to the adventitious C 1s component at 284.8 eV.

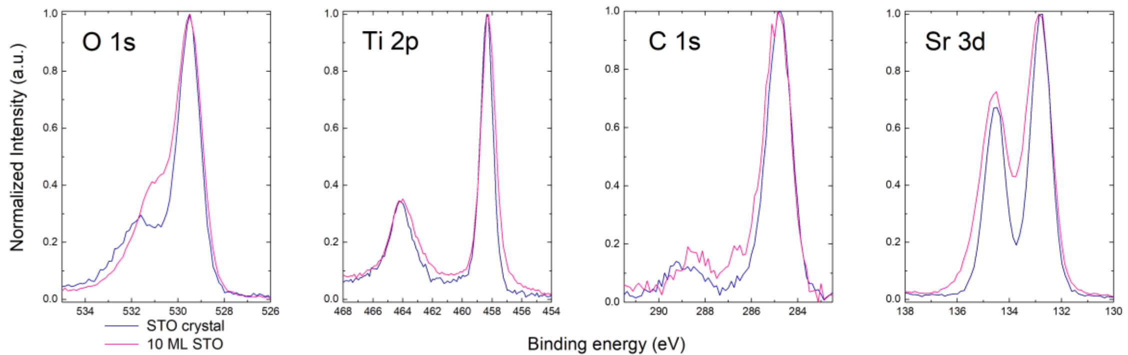

Figure 45: XPS spectra of the O 1s, Ti 2p, C 1s and Sr 3d regions of sample $S_{CY,4}$.

The spectra from O 1s, Ti 2p and Sr 3d regions exhibit the expected STO contributions (529.5 eV, 458.3 eV, and 132.9 eV, respectively). However, some differences between the spectra for the STO film and the single crystal can be observed: (i) in the O 1s region at ~531.1 eV, (ii) in the Sr 3d region at ~133.5 eV, and (iii) in the Ti 2p region at ~457 eV.

The additional double peak in the Sr 3d region can be assigned to surface $SrCO_3$ or to strontium silicates at the STO-Si interface. Since some formation of $SrCO_3$ is expected, both at the surfaces of the STO film and the single crystal STO sample, it is more likely that this contribution is related to silicates, as is the extra peak in the O 1s region.

The extra peak in the Ti 2p region can be assigned to Ti^{3+} oxidation states related to oxygen vacancies [143]. To assess the chemical composition of the STO thin film, fittings were performed in these main three regions as presented in Fig. 46. Only the peak area ratio related with the STO film was considered in the calculations. The relative concentrations of Sr, Ti and O in the STO film of sample $S_{CY,4}$ are about 23%, 20% and 57%, respectively. The composition of the STO film is close to stoichiometric, however slightly Ti and O deficient. It seems that the expansion of the unit cell volume observed by RSM can be mostly assigned to oxygen vacancies present in the STO film.

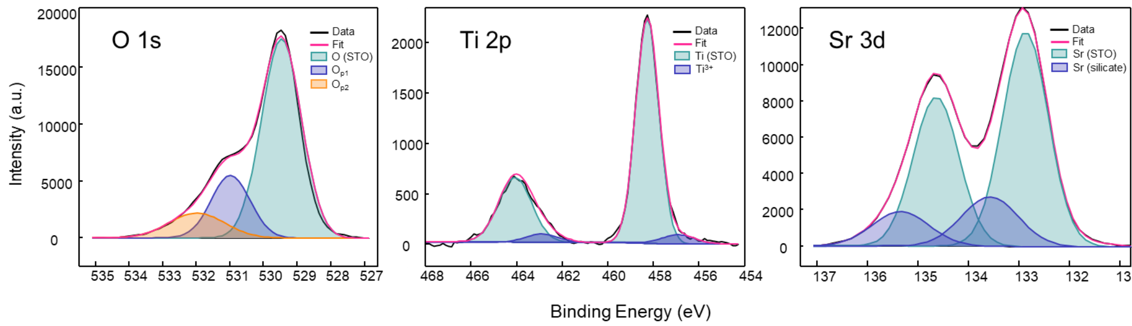

Figure 46: Fittings for O 1s, Ti 2p and Sr 3d spectra for sample $S_{CY,4}$.

The thicknesses of the STO film and the silicate layer, together with their densities, were explored by XRR using synchrotron light radiation with a photon energy of 20 keV. The XRR spectra and fittings are presented in Fig. 47. The same model was used for the fitting as presented in Subsection 6.2.2.1. In the model, there are two additional layers between the Si substrate and the STO film: a strontium silicate layer ($SrSiO_3$) and a Si layer with a slightly lower density than the bulk Si. The results of the fitting are presented in Table 13.

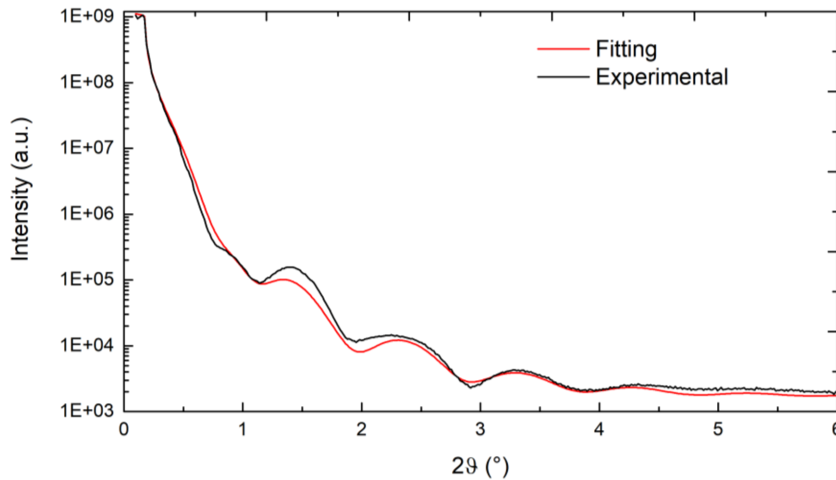

Figure 47: XRR data and fitting for sample $S_{CY,4}$. The analysis was performed using synchrotron radiation with a photon energy of 20 keV.

Table 13: Results of XRR analysis for sample $S_{CY,4}$.

Layer	Thickness (nm)	Density (g cm^{-3})
STO	3.7 ± 0.2	4.5 ± 0.3
Silicate ($SrSiO_3$)	1.9 ± 0.3	3.4 ± 0.4

The thickness of the STO layer (~3.7 nm) corresponds to about 9 ML of STO coverage, which is close to the value estimated at the beginning of the experiment (10 ML). The thickness of the silicate layer is ~1.9 nm, which is more than observed in sample $S_{TR,1}$. Samples $S_{TR,1}$ and $S_{CY,4}$ were prepared using the same growth parameters. There is a possibility that there were minor differences in sample preparation because the samples were prepared by different operators about a year apart. The repeatability of the STO film growth should be further explored. However, a direct comparison of these results should be done carefully because different X-ray sources were used during XRR measurements of the two samples. Sample $S_{TR,1}$ was analysed using a laboratory X-ray source, while synchrotron light (SL) was used during XRR analysis of sample $S_{CY,4}$. The use of SL results in a higher intensity, higher signal-to-noise ratio and angular resolution [86]. When comparing the XRR spectra, a large background can be observed at low angles close to the total reflection for sample $S_{TR,1}$, which may influence the data interpretation if not carefully removed before fitting. In the case sample $S_{CY,4}$, the background is much lower due to better collimation of the beam and a higher flux that results in better input data for the fittings.

6.3.2.3 Test of functional properties

STO is known to be an incipient ferroelectric in bulk but may become ferroelectric (FE) when in the form of a strained ultrathin film. Many theoretical and experimental studies have shown that it is possible to produce FE in STO ultra-thin films by inducing epitaxial strain [37], [144]–[148]. FE has been observed in ultrathin STO layers with film thickness < 20 ML by means of PFM [38]. As discovered by RSM, a small portion of the STO film in sample $S_{CY,4}$ exhibits a tetragonal unit cell, therefore we had reason to believe that FE properties could arise in this STO film. On the other hand, studies have shown that the STO film tends to relax if an amorphous silicate layer forms at the STO-Si interface [38]. Since a ~1.9 nm silicate interlayer is present in sample $S_{CY,4}$, the chances of detecting any FE properties were low.

To check for possible FE in the partially strained STO film, we used PFM, a technique that has demonstrated FE in films as thin as 2.8 nm [149], [150]. PFM measurements were performed on different parts of the sample. Fig. 48(a) and (b) show topography images of a representative part of the sample surface. Local electric fields were applied to the STO layer by means of a biased, conducting atomic force probe, and a potential piezoelectric response was subsequently imaged. The measurements were performed at RT. However, no piezoresponse, and therefore no FE, was detected, not in the vertical, nor in the lateral direction as presented in Fig. 48 (c) and (d), respectively. The signal recorded in these two figures is due to noise.

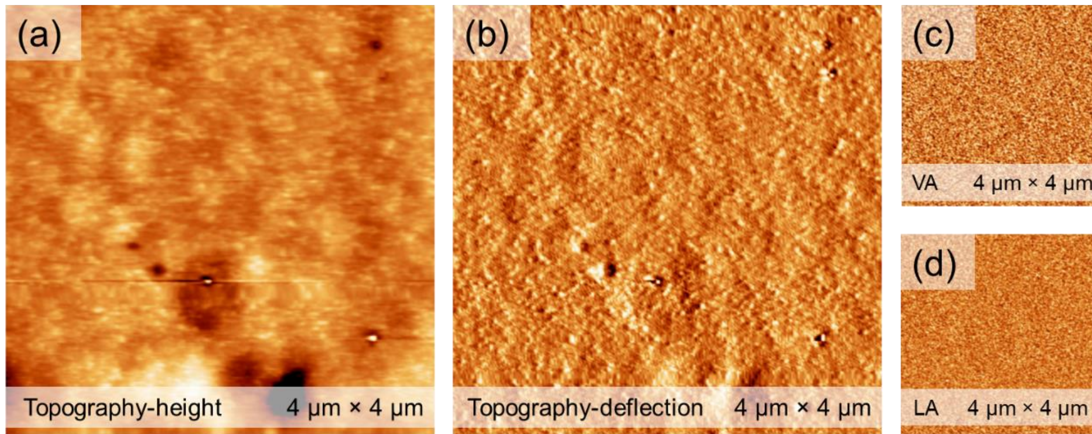

Figure 48: Results of PFM analysis of sample $S_{CY,4}$: (a) Topography-height image. (b) Topography-deflection image. (c) PFM mode – vertical amplitude. (d) PFM mode – lateral amplitude.

This is consistent with the RSM results which show that most of the STO film is relaxed. Warusawithana et al. [38] observed that the relaxation of the STO film due to silicate formation in thicker STO films can be related to the absence of FE in such STO films. The STO films in their study that exhibited FE showed signs of crystallinity at all steps of their growth, even right after the deposition of the first STO layers at a low temperature. On the contrary, the STO layers in our study are amorphous after their deposition and become crystalline only after the crystallization step. It seems that an amorphous initiation of the STO growth impedes the chances of obtaining a commensurately strained STO on Si(001). To obtain a sharp STO-Si interface, the PLD growth should be designed so that the crystallinity of the sample surface is preserved throughout the entire process of the STO growth.

6.3.2.4 Demonstration of the integration of functional oxides

The procedure for the PLD-growth of STO on Si presented in this work was used to prepare STO-Si pseudo-substrates that were then used for the integration of $(LaMnO_3/STO)x$ superlattices (SL) with Si in the work completed by Chen et al. [48]. The $(LaMnO_3/STO)x$ SL system is at the same time difficult to produce and very interesting because of its magnetic properties, which makes it a convenient case study of the integration of functional oxides with Si. In their work, (001) single-oriented SLs were integrated on Si using various template techniques, including a thin STO film prepared by PLD. They found that the SLs prepared on a PLD-grown STO-Si pseudo-substrate exhibit an epitaxial relationship with the Si substrate and a rocking curve FWHM of 2.66°. The magnetic properties in the SLs grown on STO-Si are well pronounced, however, modified by defects and strain compared to reference SLs grown on an STO single crystal.

6.4 Conclusions

The impact of four key parameters (coverage per crystallization, coverage per oxidation, crystallization procedure, and crystallization temperature) on the multi-staged growth of epitaxial ultra-thin STO layers on Si(001) by PLD has been explored. The main results and conclusions can be summarized as follows:

(1) The minimization of the thermal budget during the crystallization step increases the interface sharpness, although certain energy has to be supplied to the system in order to ensure an adequate density of the STO layer.

(2) A coverage of 2 ML before every crystallization step yields the best results in terms of the crystallization temperature, surface crystalline quality, and stoichiometry.

(3) The best results were obtained when the coverage per oxidation was as high as the optimal coverage per crystallization (2 ML).

These results are explained in terms of the necessary balance between critical thickness and crystallization energy minimization, and the need to ensure enough STO coverage of the buffer layer so any possible reactions during the oxidation phase are discarded.

An ultra-thin STO film was prepared using the optimized growth parameters. The structural analysis showed that the STO film grows along the (001) direction, rotated in-plane by 45° in respect to the Si lattice. In the crystalline STO film, portions with different values of lattice parameters are present. A small part of the STO film is compressed in-plane and expanded in the out-of-plane direction due to the strain induced by the STO-Si lattice mismatch. Most of the ~3.7 nm thick STO film is relaxed due to a ~1.9 nm thick silicate layer present at the STO-Si interface. That part of the film exhibits a cubic unit cell with a volume 2-5% larger than the bulk unit cell, while a smaller part of the film exhibits a tetragonal unit cell expanded in the in-plane direction with a volume up to 7% larger than the bulk unit cell volume. Presumably, this part has an a-domain STO structure due to tensile strain resulting from the thermal mismatch of STO and Si.

The expansion of the unit cell volume can be attributed to a slight non-stoichiometry of the STO film due to a small Ti and O-deficiency. The STO film was tested for FE properties, however, none were detected. The relaxation of the STO film due to the formation of the silicate interlayer prevents the emergence of FE properties.

The silicate interlayer starts to form at the STO-Si interface already after the deposition of the first 2 ML. The thickness of the silicate interlayer increases with every cycle of deposition, oxidation, and crystallization steps. According to research on MBE growth of STO on Si, an amorphous initiation of the STO growth hampers the chances of obtaining a commensurately strained STO film. To produce a sharp STO-Si interface, the PLD growth procedure should be designed so that the crystallinity of the sample surface can be maintained throughout the entire growth process. Even though the amorphization of the STO-Si interface cannot be completely avoided, ultra-thin films of STO on Si produced by PLD can still serve as an excellent template for the growth of thicker STO films in the production of STO-Si pseudo-substrates and integration with functional oxides, which has been demonstrated by research that followed the presented work.

Chapter 7

Summary and Conclusions

When growing thin films of STO on Si, an amorphous interlayer is often formed at the STO-Si interface, which limits the use of STO-Si pseudo-substrates in certain device applications. While this problem has been addressed for STO-Si pseudo-substrates prepared using the MBE method, the issue still remains to be answered when the PLD technique is used for the STO deposition.

In this thesis, several aspects concerning the PLD growth of epitaxial ultra-thin STO films on Sr-passivated Si substrates were considered. I gave particular attention to the identification of mechanisms that cause the formation and expansion of the amorphous interlayer at the STO-Si interface, which I systematically addressed by examining the surfaces and films formed during the main steps of the PLD-growth procedure. I studied in detail the surface morphology, atomic structure, and defects of the deoxidised Si(001) surface and the Sr-passivated Si(001) surface, followed by a thorough investigation of the crystal structure and chemical composition of ultra-thin STO films integrated on Sr-Si substrates and the STO-Si interface.

In the first step, I examined the surfaces of the deoxidised LD and HD Si substrates used in all the experiments presented in this work. I was mainly interested in the stability of deoxidized Si(001) surfaces at a pressure of ~ 1×10^{-8} mbar during a period of 5 min. Such surface exposure (~ 3 L), which is present before every Sr-passivation step performed in the JSI PLD system, cannot be avoided (without improving the base pressure in the deposition chamber), however, I showed that the Si(001) surface remains stable despite such exposure without any signs of amorphous silicate formations that might disturb the quality of the STO-Si interface during the STO film integration.

In the next part, the findings of a detailed analysis of a PLD-prepared Sr/Si(001)(2×1) surface, which serves as a template for the growth of STO thin films, are presented. Chemical analysis showed that the SiO_2 layer was completely removed from the Sr-Si surface while only a minor amount of silicates was formed after the passivation step. STM results demonstrated considerable differences in the surface morphology between deoxidised Si and the Sr-passivated Si surfaces, caused by a complete transfer of the topmost Si atoms towards step edges as ½ ML of Sr was deposited on a Si substrate at 700 °C using PLD. High-resolution STM images revealed an atomically ordered surface with (2×1) and (1×2) surface reconstructions alternating on neighbouring terraces and a 0.78 nm×0.39 nm large unit cell. In addition to some physisorbed contaminants, two types of surface defects were observed: (i) series of Sr vacancies and (ii) series of Sr adatoms, which were identified by comparing experimental STM images with calculated constant current images based on DFT calculations. It was discovered that compared to MBE-prepared surfaces, the Sr-Si surface prepared by PLD displays a higher defect density originating mainly from the high-energetic nature of the PLD deposition in vacuum.

Furthermore, we grew ultra-thin films of STO on a Sr-passivated Si substrate following a special multi-step procedure, where STO deposition, oxidation, and crystallization stages are performed separately in cycles until a film thickness of ~10 ML is reached. By varying some key deposition parameters (coverage per oxidation, coverage per crystallization, crystallization procedure, and crystallization temperature), we developed a protocol for STO integration on Si, taking into account the peculiarities of the PLD growth, STO critical thickness, and the process thermal budget, in order to kinetically trap the reactions between STO and Si and thus minimize the thickness of the interface layer while maintaining sufficient density of the STO layer. Together with the parameters determined by previous studies, the optimised parameters for the formation of the STO seed layer on Si using the PLD technique are:

(i) Sr deoxidation: 12 h degassing at 650 °C, followed by 60 s flashes at 1200 °C repeated 2-3 times.

(ii) Sr-passivation of the Si surface: deposition of 1/2 ML Sr in a background pressure $< 1\times10^{-8}$ mbar, fluence of 1 J cm^{-2}, frequency of 0.25 Hz, spot size of 0.14 mm^2, and a substrate temperature of 700 °C. This step should be executed within 5 min after Sr deoxidation.

(iii) Growth of ultra-thin STO film: fluence of 1.5 J cm^{-2}, frequency of 1 Hz, spot size of 0.58 mm^2, deposition of 2 ML of STO in an Ar atmosphere of 5×10^{-2} mbar at RT, followed by an exposure to 9×10^{-7} mbar of O_2 for 5 min at RT, and annealing for 15 min in a base pressure $< 1\times10^{-8}$ mbar at a temperature of 515 °C. This step is repeated until reaching a thickness of 10 ML.

The as-prepared oxide layer is single phase and exhibits STO(001)||Si(001) out-of-plane and STO[110]||Si[100] in-plane orientation. Most of the ~3.7 nm thick STO film is relaxed due to a ~1.2-1.9 nm thick silicate layer present at the STO-Si interface. That part of the film exhibits a cubic unit cell with a volume 2-5% larger than the bulk unit cell, while a smaller part of the film exhibits a tetragonal unit cell expanded in the in-plane direction with a volume up to 7% larger than the bulk unit cell volume. The expansion of the unit cell volume can be attributed to a slight non-stoichiometry of the STO film due to a small Ti and O-deficiency. The STO film was tested for FE properties, however, none were detected. The relaxation of the STO film due to the formation of the silicate interlayer prevents the emergence of FE properties.

In the final part, I studied the evolution of the STO-Si interface during the STO growth on Sr-Si substrates. The interlayer starts forming at the deposition of the first 2 ML of STO which are amorphous and expands by every deposition-oxidation-crystallization cycle reaching a thickness of 1.2 – 1.9 nm after the deposition of about 10 ML of STO. Compared to the thickness of the interlayer found in 50 nm thick PLD-grown STO films on Si (~2.5 nm), the majority of the interlayer develops during the formation of the first 10 ML of STO. Although amorphization of the STO-Si interface cannot be avoided completely, ultra-thin films of STO on Si produced by PLD can still be used as an excellent template for the growth of thicker STO films in the production of STO-Si pseudo-substrates and the epitaxial integration of various functional oxides with Si.

Additionally, a network of modified UHV equipment for sample preparation, transfer, and analysis under UHV conditions was established which enabled a large part of the research presented in this work and is now a part of the JSI research infrastructure.

In summary, the results presented in this thesis offer an insight into the capabilities and limitations of the PLD technique in the integration of ultra-thin STO films on Sr-passivated Si substrates with an atomically sharp STO-Si interface.

Appendix A

Sample Transfer Using a Vacuum Suitcase

A.1 Introduction

The simplest interface one can think of is that between a crystalline solid and vacuum. When vacuum is sufficiently high, one can neglect the influence of the gas phase and adsorbed contaminants [151]. At a pressure of approximately 1.3×10^{-6} mbar (1×10^{-6} Torr), the number of molecules necessary to complete 1 ML of adsorbates strikes the surface every second. The actual coverage depends on the sticking coefficient S, which is the probability that an impinging atom or molecule remains adsorbed. The unit Langmuir (L) is defined as the dosage corresponding to exposure of the surface for 1 s to a gas pressure of ~1.3×10^{-6} mbar, assuming S=1. In order to preserve the surface clean at least over a period of a few hours, it is, therefore, necessary to have a vacuum with residual gas pressure lower than 10^{-10} mbar.

UHV is required for most surface science experiments and is crucial for the preparation of atomically clean surfaces and preventing their contamination during their analysis especially when several methods are used. Nowadays, different deposition and analysis techniques are being combined in multi-chamber UHV systems that enable *in situ* transfer between the instruments. When such complex UHV systems are not available, ultra-thin films which are sensitive to ambient air are often covered by protective cap layers. Nevertheless, such overgrowth does not always present a suitable solution, as it may alter the physical properties of the original films [152], [153] nor is it applicable when a surface analysis is needed. On the other hand, individual instruments, spread within laboratories or even located at different institutions, can be used for the studies of the same sample without breaking vacuum by using a portable UHV chamber or a so-called "vacuum suitcase".

Several vacuum transfer systems have been developed and reported so far [154]–[158]. Special vacuum suitcases have been designed for specific applications, e.g. for neutron reflectometry under UHV [152], and for X-ray absorption fine structure spectroscopy at synchrotron facilities [159]. Presently, many UHV equipment manufacturers offer their own UHV transfer solutions [160].

In this appendix, a simple, portable vacuum suitcase will be described, used to transport samples between three separate UHV systems: PLD with RHEED, LT-STM with LEED and, XPS system. Furthermore, the adaptations to the host UHV systems needed to allow docking of the vacuum suitcase will be presented, together with a description of the transfer procedures. The appendix concludes with a presentation of the results of two tests of sample transfer.

A.1.1 The vacuum suitcase

We used a custom-designed vacuum suitcase (assembled by Specs) to transport samples freshly prepared in the PLD system to a combined LEED and LT STM system and a separate XPS system. The suitcase consists of 4 main parts: (i) a T-piece with standard CF40 flanges, (ii) a UHV gate valve, (iii) an ion pump (Gamma Vacuum, 35 l/s) that acts also as a pressure gauge, (iv) and a transfer rod with a special sample carrier as can be seen in Fig. 49(a). The ion pump can be connected to a controller unit and a battery power supply, which enables the operation of the pump during the transfer. This is especially important because it is known that an ion pump generates a pressure burst at every power-up, which can contaminate the samples. The magnetically coupled transfer rod has rotary (360°) and effective linear motion (up to 450 mm). The sample carrier attached to the end of the transfer rod can hold up to 6 flag style (Omicron type) sample plates in 2 rows by 3, which can be accessed by rotating the rod (Fig. 49(b)). Providing a bake-out of the suitcase, its base pressure can be as low as 9×10^{-11} mbar. The total weight of the suitcase including the controller and the battery is about 18 kg.

Some minor modifications were made to the original design of the vacuum suitcase. Across the opening leading to the ion pump, we added a mesh that protects the pump against accidental falls of material from samples or the sample plates. Additionally, to access all 6 sample stages, we spot-welded stainless steel ribbons at the ends of individual carrier stages. This prevents the sample plates from slipping out from the sample carrier during the rotation of the manipulator for 180°. To the end of the transfer rod, we added a lock screw to prevent any movements of the rod with the sample carrier during the transfer. Finally, we added some handles for carrying the suitcase.

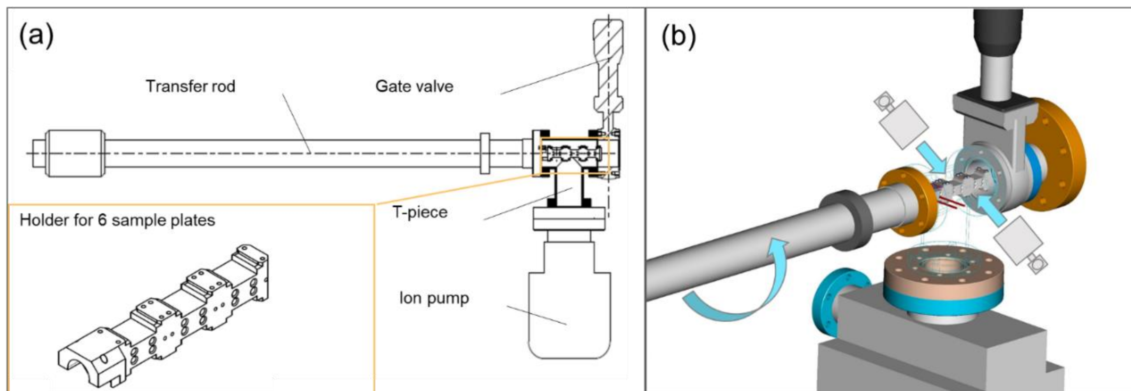

Figure 49: (a) Schematics of the vacuum suitcase. (b) The 3 sample plates (from total 6) can be inserted by rotating the transfer rod by 180°.

A.1.2 Modifications of host UHV systems

To use the (presented) vacuum suitcase, some adaptations of the host UHV systems are usually needed. The UHV docking chamber must be equipped with a CF40 flange and a connection to a turbopump that allows for fast pumping down to at least 5×10^{-9} mbar. If the UHV system is equipped with a load-lock (LL) with an extra port and a suitable transfer rod, it can be used as a dock for installing the vacuum suitcase. If not, a short CF40 T-piece with a gate valve has to be installed. Additional equipment is needed if the sample plates do not fit the analysis equipment and adapters need to be used. The vacuum suitcase must be properly aligned with the docking chamber. When high accuracy in positioning is not possible, it is advisable to install a metal bellow between the two parts

to allow small deviations from the optimal position. The weight of the suitcase must be supported by a suitable structure.

We established a suitcase connection with three UHV systems, located in three different laboratories in different buildings in the JSI area: (i) a PLD system at the Advanced Materials Department, K9, JSI, (ii) a LEED and LT STM system at Condensed Physics Department, F5, JSI, (iii) and an XPS system at the Department of Surface Engineering and Optoelectronics, F3, JSI.

For the PLD system, a T-piece with a viewport and two gate valves was attached to the storage chamber and connected to the LL turbopump on one side, as shown in Fig. 50(a) and 51(a). A short bellow was added between the T-piece and the vacuum suitcase. A special shelf was designed to support the suitcase's weight. Additionally, a protective stand, connecting the end of the transfer rod to the floor, was installed to prevent unwanted movements of the vacuum suitcase during the everyday PLD operation (Fig. 50(b)). Fig. 50(c) shows the PLD-suitcase connection during bake-out of the buffer volume.

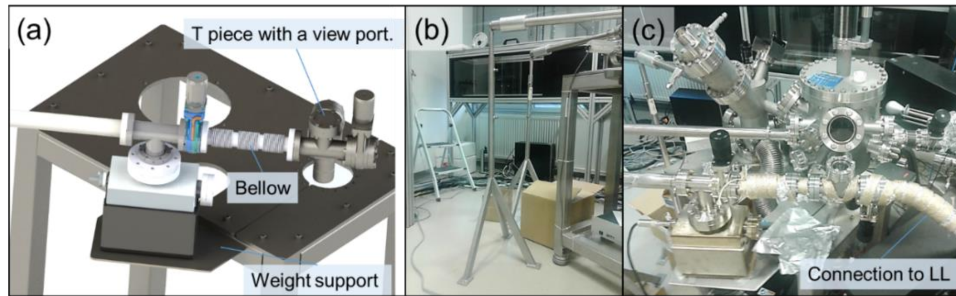

Figure 50: (a) Design of a docking station for the vacuum suitcase at the PLD system. (b) Protective stand. (c) Preparations for the bake-out of the buffer volume.

To establish a connection between the XPS system and the vacuum suitcase, we added an extra chamber that enables moving the sample plates into a special adapter that fits the XPS chamber. Therefore, a preparation chamber with many viewports, a transfer rod, and additional wobble sticks was attached to the XPS chamber as shown in Fig. 51(b) (see Chapter 3, Fig. 3). After adding a T-piece, a connection to the XPS LL, a bellow, and weight support, the XPS-suitcase connection was established.

The easiest solution was found for the STM-suitcase connection because the STM LL allowed a direct connection to the suitcase with the frame of the STM system acting also as weight support for the suitcase (Fig. 51(c)).

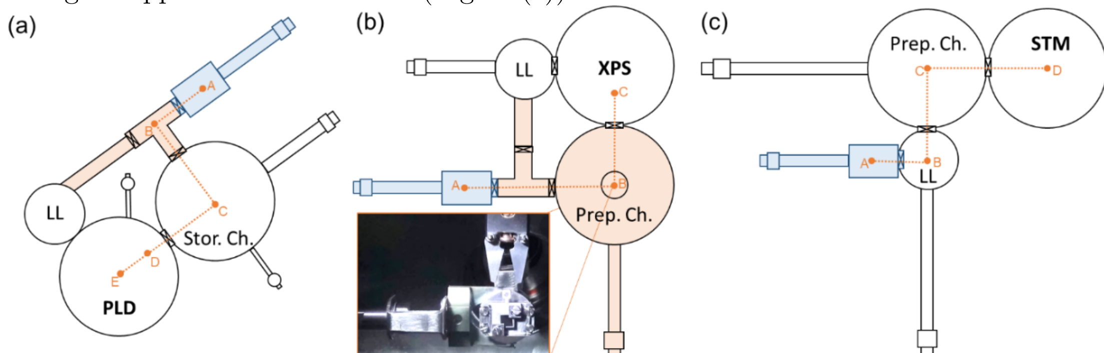

Figure 51: Schematics of different UHV system-vacuum suitcase connections with marked sample paths. The host UHV systems shown in the schematics are: (a) the PLD system, (b) the XPS system, and (c) the STM system. The vacuum suitcase is coloured blue and orange marks the vacuum equipment that was added to the existing UHV systems.

A.1.3 The sample transfer procedure

The basic procedure for sample transfer using the vacuum suitcase is the same for all 3 transfer options (PLD-STM, STM-XPS, PLD-XPS):

1) The suitcase is attached to a host UHV system A.
2) The docking chamber (LL or T-piece) is pumped using a turbopump connection.
3) A bake-out of the docking chamber is performed.
4) After reaching the desired pressure ($<5\times10^{-9}$ mbar), the samples are moved from the host vacuum system to the vacuum suitcase.
5) The docking chamber is vented with dry nitrogen and the suitcase is detached.
6) The suitcase is transferred and attached to the host UHV system B.
7) The docking chamber of the UHV system B is pumped and baked-out until an appropriate pressure is reached.
8) The samples are moved from the suitcase to the host UHV system.

The specific steps needed to move a sample from the presented vacuum systems to the vacuum suitcase are illustrated in Fig. 51. After a sample is prepared in the PLD chamber (site E in Fig. 51(a)), it is transferred to an acceptor stage (site D) by a wobble stick. From there, it is moved to a storage chamber by a transfer rod (to site C). Multiple samples can be stored in the storage chamber. From the storage chamber, the samples are transferred to the suitcase sample carrier (site B) by an additional wobble stick.

At the XPS system, the samples are inserted first into the preparation chamber by the suitcase transfer rod as shown in Fig. 51(b). A wobble stick located at the top of the preparation chamber is used to remove a sample plate from the suitcase sample carrier. The sample plate is then inserted into an XPS adapter fixed at the end of the transfer rod in the preparation chamber (inset in Fig. 51(b)). Finally, the adapter with the sample plate is moved inside the XPS chamber and inserted into the instrument. Up to 6 samples can be analysed at each suitcase transfer by exchanging the sample plates in the XPS adapter.

At the STM system, the sample plates are transferred from the suitcase to the STM LL using the suitcase transfer rod and a LL transfer rod with a flag style toggle end-effector and no special adapters are needed (Fig 51(c)). Because all movements inside the vacuum systems cause some outgassing, the valves must be opened and closed slowly, as should be the movements of the magnetic transfer rods.

A.2 Test of Sample Transfer

There are two steps of the sample transfer procedure using the vacuum suitcase during which the sample surface might get contaminated. The first one is immediately after the preparation of a sample in the PLD chamber and before its transfer to the storage chamber, due to a relatively high background pressure in the PLD chamber after performing deposition ($\sim1\times10^{-8}$ mbar). The second is during the bake-out of the docking chamber (LL or T-piece), which is needed to achieve UHV, after attaching the suitcase to a host UHV system. During the bake-out, the UHV gate valve separating the suitcase from the docking chamber can also heat up and cause an increase in the suitcase base pressure, which might contaminate the sample surface.

To determine the impact of the background gas on the surface cleanliness during these two steps, we performed two additional test experiments. For the first test, we took a sample with a clean Cu(111) surface from the STM chamber to the suitcase, performed a bake-out of the docking chamber, and transferred the sample back to the STM. In the second test, we took the Cu sample from the STM system to the PLD system using the

vacuum suitcase. At the PLD system, we inserted the sample into the deposition chamber for ~15 min in total and then returned the sample to the STM system using the vacuum suitcase. During the second test, the bake-out was performed twice, once per every docking. We performed STM analysis of the Cu surface at the beginning and the end of each of the two transfer tests.

A.2.1 Methods

A high-purity Cu(111) single-crystal substrate was cleaned in the STM preparation chamber under UHV (~5×10^{-10} mbar) by a thorough procedure of Ar-ion sputtering and annealing cycles. After STM analysis, the sample was moved from the STM system to the vacuum suitcase, readily attached to the STM system. After closing the gate valve to the suitcase, the LL was vented by nitrogen gas and the suitcase was detached, exposed to the atmospheric pressure, and then reattached. Heating tapes were wrapped around the LL chamber and the transfer arm. The LL volume was pumped down followed by a 3 h bake-out at 130 °C. During the bake-out, the pressure in the suitcase increased from 2×10^{-10} mbar to 2×10^{-9} mbar. After the LL was cooled below 50 °C, the sample was transferred from the suitcase back to the STM chamber, where we performed surface analysis. Between the first and the second STM analysis, the sample was exposed to ~16 L, disregarding the brief pressure increases produced by movements of the transfer rods and valves.

For the second test, the sample surface was cleaned again, inspected by STM, and moved back to the vacuum suitcase. Fig. 52 shows the surface exposure at every step of the sample transfer during this test. The suitcase was detached from the STM system and transferred to the PLD laboratory. After attaching the transfer chamber to the T-piece, the buffer volume was pumped and baked for 3 h at 130 °C using heating tapes. During the bake-out, the pressure in the suitcase was ~1.5×10^{-9} mbar. The surface exposure during the first bake-out was ~12 L. After cooling the T-piece, the sample was moved from the suitcase through the storage chamber to the PLD chamber with a base pressure of ~6×10^{-9} mbar, where it was left for 15 min (~4 L exposure). Then the sample was moved back to the vacuum suitcase and transferred to the STM system. An additional bake-out (3h, 130 °C, ~2×10^{-9} mbar in the suitcase) was performed after reattaching the suitcase to the STM LL. The sample was transferred to the STM chamber after the temperature of the LL was decreased below 50 °C. During the second bake-out, the Cu surface was exposed to ~16 L. The exposure during the rest of the transfer steps is negligible compared to surface exposure during the bake-outs and the sample exposure to the residual atmosphere in the PLD chamber.

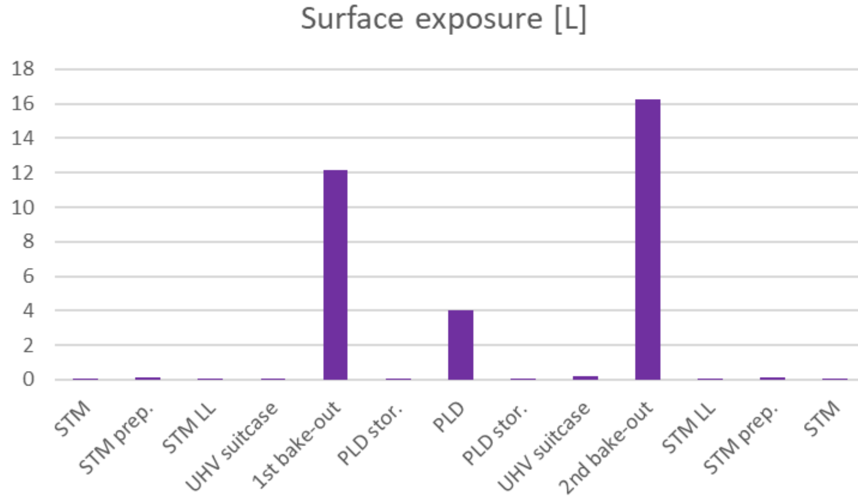

Figure 52: A chart showing the Cu(111) surface exposure at every step performed during the 2nd transfer test from the STM system to the PLD system and back using the vacuum suitcase.

A.2.2 Results and discussion

The Cu(111) surface was first inspected by STM at ~4 K after performing the standard cleaning procedure. Fig. 53(a) shows terraces of different sizes separated by monoatomic steps. In Fig. 53(b), a few surface defects typical for the Cu(111) surface can be observed. The dark spots represent adsorbates, most likely CO molecules and the circles surrounding the adsorbates can be attributed to standing waves produced by scattering of the Cu(111) surface state electrons at the adsorbate sites [161]. STM image in Fig. 53(c) shows the Cu(111) surface after performing the sample transfer from the STM to the vacuum suitcase and back and performing one bake-out in the process. The density of surface defects increased from ~10 per 250 nm^2 to ~40 per 250 nm^2 after the first test.

The Cu(111) surface was cleaned again and inspected by STM. The STM images resembled the images presented in Fig. 53(a) and (b). After transferring the sample to the PLD system and back, and performing two bake-outs in the process, the Cu surface was again inspected by STM. Fig. 53(d) shows terraces covered with different types of adsorbates. The majority of adsorbates are ordered in chains that are oriented in the main crystal directions corresponding to the hexagonal crystal lattice of the Cu(111) surface. Some of these chains are quite long. The high-resolution STM image in Fig. 53(e) shows a part of a chain in higher resolution. Note that during the formation of the presented image the STM tip had a double apex, as was found later. After applying a bias pulse to the tip on a clean Cu surface, the tip apex changed (see inset in Fig. 53(e)).

CO molecules do not usually arrange in rows on the Cu(111) surface [161]. It appears that different species are present at the surface. Similar chain-like structures have been observed on a Cu(110) surface. In the study by Shi, the adsorbates were identified as water molecules [162]. It is very likely that the water partial pressure is higher in the PLD chamber than in other parts of the vacuum equipment used during the testing. We know that cold spots that retain water vapour are formed in the deposition chamber due to uneven heating and cooling of the PLD system during the bake-out performed using heating tapes. Thus, we believe that water was adsorbed during the sample exposure to the PLD chamber.

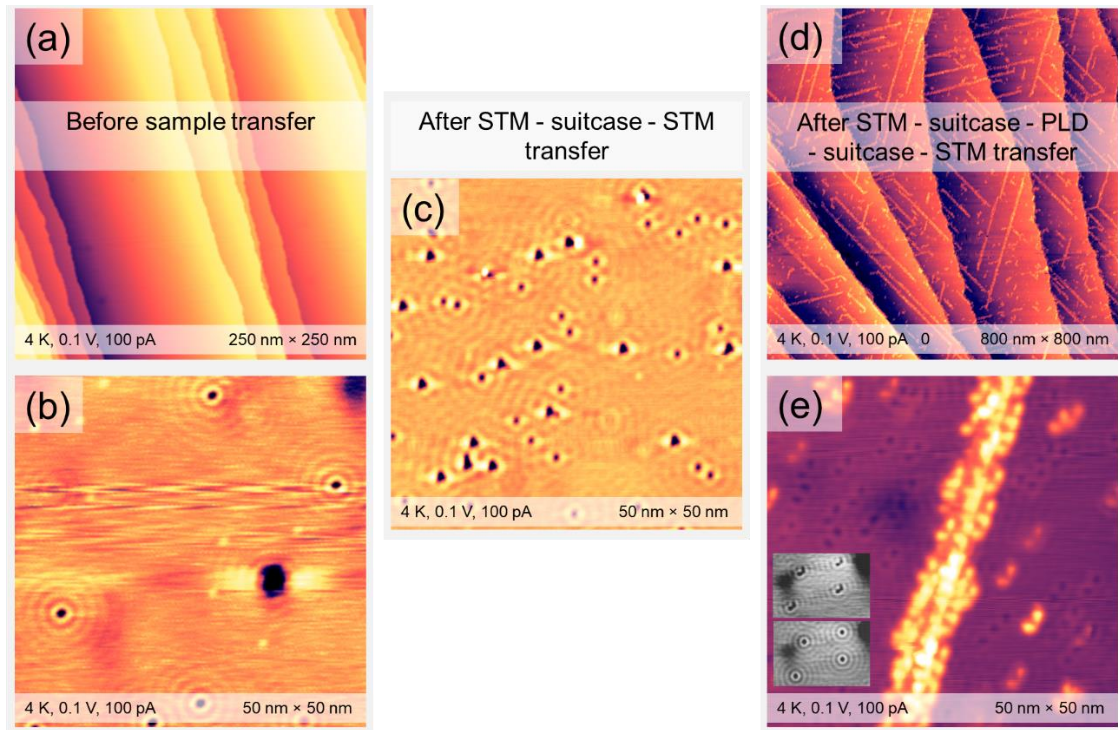

Figure 53: Results of STM analysis. (a) and (b) STM images of Cu(111) surface after cleaning. (c) STM image of the Cu(111) surface after the 1st transfer test. (d) and (e) STM images of the Cu(111) surface after the 2nd transfer test. The two insets in (e) show a transition from a double to a single apex STM tip after applying a bias pulse.

A.3 Conclusions

We established a network for sample transfer under UHV conditions between three separate vacuum systems. Using a vacuum suitcase, it is now possible to transfer samples between the PLD, LEED-STM, and the XPS systems located at JSI. At every sample transfer, a bake-out of the docking chamber is performed to decrease the pressure in the chamber before moving samples from the suitcase to a host UHV system. At every bake-out, the samples are exposed to about 12-16 L of residual atmosphere.

We performed two tests of sample transfer using a Cu(111) monocrystal. According to the results of STM analysis before and after the 1st transfer test (STM-suitcase-STM) we can conclude that the bake-out of a docking chamber causes an increase of the Cu surface defect density by a factor of ~4. After the surface was exposed to the PLD chamber (~4 L) and 2 bake-outs (~28 L), the defect density was increased even more. Apart from the typical CO adsorbates, an additional type of adsorbates arranging in chains was observed on the Cu surface, for which we assume to be water molecules. While additional CO molecules were probably adsorbed during the bake-outs, the source of water molecules is most likely the PLD chamber, because water vapour could be retained in the deposition chamber due to uneven bake-outs of the PLD system.

The sample transfer procedure could be improved in many ways:

1.) The transfer procedure is very time-consuming. Most of the time is spent performing bake-outs of the docking chambers. At the same time, bake-outs contribute the largest share to the total surface exposure (assuming an integer sticking coefficient). The bake-out of the docking T-piece at the PLD system could be avoided by attaching a turbopump directly to the T-piece instead of using the long connection to the turbopump and by venting the T-piece with N_2 the entire time it is exposed to atmosphere. The partial pressure of water vapour otherwise decreased by bake-outs could also be lowered by using liquid-nitrogen cold traps in the docking chambers.

2.) The base pressure in the PLD system should be decreased. Although the sample exposure is lower during its time in the PLD chamber than during a bake-out, it appears that water is adsorbed on the surface in the first case. In the case of clean Si surfaces, however, all oxygen-containing species pose a major problem. The base pressure in the PLD deposition chamber could be further decreased by replacing all vacuum parts with non-metal sealing, while the use of a bake-out tent would enable a more uniform warm-up and cooling of the entire PLD vacuum system.

3.) The weight and compactness of the suitcase could be decreased by replacing the ion-pump with a non-evaporable getter pump, which would offer also other advantages: no need for continuous power supply, no electric or magnetic field, high pumping speed, and pressures as low as 3×10^{-11} mbar [158].

Appendix B

STM of 2 ML STO on Si

An additional sample with a 2 ML STO film on the Sr-passivated Si surface was prepared by PLD (Fig. 54). The RHEED analysis of the sample surface after the crystallization step showed a diffuse pattern indicating an amorphous surface (Fig. 54(b)). The sample was transferred using the vacuum suitcase to the STM system. STM analysis showed that the film surface exhibits grain-like features with size ranging from 2 to 5 nm, and is generally very smooth (RSM = 0.16 nm), as presented in Fig. 54 (c) and (d). What is surprising is that the steps of the underlying Sr-Si surface cannot be recognized. The surface is amorphous; no periodic structures can be observed.

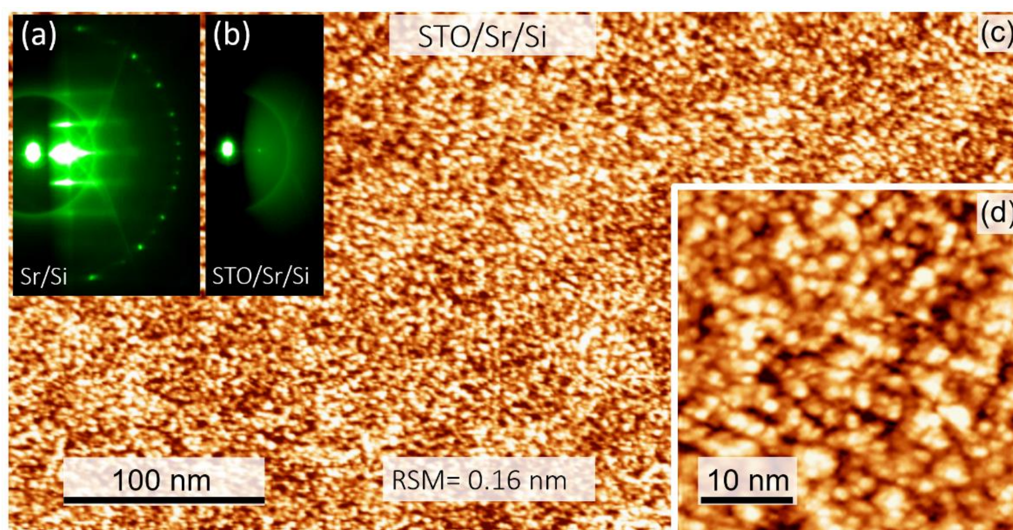

Figure 54: (a) RHEED of the Sr-passivated Si surface exhibiting the (1×2) + (2×1) surface reconstruction. (b) RHEED pattern after the deposition of a 2 ML of STO. (c) Large scale STM image of the STO film surface. (d) A magnification of a part of the STO film surface.

References

[1] M. Coll *et al.*, “Towards Oxide Electronics: a Roadmap,” *Appl. Surf. Sci.*, vol. 482, pp. 1–93, Jul. 2019.

[2] M. Lorenz *et al.*, “The 2016 oxide electronic materials and oxide interfaces roadmap,” *J. Phys. D. Appl. Phys.*, vol. 49, no. 43, p. 433001, Nov. 2016.

[3] H. Frey and H. R. Khan, *Handbook of Thin-Film Technology*. Springer Berlin Heidelberg, 2015.

[4] D. W. Pashley, “Epitaxy growth mechanisms,” *Mater. Sci. Technol.*, vol. 15, no. 1, pp. 2–8, 1999.

[5] H. Y. Hwang, Y. Iwasa, M. Kawasaki, B. Keimer, N. Nagaosa, and Y. Tokura, “Emergent phenomena at oxide interfaces,” *Nature Materials*, vol. 11, no. 2. Nature Publishing Group, pp. 103–113, 24-Jan-2012.

[6] F. Sánchez, C. Ocal, and J. Fontcuberta, “Tailored surfaces of perovskite oxide substrates for conducted growth of thin films,” *Chemical Society Reviews*, vol. 43, no. 7. Royal Society of Chemistry, pp. 2272–2285, 07-Apr-2014.

[7] D. P. Kumah, J. H. Ngai, and L. Kornblum, “Epitaxial Oxides on Semiconductors: From Fundamentals to New Devices,” *Adv. Funct. Mater.*, vol. 1901597, pp. 1–37, Jul. 2019.

[8] A. A. Demkov and A. B. Posadas, *Integration of Functional Oxides with Semiconductors*. Springer New York, 2014.

[9] J. W. Reiner *et al.*, “Crystalline Oxides on Silicon,” *Adv. Mater.*, vol. 22, no. 26–27, pp. 2919–2938, Apr. 2010.

[10] D. S. Aidhy, B. Liu, Y. Zhang, and W. J. Weber, “Chemical expansion affected oxygen vacancy stability in different oxide structures from first principles calculations,” *Comput. Mater. Sci.*, vol. 99, pp. 298–305, Mar. 2015.

[11] P. De Coux *et al.*, “Epitaxial ferromagnetic oxide thin films on silicon with atomically sharp interfaces,” *Appl. Phys. Lett.*, vol. 105, no. 1, p. 012401, Jul. 2014.

[12] H. N. Lee, D. Hesse, N. Zakharov, and U. Gösele, “Ferroelectric Bi3.25La0.75Ti3o12 films of uniform a-axis orientation on silicon substrates,” *Science (80-.).*, vol. 296, no. 5575, pp. 2006–2009, Jun. 2002.

[13] M. Scigaj *et al.*, “Ultra-flat BaTiO3 epitaxial films on Si(001) with large out-of-plane polarization,” *Appl. Phys. Lett.*, vol. 102, no. 11, p. 112905, Mar. 2013.

[14] S. Abel *et al.*, “A strong electro-optically active lead-free ferroelectric integrated on silicon,” *Nat. Commun.*, vol. 4, p. 1671, 2013.

[15] C. Dubourdieu *et al.*, “Switching of ferroelectric polarization in epitaxial BaTiO3 films on silicon without a conducting bottom electrode,” *Nat. Nanotechnol.*, vol. 8,

no. 10, 2013.
[16] S. H. Baek *et al.*, “Giant Piezoelectricity on Si for Hyperactive MEMS,” *Science (80-.).*, vol. 334, no. 6058, pp. 958–961, 2011.
[17] P. Perna, L. Méchin, M. P. Chauvat, P. Ruterana, C. Simon, and U. Scotti Di Uccio, “High Curie temperature for La0.7Sr0.3MnO3 thin films deposited on CeO2 /YSZ-based buffered silicon substrates,” *J. Phys. Condens. Matter*, vol. 21, no. 30, p. 306005, Jul. 2009.
[18] R. Bachelet, P. De Coux, B. Warot-Fonrose, V. Skumryev, J. Fontcuberta, and F. Sánchez, “CoFe2O4/buffer layer ultrathin heterostructures on Si(001),” *J. Appl. Phys.*, vol. 110, no. 8, p. 086102, Oct. 2011.
[19] J. W. Park *et al.*, “Creation of a two-dimensional electron gas at an oxide interface on silicon,” *Nat. Commun.*, vol. 1, no. 7, 2010.
[20] E. G. Keim, L. Wolterbeek, and A. Van Silfhout, “Adsorption of atomic oxygen (N2O) on a clean Si(100) surface and its influence on the surface state density; A comparison with O2,” *Surf. Sci.*, vol. 180, no. 2–3, pp. 565–598, Feb. 1987.
[21] T. Parkelj Potočnik *et al.*, “Atomic structure of Sr/Si(0 0 1)(1 $\times$ 2) surfaces prepared by Pulsed laser deposition,” *Appl. Surf. Sci.*, vol. 471, pp. 664–669, Mar. 2019.
[22] D. V. Averyanov *et al.*, “Atomic-Scale Engineering of Abrupt Interface for Direct Spin Contact of Ferromagnetic Semiconductor with Silicon,” *Sci. Rep.*, vol. 6, no. 1, pp. 1–9, Mar. 2016.
[23] C. Merckling *et al.*, “Pseudomorphic molecular beam epitaxy growth of γ- Al 2O3(001) on Si(001) and evidence for spontaneous lattice reorientation during epitaxy,” *Appl. Phys. Lett.*, vol. 89, no. 23, p. 232907, Dec. 2006.
[24] S. Guha, N. A. Bojarczuk, and V. Narayanan, “Lattice-matched, epitaxial, silicon-insulating lanthanum yttrium oxide heterostructures,” *Appl. Phys. Lett.*, vol. 80, no. 5, pp. 766–768, Feb. 2002.
[25] D. O. Klenov, L. F. Edge, D. G. Schlom, and S. Stemmer, “Extended defects in epitaxial Sc2 O3 films grown on (111) Si,” *Appl. Phys. Lett.*, vol. 86, no. 5, pp. 1–3, Jan. 2005.
[26] D. V. Averyanov *et al.*, “Direct epitaxial integration of the ferromagnetic semiconductor EuO with Si(1 1 1),” *J. Magn. Magn. Mater.*, vol. 459, pp. 136–140, Aug. 2018.
[27] M. P. Warusawithana *et al.*, “A ferroelectric Oxide Made Directly on Silicon,” *Science (80-.).*, no. 16, pp. 15–18, 2008.
[28] R. A. McKee, F. J. Walker, and M. F. Chisholm, “Crystalline Oxides on Silicon: The First Five Monolayers,” *Phys. Rev. Lett.*, vol. 81, no. 14, pp. 3014–3017, 1998.
[29] J. Lettieri, J. H. Haeni, and D. G. Schlom, “Critical issues in the heteroepitaxial growth of alkaline-earth oxides on silicon,” *J. Vac. Sci. Technol. A Vacuum, Surfaces, Film.*, vol. 20, no. 4, pp. 1332–1340, 2002.
[30] Y. Wei *et al.*, “Mechanism of cleaning Si(100) surface using Sr or SrO for the growth of crystalline SrTiO[sub 3] films,” *J. Vac. Sci. Technol. B Microelectron. Nanom. Struct.*, vol. 20, no. 4, p. 1402, Aug. 2002.
[31] F. Niu and B. W. Wessels, “Surface and interfacial structure of epitaxial SrTiO3 thin films on (001) Si grown by molecular beam epitaxy,” *J. Cryst. Growth*, vol.

300, no. 2, pp. 509–518, Mar. 2007.

[32] G. Delhaye *et al.*, "Structural properties of epitaxial SrTiO3 thin films grown by molecular beam epitaxy on Si(001)," *J. Appl. Phys.*, vol. 100, no. 12, p. 124109, Dec. 2006.

[33] M. Choi *et al.*, "Strain relaxation in single crystal SrTiO 3 grown on Si (001) by molecular beam epitaxy," *J. Appl. Phys.*, vol. 111, no. 6, pp. 1–8, 2012.

[34] J. Robertson and R. M. Wallace, "High-K materials and metal gates for CMOS applications," *Materials Science and Engineering R: Reports*, vol. 88. Elsevier Ltd, pp. 1–41, 01-Feb-2015.

[35] D. Klement, *Growth of Strontium Titanate on Silicon By Pulsed Laser Deposition Technique*. 2015.

[36] K. Nomura, H. Ohta, K. Ueda, T. Kamiya, M. Hirano, and H. Hosono, "Thin-film transistor fabricated in single-crystalline transparent oxide semiconductor," *Science (80-.).*, vol. 300, no. 5623, pp. 1269–1272, May 2003.

[37] A. Antons, J. B. Neaton, K. M. Rabe, and D. Vanderbilt, "Tunability of the dielectric response of epitaxially strained SrTiO 3 from first principles," *Phys. Rev. B - Condens. Matter Mater. Phys.*, vol. 71, no. 2, p. 024102, Jan. 2005.

[38] M. P. Warusawithana *et al.*, "A ferroelectric oxide made directly on silicon," *Science (80-.).*, vol. 324, no. 5925, pp. 367–370, Apr. 2009.

[39] O. Khaselev and J. A. Turner, "A monolithic photovoltaic-photoelectrochemical device for hydrogen production via water splitting," *Science (80-.).*, vol. 280, no. 5362, pp. 425–427, Apr. 1998.

[40] L. Ji *et al.*, "A silicon-based photocathode for water reduction with an epitaxial SrTiO3 protection layer and a nanostructured catalyst," *Nat. Nanotechnol.*, vol. 10, no. 1, pp. 84–90, Jan. 2015.

[41] X. Gu *et al.*, "Growth, characterization, and uniformity analysis of 200 mm wafer-scale SrTiO3/Si," *J. Vac. Sci. Technol. B, Nanotechnol. Microelectron. Mater. Process. Meas. Phenom.*, vol. 28, no. 3, p. C3A12-C3A16, May 2010.

[42] M. D. McDaniel, T. Q. Ngo, S. Hu, A. Posadas, A. A. Demkov, and J. G. Ekerdt, "Atomic layer deposition of perovskite oxides and their epitaxial integration with Si, Ge, and other semiconductors," *Appl. Phys. Rev.*, vol. 2, no. 4, p. 041301, Dec. 2015.

[43] C. B. Zhang, L. Wielunski, and B. G. Willis, "Formation of strontium template on Si(1 0 0) by atomic layer deposition," *Appl. Surf. Sci.*, vol. 257, no. 11, pp. 4826–4830, Mar. 2011.

[44] N. Pryds, B. Toftmann, J. B. Bilde-Sørensen, J. Schou, and S. Linderoth, "Thickness determination of large-area films of yttria-stabilized zirconia produced by pulsed laser deposition," *Appl. Surf. Sci.*, vol. 252, no. 13 SPEC. ISS., pp. 4882–4885, Apr. 2006.

[45] D. H. A. A. Blank, M. Dekkers, and G. Rijnders, "Pulsed laser deposition in Twente: From research tool towards industrial deposition," *J. Phys. D. Appl. Phys.*, vol. 47, no. 3, p. 034006, Jan. 2014.

[46] H. M. Christen and G. Eres, "Recent advances in pulsed-laser deposition of complex oxides," *J. Phys. Condens. Matter*, vol. 20, no. 26, p. 264005, Jul. 2008.

[47] D. Oka and T. Fukumura, "Crystal engineering for novel functionalities with oxide thin film epitaxy," *CrystEngComm*, vol. 19, no. 16. Royal Society of Chemistry, pp. 2144–2162, 19-Apr-2017.

[48] B. Chen *et al.*, "Integration of Single Oriented Oxide Superlattices on Silicon Using Various Template Techniques," *ACS Appl. Mater. Interfaces*, vol. 12, no. 38, pp. 42925–42932, Sep. 2020.

[49] R. Guo *et al.*, "Functional ferroelectric tunnel junctions on silicon," *Sci. Rep.*, vol. 5, no. 1, p. 12576, 2015.

[50] G. Niu *et al.*, "Epitaxy of BaTiO3 thin film on Si(001) using a SrTiO3 buffer layer for non-volatile memory application," *Microelectron. Eng.*, vol. 88, no. 7, pp. 1232–1235, 2011.

[51] M. Spreitzer, R. Egoavil, J. Verbeeck, D. H. A. Blank, and G. Rijnders, "Pulsed laser deposition of SrTiO3 on a H-terminated Si substrate," *J. Mater. Chem. C*, vol. 1, no. 34, pp. 5216–5222, Sep. 2013.

[52] X. Y. Zhou *et al.*, "Epitaxial growth of SrTiO3 thin film on Si by laser molecular beam epitaxy," *Appl. Phys. Lett.*, vol. 90, no. 1, p. 012902, Jan. 2007.

[53] X. Y. ZHOU *et al.*, "INFLUENCE OF PROCESSING CONDITIONS ON THE STRUCTURE OF STRONTIUM TITANATE THIN FILMS GROWN ON SI BY LASER MBE," *Integr. Ferroelectr.*, vol. 86, no. 1, pp. 109–116, Jan. 2006.

[54] M. Spreitzer *et al.*, "Growth mechanism of epitaxial SrTiO 3 on a (1 × 2) + (2 × 1) reconstructed Sr(1/2 ML)/Si(001) surface," *J. Mater. Chem. C*, vol. 8, no. 2, pp. 518–527, 2020.

[55] D. B. Chrisey and G. K. Hubler, *Pulsed laser deposition of thin films*. J. Wiley, 1994.

[56] D. Dijkkamp *et al.*, "Preparation of Y-Ba-Cu oxide superconductor thin films using pulsed laser evaporation from high Tc bulk material," *Appl. Phys. Lett.*, vol. 51, no. 8, pp. 619–621, Aug. 1987.

[57] J. A. Greer, "History and current status of commercial pulsed laser deposition equipment," *J. Phys. D. Appl. Phys.*, vol. 47, no. 3, p. 034005, Jan. 2014.

[58] V. A. Ukraintsev and J. T. Yates, "The role of nickel in Si(001) roughening," *Surf. Sci.*, vol. 346, no. 1–3, pp. 31–39, 1996.

[59] K. Hata, T. Kimura, S. Ozawa, and H. Shigekawa, "How to fabricate a defect free Si(001) surface," *J. Vac. Sci. Technol. A Vacuum, Surfaces, Film.*, vol. 18, no. 4, pp. 1933–1936, Jul. 2000.

[60] H.-J. Güntherodt and R. Wiesendanger, *Scanning Tunneling Microscopy I : General Principles and Applications to Clean and Adsorbate-Covered Surfaces*. Springer Berlin Heidelberg, 1992.

[61] M. S. Hoogeman *et al.*, "Design and performance of a programmable-temperature scanning tunneling microscope," *Rev. Sci. Instrum.*, vol. 69, no. 5, pp. 2072–2080, May 1998.

[62] N. Nilius, "Properties of oxide thin films and their adsorption behavior studied by scanning tunneling microscopy and conductance spectroscopy," *Surf. Sci. Rep.*, vol. 64, no. 12, pp. 595–659, Dec. 2009.

[63] J. Bardeen, "Tunnelling from a many-particle point of view," *Phys. Rev. Lett.*, vol.

6, no. 2, pp. 57–59, Jan. 1961.

[64] J. Tersoff and D. R. Hamann, "Theory and application for the scanning tunneling microscope," *Phys. Rev. Lett.*, vol. 50, no. 25, pp. 1998–2001, Jun. 1983.

[65] J. Tersoff and D. R. Hamann, "Theory of the scanning tunneling microscope," *Phys. Rev. B*, vol. 31, no. 2, pp. 805–813, Jan. 1985.

[66] H. Neddermeyer, "Scanning tunnelling microscopy of semiconductor surfaces," *Reports Prog. Phys.*, vol. 59, no. 6, pp. 701–769, Jun. 1996.

[67] F. J. Morin and J. P. Maita, "Electrical properties of silicon containing arsenic and boron," *Phys. Rev.*, vol. 96, no. 1, pp. 28–35, Oct. 1954.

[68] D. S. Sholl and J. A. Steckel, *Density functional theory : a practical introduction.* Wiley, 2009.

[69] D. E. P. Vanpoucke and G. Brocks, "Formation of Pt-induced Ge atomic nanowires on Pt/Ge(001): A density functional theory study," *Phys. Rev. B*, vol. 77, no. 24, p. 241308, Jun. 2008.

[70] I. Horcas, R. Fernández, J. M. Gómez-Rodríguez, J. Colchero, J. Gómez-Herrero, and A. M. Baro, "WSXM : A software for scanning probe microscopy and a tool for nanotechnology," *Rev. Sci. Instrum.*, vol. 78, no. 1, p. 013705, Jan. 2007.

[71] P. Hohenberg and W. Kohn, "Inhomogeneous Electron Gas," *Phys. Rev.*, vol. 136, no. 3B, pp. B864–B871, Nov. 1964.

[72] W. Kohn and L. J. Sham, "Self-Consistent Equations Including Exchange and Correlation Effects," *Phys. Rev.*, vol. 140, no. 4A, pp. A1133–A1138, Nov. 1965.

[73] P. E. Blöchl, "Projector augmented-wave method," *Phys. Rev. B*, vol. 50, no. 24, pp. 17953–17979, Dec. 1994.

[74] G. Kresse and J. Furthmüller, "Efficiency of ab-initio total energy calculations for metals and semiconductors using a plane-wave basis set," *Comput. Mater. Sci.*, vol. 6, no. 1, pp. 15–50, Jul. 1996.

[75] J. P. Perdew *et al.*, "Restoring the Density-Gradient Expansion for Exchange in Solids and Surfaces," *Phys. Rev. Lett.*, vol. 100, no. 13, p. 136406, Apr. 2008.

[76] J. Wang *et al.*, "Bonding and diffusion of Ba on a Si(001) reconstructed surface," *Phys. Rev. B*, vol. 60, no. 7, pp. 4968–4971, Aug. 1999.

[77] C. J. Först, C. R. Ashman, K. Schwarz, and P. E. Blöchl, "The interface between silicon and a high-k oxide," *Nature*, vol. 427, no. 6969, pp. 53–56, Jan. 2004.

[78] C. R. Ashman, C. J. Först, K. Schwarz, and P. E. Blöchl, "First-principles calculations of strontium on Si(001)," *Phys. Rev. B*, vol. 69, no. 7, p. 075309, 2004.

[79] G. Binnig, C. F. Quate, and C. Gerber, "Atomic force microscope," *Phys. Rev. Lett.*, vol. 56, no. 9, pp. 930–933, Mar. 1986.

[80] G. Haugstad, *Atomic Force Microscopy: Understanding Basic Modes and Advanced Applications.* Hoboken, NJ, USA: John Wiley and Sons, 2012.

[81] H. Uršič and U. Prah, "Investigations of ferroelectric polycrystalline bulks and thick films using piezoresponse force microscopy," *Proceedings of the Royal Society A: Mathematical, Physical and Engineering Sciences*, vol. 475, no. 2223. 2019.

[82] C. R. Brundle, C. A. Evans Jr., and S. Wilson, *Encyclopedia of Materials Characterization.* Elsevier, 1992.

[83] A. A. Bunaciu, E. gabriela Udriştioiu, and H. Y. Aboul-Enein, "X-Ray Diffraction:

Instrumentation and Applications," *Crit. Rev. Anal. Chem.*, vol. 45, no. 4, pp. 289–299, Oct. 2015.

[84] V. Holý, U. Pietsch, and T. Baumbach, *High-Resolution X-Ray Scattering from Thin Films and Multilayers.* Springer, 1999.

[85] R. Feidenhans'l, "Surface structure determination by X-ray diffraction," *Surf. Sci. Rep.*, vol. 10, no. 3, pp. 105–188, May 1989.

[86] G. Renaud, "Oxide surfaces and metal/oxide interfaces studied by grazing incidence X-ray scattering," *Surf. Sci. Rep.*, vol. 32, no. 1–6, pp. 5–90, Jan. 1998.

[87] J. Rubio-Zuazo, P. Ferrer, A. López, A. Gutiérrez-León, I. Da Silva, and G. R. Castro, "The multipurpose X-ray diffraction end-station of the BM25B-SpLine synchrotron beamline at the ESRF," *Nucl. Instruments Methods Phys. Res. Sect. A Accel. Spectrometers, Detect. Assoc. Equip.*, vol. 716, pp. 23–28, Jul. 2013.

[88] W. H. Press, S. a Teukolsky, W. T. Vetterling, and B. P. Flannery, *Numerical Recipes 3rd Edition: The Art of Scientific Computing*, vol. 1. 2007.

[89] M. Björck and G. Andersson, "GenX: An extensible X-ray reflectivity refinement program utilizing differential evolution," *J. Appl. Crystallogr.*, vol. 40, no. 6, pp. 1174–1178, Nov. 2007.

[90] J. F. Moulder, W. F. Stickle, P. E. Sobol, and K. D. Bomben, *Handbook of X-ray Photoelectron Spectroscopy Edited by.* 1992.

[91] J. E. Griffith and G. P. Kochanski, "The atomic structure of vicinal si(001) and ge(001)," *Crit. Rev. Solid State Mater. Sci.*, vol. 16, no. 4, pp. 255–289, 1990.

[92] R. C. Henderson, R. B. Marcus, and W. J. Polito, "Carbide contamination of silicon surfaces," *J. Appl. Phys.*, vol. 42, no. 3, pp. 1208–1215, Mar. 1971.

[93] D. Klement, M. Spreitzer, and D. Suvorov, "Formation of a strontium buffer layer on Si(001) by pulsed-laser deposition through the Sr/Si(001)(2 x 3) surface reconstruction," *Appl. Phys. Lett.*, vol. 106, no. 7, p. 071602, 2015.

[94] J. Dabrowski and H.-J. Müssig, *Silicon surfaces and formation of interfaces : basic science in the industrial world.* World Scientific, 2000.

[95] J. A. Appelbaum and D. R. Hamann, "Theory of reconstruction induced subsurface strain - application to Si(100)," *Surf. Sci.*, vol. 74, no. 1, pp. 21–33, May 1978.

[96] T. Uda *et al.*, "Ground state of the Si(0 0 1) surface revisited - Is seeing believing?," *Prog. Surf. Sci.*, vol. 76, no. 6–8, pp. 147–162, 2004.

[97] L. Perdigão *et al.*, "Semiconducting surface reconstructions of p-type Si(100) substrates at 5 K," *Phys. Rev. Lett.*, vol. 92, no. 21, pp. 2–5, 2004.

[98] T. Uozumi, Y. Tomiyoshi, N. Suehira, Y. Sugawara, and S. Morita, "Observation of Si(1 0 0) surface with noncontact atomic force microscope at 5 K," *Appl. Surf. Sci.*, vol. 188, no. 3–4, pp. 279–284, 2002.

[99] D. E. Aspnes and J. Ihm, "Biatomic steps on (001) silicon surfaces," *Phys. Rev. Lett.*, vol. 57, no. 24, pp. 3054–3057, Dec. 1986.

[100] J. E. Griffirh and G. P. Kochanski, "The atomic structure of vicinal Si(OO1) and Ge(001)," *Crit. Rev. Solid State Mater. Sci.*, vol. 16, no. 4, pp. 255–289, Jan. 1990.

[101] S. Gerhold, M. Riva, B. Yildiz, M. Schmid, and U. Diebold, "Adjusting island density and morphology of the SrTiO 3 (110)-(4 × 1) surface: Pulsed laser deposition combined with scanning tunneling microscopy," *Surf. Sci.*, vol. 651, pp. 76–83, Sep.

2016.
[102] H. Niehus, U. K. Köhler, M. Copel, and J. E. Demuth, “A real space investigation of the dimer defect structure of Si(001)-(2times8),” *J. Microsc.*, vol. 152, no. 3, pp. 735–742, Dec. 1988.
[103] M. Kuzmin *et al.*, “Dimer-vacancy defects on Si(1 0 0): The role of nickel impurity,” *Appl. Surf. Sci.*, vol. 506, p. 144647, Mar. 2020.
[104] T. Ichinokawa, H. Ampo, S. Miura, and A. Tamura, “Formation of surface superstructures by heat treatments on Ni-contaminated surface of Si(110),” *Phys. Rev. B*, vol. 31, no. 8, pp. 5183–5186, Apr. 1985.
[105] A. A. Demkov and A. B. Posadas, *Integration of Functional Oxides with Semiconductors*. 2014.
[106] A. A. Demkov and X. Zhang, “Theory of the Sr-induced reconstruction of the Si (001) surface,” *J. Appl. Phys.*, vol. 103, no. 10, p. 103710, 2008.
[107] K. Garrity and S. Ismail-Beigi, “Phase diagram of Sr on Si(001): A first-principles study,” *Phys. Rev. B - Condens. Matter Mater. Phys.*, vol. 80, no. 8, pp. 1–14, 2009.
[108] W. C. Fan, N. J. Wu, and A. Ignatiev, “Observation of ordered structures of Sr on the Si(100) surface,” *Phys. Rev. B*, vol. 42, no. 2, pp. 1254–1257, 1990.
[109] Y. Liang, S. Gan, and M. Engelhard, “First step towards the growth of single-crystal oxides on Si: Formation of a two-dimensional crystalline silicate on Si(001),” *Appl. Phys. Lett.*, vol. 79, no. 22, pp. 3591–3593, 2001.
[110] A. Herrera-Gómez *et al.*, “Photoemission from the Sr/Si(001) interface,” *J. Appl. Phys.*, vol. 90, no. 12, pp. 6070–6072, Dec. 2001.
[111] X. Hu, Z. Yu, J. A. Curless, R. Droopad, and K. Eisenbeiser, “Comparative study of Sr and Ba adsorption on Si (1 0 0),” vol. 181, pp. 103–110, 2001.
[112] D. M. Goodner, D. L. Marasco, A. A. Escuadro, L. Cao, and M. J. Bedzyk, “X-ray standing wave investigation of submonolayer barium and strontium surface phases on Si(001),” *Phys. Rev. B*, vol. 71, no. 16, pp. 1–6, 2005.
[113] J. W. Reiner, K. F. Garrity, F. J. Walker, S. Ismail-Beigi, and C. H. Ahn, “Role of strontium in oxide epitaxy on silicon (001),” *Phys. Rev. Lett.*, vol. 101, no. 10, pp. 3–6, 2008.
[114] M. Choi, A. B. Posadas, H. Seo, R. C. Hatch, and A. A. Demkov, “Charge transfer in Sr Zintl template on Si(001),” *Appl. Phys. Lett.*, vol. 102, no. 3, pp. 4–8, 2013.
[115] M. Kuzmin *et al.*, “Sr/Si(100)(1 × 2) reconstruction as a template for the growth of crystalline high-k films on silicon: Atomic structure and reactivity,” *Surf. Sci.*, vol. 646, pp. 140–145, 2016.
[116] W. Du *et al.*, “Identifying atomic geometry and electronic structure of (2×3) -Sr/Si (100) surface and its initial oxidation,” *J. Chem. Phys.*, vol. 129, no. 16, pp. 1–8, 2008.
[117] J. He, G. Zhang, J. Guo, Q. Guo, and K. Wu, “Atomic structure of Sr-induced reconstructions on the Si(100) surface,” *J. Appl. Phys.*, vol. 109, no. 8, pp. 1–4, 2011.
[118] S. Metev and K. Meteva, “Nucleation and growth of laser-plasma deposited thin films,” *Appl. Surf. Sci.*, vol. 43, no. 1–4, pp. 402–408, Dec. 1989.
[119] P. R. Willmott and J. R. Huber, “Pulsed laser vaporization and deposition,” *Rev.*

Mod. Phys., vol. 72, no. 1, pp. 315–328, 2000.

[120] G. C. Tyrrell, L. G. Coccia, T. H. York, and I. W. Boyd, "Energy-dispersive mass spectrometry of high energy ions generated during KrF excimer and frequency-doubled Nd:YAG laser ablation of metals," *Appl. Surf. Sci.*, pp. 227–232, Apr. 1996.

[121] E. Robert, *Pulsed Laser Deposition of Thin Films.* Hoboken, NJ, USA: John Wiley & Sons, Inc., 2006.

[122] L. Ji *et al.*, "A silicon-based photocathode for water reduction with an epitaxial SrTiO3 protection layer and a nanostructured catalyst," 2015.

[123] F. Wu, S. G. Jaloviar, D. E. Savage, and M. G. Lagally, "Roughening of steps during homoepitaxial growth on Si(001)," *Phys. Rev. Lett.*, vol. 71, no. 25, pp. 4190–4193, 1993.

[124] D. E. Jones, J. P. Pelz, Y. Hong, E. Bauer, and I. S. T. Tsong, "Striped phase and temperature dependent step shape transition on highly b-doped Si(001)−(2×1) Surfaces," *Phys. Rev. Lett.*, vol. 77, no. 2, pp. 330–333, 1996.

[125] M. R. Sardela, H. H. Radamson, J. O. Ekberg, J. E. Sundgren, and G. V. Hansson, "Growth, electrical properties and reciprocal lattice mapping characterization of heavily B-doped, highly strained silicon-molecular beam epitaxial structures," *J. Cryst. Growth*, vol. 143, no. 3–4, pp. 184–193, Oct. 1994.

[126] Y. fang Hu, J. shu Yang, and Q. Cai, "B-induced reconstruction on Si(100)-(2 × 1) surface studied with scanning tunneling microscopy," *Mater. Charact.*, vol. 48, no. 2–3, pp. 183–188, 2002.

[127] X. Y. Zhou *et al.*, "Epitaxial growth of SrTiO3 thin film on Si by laser molecular beam epitaxy," *Appl. Phys. Lett.*, vol. 90, no. 1, pp. 2–5, 2007.

[128] F. Hanzig *et al.*, "Crystallization dynamics and interface stability of strontium titanate thin films on silicon," *J. Appl. Crystallogr.*, vol. 48, no. 2, pp. 393–400, Apr. 2015.

[129] A. Imanaka, T. Sasaki, Y. Hotta, and S. Satoh, "Fabrication of Sr silicate buffer layer on Si(100) substrate by pulsed laser deposition using a SrO target," *J. Vac. Sci. Technol. A Vacuum, Surfaces, Film.*, vol. 32, no. 5, p. 051501, Sep. 2014.

[130] G. Saint-Girons *et al.*, "Epitaxy of SrTiO3 on Silicon: The Knitting Machine Strategy," *Chem. Mater.*, vol. 28, no. 15, pp. 5347–5355, Aug. 2016.

[131] L. V. Goncharova *et al.*, "Interface structure and thermal stability of epitaxial SrTiO 3 thin films on Si (001)," *J. Appl. Phys.*, vol. 100, no. 1, p. 014912, Jul. 2006.

[132] D. Diaz-Fernandez, M. Spreitzer, T. Parkelj, J. Kovač, and D. Suvorov, "The importance of annealing and stages coverage on the epitaxial growth of complex oxides on silicon by pulsed laser deposition," *RSC Adv.*, vol. 7, no. 40, pp. 24709–24717, May 2017.

[133] A. Thøgersen, J. H. Selj, and E. S. Marstein, "Oxidation Effects on Graded Porous Silicon Anti-Reflection Coatings," *J. Electrochem. Soc.*, vol. 159, no. 5, pp. D276–D281, Feb. 2012.

[134] Z. Jovanović *et al.*, "Control of SrO buffer-layer formation on Si(001) using the pulsed-laser deposition technique," *RSC Adv.*, vol. 6, no. 85, pp. 82150–82156, Aug. 2016.

[135] I. J. McColm, *Dictionary of Ceramic Science and Engineering.* Springer

Netherlands, 2013.

[136] F. Amy, A. S. Wan, A. Kahn, F. J. Walker, and R. A. McKee, “Band offsets at heterojunctions between SrTiO 3 and BaTiO 3 and Si(100),” *J. Appl. Phys.*, vol. 96, no. 3, pp. 1635–1639, Aug. 2004.

[137] R. P. Vasquez, “X-ray photoelectron spectroscopy study of Sr and Ba compounds,” *J. Electron Spectros. Relat. Phenomena*, vol. 56, no. 3, pp. 217–240, Jun. 1991.

[138] D. Diaz-Fernandez, M. Spreitzer, T. Parkelj, and D. Suvorov, “Multi-stage pulsed laser deposition of high quality epitaxial ultra-thin SrTiO3 on Si substrates,” *Appl. Surf. Sci.*, vol. 455, pp. 227–235, Oct. 2018.

[139] X. Hu *et al.*, “The interface of epitaxial SrTiO3 on silicon: In situ and ex situ studies,” *Appl. Phys. Lett.*, vol. 82, no. 2, pp. 203–205, Jan. 2003.

[140] L. Zhang *et al.*, “Continuously Tuning Epitaxial Strains by Thermal Mismatch,” *ACS Nano*, vol. 12, no. 2, pp. 1306–1312, Feb. 2018.

[141] G. Z. Liu, Q. Y. Lei, and X. X. Xi, “Stoichiometry of SrTiO 3 films grown by pulsed laser deposition,” *Appl. Phys. Lett.*, vol. 100, no. 20, p. 202902, May 2012.

[142] C. M. Brooks, L. F. Kourkoutis, T. Heeg, J. Schubert, D. A. Muller, and D. G. Schlom, “Growth of homoepitaxial SrTiO3 thin films by molecular-beam epitaxy,” *Appl. Phys. Lett.*, vol. 94, no. 16, p. 162905, Apr. 2009.

[143] H. L. Cai, X. S. Wu, and J. Gao, “Effect of oxygen content on structural and transport properties in SrTiO3-x thin films,” *Chem. Phys. Lett.*, vol. 467, no. 4–6, pp. 313–317, Jan. 2009.

[144] W. W. Peng *et al.*, “Room-temperature soft mode and ferroelectric like polarization in SrTiO3 ultrathin films: Infrared and ab initio study,” *Sci. Rep.*, vol. 7, no. 1, pp. 1–11, Dec. 2017.

[145] N. Pertsev, A. Tagantsev, and N. Setter, “Phase transitions and strain-induced ferroelectricity in epitaxial thin films,” *Phys. Rev. B - Condens. Matter Mater. Phys.*, vol. 61, no. 2, pp. R825–R829, Jan. 2000.

[146] J. H. Haeni *et al.*, “Room-temperature ferroelectricity in strained SrTiO3,” *Nature*, vol. 430, no. 7001, pp. 758–761, Aug. 2004.

[147] H. W. Jang *et al.*, “Ferroelectricity in strain-free SrTiO3 thin films,” *Phys. Rev. Lett.*, vol. 104, no. 19, p. 197601, May 2010.

[148] A. Vasudevarao *et al.*, “Multiferroic domain dynamics in strained strontium titanate,” *Phys. Rev. Lett.*, vol. 97, no. 25, p. 257602, Dec. 2006.

[149] C. H. Ahn *et al.*, “Local, nonvolatile electronic writing of epitaxial Pb(Zr0.52Ti0.48)O3/SrRuO=3 heterostructures,” *Science (80-.).*, vol. 276, no. 5315, pp. 1100–1103, May 1997.

[150] T. Tybell, C. H. Ahn, and J. M. Triscone, “Control and imaging of ferroelectric domains over large areas with nanometer resolution in atomically smooth epitaxial Pb(Zr0.2Ti0.8)O3 thin films,” *Appl. Phys. Lett.*, vol. 72, no. 12, pp. 1454–1456, Mar. 1998.

[151] H. Lüth and H. Lüth, “Surface and Interface Physics: Its Definition and Importance,” in *Surfaces and Interfaces of Solids*, Springer Berlin Heidelberg, 1993, pp. 1–29.

[152] A. Syed Mohd *et al.*, “A versatile UHV transport and measurement chamber for

neutron reflectometry under UHV conditions," *Rev. Sci. Instrum.*, vol. 87, no. 12, p. 123909, Dec. 2016.

[153] J. F. Calleja *et al.*, "Effect of a capping layer on the magnetic properties of island nanostructured Fe(110)," *J. Appl. Phys.*, vol. 97, no. 10, p. 104302, May 2005.

[154] M. J. Sik and R. P. Ferrier, "A High Vacuum, Low Temperature Specimen Transfer Device for use in Measuring Optical Properties of Thin Films[1] M. J. Sik and R. P. Ferrier, 'A High Vacuum, Low Temperature Specimen Transfer Device for use in Measuring Optical Properties of Thin Films,' ," *J. Phys. E.*, vol. 6, no. 8, pp. 749–750, 1973.

[155] C. A. Crider, G. Cisneros, P. Mark, and J. D. Levine, "Satellite vacuum system for a standard LEED–AES system with sample transfer capability," *J. Vac. Sci. Technol.*, vol. 13, no. 6, pp. 1202–1205, Nov. 1976.

[156] S. Messerli, S. Schintke, K. Morgenstern, A. Sanchez, U. Heiz, and W. D. Schneider, "Imaging size-selected silicon clusters with a low-temperature scanning tunneling microscope," *Surf. Sci.*, vol. 465, no. 3, pp. 331–338, Oct. 2000.

[157] P. Jiříček, M. Cukr, V. Kolařík, and S. Koc, "Transfer of samples between separated ultrahigh vacuum instruments for semiconductor surface studies," *Review of Scientific Instruments*, vol. 69, no. 7. American Institute of PhysicsAIP, pp. 2804–2805, 01-Jul-1998.

[158] G. Firpo, F. De Buatier Mongeot, C. Boragno, and U. Valbusa, "High performance portable vacuum suitcase," *Rev. Sci. Instrum.*, vol. 76, no. 2, p. 026108, Jan. 2005.

[159] Y. Watanabe *et al.*, "Portable ultrahigh-vacuum sample storage system for polarization-dependent total-reflection fluorescence x-ray absorption fine structure spectroscopy," *J. Vac. Sci. Technol. A Vacuum, Surfaces, Film.*, vol. 34, no. 2, p. 023201, Mar. 2016.

[160] "Ferrovac UHV suitcase." [Online]. Available: https://www.ferrovac.com/?tool=ProductList&category=UHV+Suitcase. [Accessed: 08-Mar-2021].

[161] E. Zupanič, R. Žitko, H. J. P. van Midden, I. Muševič, and A. Prodan, "Low-temperature Scanning Tunneling Microscopy and Spectroscopy of Noble-metal Surfaces," *Croat. Chem. Acta*, vol. 82, no. 2, pp. 485–491, 2009.

[162] Y. Shi, "Adsorption and Reactions of Water on the Copper (110) Surface Studied by Scanning Tunneling Microscopy," University of California, Berkeley, 2014.

Bibliography

Publications Related to the Thesis

Original scientific articles

T. Parkelj Potočnik, E. Zupanič, W. Y. Tong, E. Bousquet, D. Diaz-Fernandez, G. Koster, P. Ghosez and M. Spreitzer, "Atomic structure of Sr/Si(001)(1×2) surfaces prepared by Pulsed laser deposition," *Applied Surface Science*, vol. 471, pp. 664-669, 2019.

D. Diaz-Fernandez, M. Spreitzer, T. Parkelj Potočnik and D. Suvorov, "Multi-stage pulsed laser deposition of high quality epitaxial ultra-thin $SrTiO_3$ on Si substrates," *Applied Surface Science*, vol. 455, pp. 227-235, 2018.

D. Diaz-Fernandez, M. Spreitzer, T. Parkelj Potočnik, J. Kovač and D. Suvorov. "The importance of annealing and stages coverage on the epitaxial growth of complex oxides on silicon by pulsed laser deposition", *RSC advances*, vol. 7, no. 40, pp. 24709-24717, 2017.

Review article

M. Spreitzer, D. Klement, T. Parkelj Potočnik, U. Trstenjak, Z. Jovanović, G. Koster, et al., "Epitaxial ferroelectric oxides on silicon with perspectives for future device applications", *APL materials*, vol. 9, no. 4, pp. 040701-1- 040701-14, 2021.

Professional article

T. Parkelj Potočnik, E. Zupanič, J. Kovač, and M. Spreitzer. "Prenos vzorcev v ultravisokem vakuumu s pomočjo vakuumskega kovčka (Transfer of samples in ultra-high vacuum by means of a vacuum suitcase)," accepted for publication in the journal *Vakuumist* in 2021.

Published scientific conference contribution abstracts (invited talk)

M. Spreitzer, T. Parkelj Potočnik, Z. Jovanović, G. Koster, and D. Suvorov. "Tailoring epitaxial oxide thin film on Si (001) with atomic precision," *18th International Conference on Thin Films &18th joint Vacuum Conference, ICTF, JVC 2020*, Budapest, Hungary, November 22-26, 2020, p. 20.

D. Suvorov, D. Diaz-Fernandez, T. Parkelj Potočnik, U. Trstenjak, and M. Spreitzer, "Epitaxial integration of oxides with silicon," *Twenty-first Annual Conference YUCOMAT 2019 & Eleventh World Round Table Conference on Sintering, WRTCS 2019*, Herceg Novi, Montenegro, September 2-6, 2019. Belgrade: Materials Research Society of Serbia, 2019. p. 1.

M. Spreitzer, D. Diaz-Fernandez, T. Parkelj Potočnik, U. Trstenjak, and D. Suvorov, "Tailoring epitaxial oxide thin film on Si(001) using pulsed-laser deposition", *Nineteenth Annual Conference YUCOMAT 2017*, Herceg Novi, Montenegro, August 31 - September 4-8, 2017. Belgrade: Materials Research Society of Serbia, 2017, p. 41.

Published scientific conference contribution abstracts

T. Parkelj Potočnik, M. Spreitzer, E. Zupanič, W. Y. Tong, D. Diaz-Fernandez, P. Ghosez, D. Suvorov, "Combined STM/DFT study of Sr-buffered Si(001) surfaces prepared by pulsed laser deposition", *SPSTM-7 & LTSPM-1 International Conference 2018, Advances in high-precision and low-temperature Scanning Probe Microscopy, Satellite meeting of the ICN+T 2018*, Nijmegen, The Netherlands, July 28-30, 2018, p. 47.

T. Parkelj Potočnik, M. Spreitzer, D. Diaz-Fernandez, E. Zupanič, D. Suvorov, "Atomic structure of Sr-buffered Si(001) grown by pulsed laser deposition", *COST TO-BE Spring Meeting 2018*, Sant Feliu, Spain, March 12-14, 2018.

D. Diaz-Fernandez, Tjaša Parkelj Potočnik, Matjaž Spreitzer, Janez Kovač, Danilo Suvorov, "PLD growth of ultra-thin SrTiO3//1/2 ML Sr/Si (001) samples: coverage, annealing and buffer layer thickness effects", *ECASIA`17, European conference on applications of surface and interface analysis*, Montpellier, France, September 24-29, 2017, p. 214.

M. Spreitzer, D. Diaz-Fernandez, T. Parkelj Potočnik, D. Suvorov, "Interfacing oxides with silicon using pulsed laser deposition", *MS & T17, Materials Science & Technology: Conference tools for Materials Science & Technology*, Pittsburgh, Pennsylvania, USA, October 8-12, 2017.

T. Parkelj Potočnik, M. Spreitzer, "Different approaches to the preparation of Sr buffered Si(001) surfaces using pulsed laser deposition", *25th International Conference on Materials and Technology*, Portorož, Slovenia, October 16-19, 2017. M. Godec et al., Ljubljana: Inštitut za kovinske materiale in tehnologije, 2017, p. 142.

T. Parkelj Potočnik, D. Diaz-Fernandez, M. Spreitzer, E. Zupanič, D. Suvorov, "Local structural studies of Sr-buffered Si surface prepared with pulsed laser deposition", *9th Jožef Stefan International Postgraduate School Students' Conference and 11th Young researchers' Day*, Ljubljana, Slovenia, April 19-20, 2017. M. Pavlin et al., Ljubljana: Jožef Stefan International Postgraduate School: Jožef Stefan Institute, 2017, p. 59.

T. Parkelj Potočnik, D. Diaz-Fernandez, M. Spreitzer, E. Zupanič, D. Suvorov, "Scanning tunneling microscopy studies of ultra-thin $SrTiO_3$ films on Si(001) grown by PLD", *24th International Conference on Materials and Technology*, Portorož, Slovenia, September 28-30, 2016. M. Godec et al., Ljubljana: Inštitut za kovinske materiale in tehnologije, 2016, p. 170.

D. Diaz-Fernandez, T. Parkelj Potočnik, M. Spreitzer, J. Kovač, D. Suvorov, "Characterization of epitaxial ultra-thin $SrTiO_3$ films on Si(001) grown by pulsed laser deposition", *COST TO-BE Fall Meeting*, Ljubljana, Slovenia, September 28-30 2016, H. Uršič Nemevšek et al., Ljubljana: Jožef Stefan Institute, 2016, p. 21.

T. Parkelj Potočnik, D. Diaz-Fernandez, M. Spreitzer, E. Zupanič, G. Koster, D. Suvorov, "Scanning tunneling microscopy of sub-monolayer structures of Sr on Si(001) grown by PLD", *COST TO-BE Fall Meeting*, Ljubljana, Slovenia, 28-30 September 2016, H. Uršič Nemevšek et al., Ljubljana: Jožef Stefan Institute, 2016, p. 75.

Other Publications

Original scientific article

D. Dominko, D. Starešinić, K. Biljaković, M. Dekić, A. Salčinović Fetić, K. Hrvat, M. Lozanič, J. Demsar, V. Grigorev, T. Parkelj Potočnik, M. Spreitzer, "Single crystal-like thin films of blue bronze", accepted for publication in in the journal *Thin Solid Films* in 2021.

Popular article

T. Parkelj Potočnik, "Veliko hrupa za nič, " *Razpotja: revija humanistov Goriške*, vol. 11, no. 41, pp. 10-12, 2020.

Published scientific conference contribution abstracts

M. Van Midden, T. Parkelj Potočnik, J. Mravlje, R. Žitko, M. Spreitzer, E. Zupanič, "Scanning tunneling microscopy and spectroscopy of thin films of strontium ruthenates: simulation perspective", *DPG-Frühjahrstagung 2018, joint meeting of the DPG and EPS Condensed Matter Divisions*, Berlin, Germany, March 11-16, 2018.

M. Van Midden, T. Parkelj Potočnik, J. Mravlje, R. Žitko, M. Spreitzer, E. Zupanič, "Scanning tunneling microscopy and spectroscopy of thin films of strontium ruthenates", *13th Multinational Congress on Microscopy*, Rovinj, Croatia, September 24-29, 2017. Andreja Gajović, Zagreb: Ruđer Bošković Institute: Croatian Microscopy Society, 2017, pp. 76-77.

Biography

Tjaša Parkelj Potočnik obtained her bachelor's degree from the Faculty of Mathematics and Physics, University of Ljubljana in 2012. In 2015, she finished her master studies at FMF-UL, and enrolled in the Nanosciences and Nanotechnologies third-level study program at the Jožef Stefan International Postgraduate School in Ljubljana. At the same time, she started working as a Junior Researcher at the Advanced Materials Department (K9) at the Jožef Stefan Institute in Ljubljana. In 2017, she was awarded for the second best oral presentation at the 25th International Conference on Materials and Technologies in Portorož.